Development of Optical Fiber Sensors for Environmental Engineering and Homeland Security Employing Evanescent Wave Absorption and Localized Surface Plasmon Resonance Spectroscopy

A Thesis Submitted

in Partial Fulfillment of the Requirements for the Degree of

DOCTOR OF PHILOSOPHY

By

FATIMA BANOO

(Roll no: 206121103)

Supervisor:

Prof. Sunil K. Khijwania

Department of Physics

Indian Institute of Technology Guwahati

Guwahati-781039, Assam, India

Dedicated to my Bacholay

Haji Mohd Hassan Aasi

STATEMENT

I hereby declare that the research work presented in this thesis entitled "**Development of Optical Fiber Sensors for Environmental Engineering and Homeland Security Employing Evanescent Wave Absorption and Localized Surface Plasmon Resonance Spectroscopy**", is carried out by me under the supervision of **Prof. Sunil K. Khijwania**, Professor, Department of Physics, Indian Institute of Technology Guwahati. The contents of this thesis have not been submitted to any other institute or university for the award of any degree.

Date …….…….

Fatima Banoo
(206121103)

Research Scholar
Department of Physics
Indian Institute of Technology Guwahati
Guwahati-781039, Assam
India

CERTIFICATE

This is to certify that work contained in the thesis entitled "**Development of Optical Fiber Sensors for Environmental Engineering and Homeland Security Employing Evanescent Wave Absorption and Localized Surface Plasmon Resonance Spectroscopy**", by Ms. Fatima Banoo (Roll no: 206121103), a student of Department of Physics, Indian Institute of Technology Guwahati, for the award of degree of Doctor of Philosophy, has been carried out under my supervision. The contents of this thesis have not been submitted to any other institute or university for the award of any degree.

Date …….…….

Prof. Sunil K. Khijwania

Professor, Department of Physics
Indian Institute of Technology Guwahati
Guwahati-781039, Assam
India

ACKNOWLEDGEMENTS

First and foremost, I would like to express my heartfelt gratitude to my esteemed supervisor, **Prof. Sunil K. Khijwania**, for giving me the invaluable opportunity to work under his guidance. His unwavering support, insightful knowledge, and patience have been instrumental in shaping my research journey and providing me with a clear direction throughout the thesis. His inspiring suggestions, constant encouragement, and dedicated mentorship have not only enriched my academic growth but also left a lasting impact on my life. I am deeply grateful for the example he has set as both a distinguished physicist and an exceptional professor.

I sincerely thank my doctoral committee members, **Prof. Kanhaiya Pandey**, **Prof. Parameswar K. Iyer**, and **Prof. Girish S. Setlur**, for their continuous support in reviewing my research work and providing invaluable suggestions. Their insightful feedback and guidance have been instrumental in refining my work, and I am truly grateful for their time and expertise.

I am deeply grateful to the members of the Fiber Optics Lab, Mr. Debabrata Paul, Mr. Manish Shing Negi and Mr. Subham Koley for their constant support and invaluable contributions. Their assistance and collaboration have played a significant role in my research journey, and I truly appreciate their generosity in sharing their expertise and insights.

My PhD life would have been incomplete without the constant support and companionship of my dear friends Debabrata Paul, Camelia Jana, Shalini Verma, Manish Singh Negi, Subham Koley, Amit Kumar, Indrajeet Saha, Shilpa Singh, Rakshanda Goswami. From our lively cooking sessions, intense UNO matches to random trips are the memories I will cherish forever. Beyond the laughter and adventure, their constant encouragement, constructive criticism, and presence through both highs and lows made this journey truly special. Their support not only enriched my PhD experience but also helped me grow as an individual, and for that, I am profoundly grateful.

Finally, and most importantly, this PhD journey would not have been possible without the love, prayers, and support of my family. My heartfelt gratitude to my uncle Haji Mohd Hassan Aasi, my parents Nissar Hussain Chopa and Fiza Banoo Chopa, for their unconditional love, support and encouragement. I especially thank my brothers Kumail Murtaza Chopa and Ghulam Abass Chopa for always standing by me, and my sisters Tohira Banoo Chopa and Hakeema Banoo

Chopa for their constant support, understanding, and friendship. I remember with deep affection my brother Kumail Murtaza Chopa, whose loss during my PhD left a void that can never be filled. I miss him every day and wish he were here to share this moment. His memory continues to inspire my strength and perseverance. A special mention to the little ones of our family Mujtaba, Fiza, Mustafa, and Imtiyaz whose love and laughter brightened my toughest days. To my entire family, thank you for believing in me, standing beside me, and giving wings to my dreams. This achievement is as much yours as it is mine.

Fatima Banoo

ABSTRACT

This thesis focuses on the development of optical fiber sensors for detecting water contaminants, specifically mercury (Hg^{2+}), arsenic (As^{3+}), and explosive trinitrophenol (TNP), which are crucial for environmental monitoring and homeland security respectively. The primary objective is to develop highly sensitive sensors with exceptionally low limits of detection (LOD), rapid response times, high selectivity, and high degree of stability, repeatability and reliability. The novelty of this research lies in the innovative integration of various nanocomposites, polymers, and composite materials with fiber optics to develop optical fiber Hg^{2+}, As^{3+}, and TNP sensors. Two key sensing techniques were employed: intensity modulation through evanescent wave absorption and wavelength modulation using localized surface plasmon resonance (LSPR). The research begins with the development of a U-shaped optical fiber LSPR based sensor for Hg^{2+} detection, utilizing graphene oxide and chitosan (GO-CS) composite as the sensing material. This sensor demonstrates outstanding sensitivity of 0.0728 nm/ppb, an ultra-low LOD of 0.29 ppb. It also exhibits high selectivity towards Hg^{2+} and a rapid response time of 0.6 s. In order to further enhance the sensing performance, a second Hg^{2+} sensor is developed incorporating carbon nanotube/polyvinyl alcohol (CNT/PVA) nanocomposite as the sensing material. This sensor offered even higher sensitivity of 0.2458 nm/ppb and a lower LOD of 0.08 ppb, while maintaining high selectivity and an improved response time of 0.4 s. Next, an optical fiber LSPR sensor for detecting another highly toxic water contaminant As^{3+} ion is developed, employing Al_2O_3/GO nanocomposite as the sensing material. This sensor exhibits high sensitivity of 0.217 nm/ppb, a remarkably low LOD of 0.09 ppb. The sensor also exhibits a fast response time of 0.5 s and high selectivity towards As^{3+}. To further enhance sensing performance, another As^{3+} sensor is developed using lauryl-functionalized gold nanoparticles. This sensor offered an enhanced sensitivity of 0.3073 nm/ppb, even lower LOD of 0.06 ppb, while maintaining high selectivity and rapid response time of 0.5 s. For TNP detection, an optical fiber sensor based on evanescent wave absorption is developed, utilizing a novel polymer (PFTPA) film. The sensor exhibits high sensitivity of 0.0032/ppb, a remarkably low LOD of 1.06 ppb, rapid response time of 2 s and shows high selectivity towards TNP. In order to further enhance the sensing performance, another TNP sensor is developed using a LSPR configuration, incorporating zinc oxide quantum dots (ZnO QDs) as the sensing film. This sensor offers a much lower LOD of 0.19 ppb and significantly higher sensitivity of 0.1288 nm/ppb, while maintain the rapid response time of 2 s and high selectivity towards TNP. It is worth mentioning that, all the novel sensors

developed in this research exhibits excellent reversibility, repeatability, stability and reliability. Moreover, their real-world applicability is validated through successful detection of Hg^{2+}, As^{3+}, and TNP in real water samples, demonstrating their potential for environmental monitoring and homeland security applications.

List of contents

List of Figures

List of Tables

List of Abbreviation

OFS	Optical Fiber Sensor
EMI	Electromagnetic Interference
ICC	Information Carrying Capacity
TIR	Total Internal Reflection
SMF	Single mode Fiber
MMF	Multimode Fiber
HF	Hydrofluoric
PCS	Plastic Clad Silica
MZI	Mach-Zehnder Interferometer
MI	Michelson Interferometer
FPI	Fabry-Perot Interferometer
PM-PCF	Polarization Maintaining Photonic Crystal Fiber
FBG	Fiber Bragg Grating
LPG	Long Period Grating
LSPR	Localized Surface Plasmon Resonance
SPR	Surface Plasmon Resonance
LOD	Limit of Detection
EM	Electromagnetic
WHO	World Health Orginization
PPB	Parts Per Billion
ICPMS	Inductively Coupled Plasma Mass Spectrometry
HPLC	High Performance Liquid Chromatography
RDX	1,3,5-Trinitro-1,3,5-triazinane
TNT	2,4,6-Trinitrotoluene
TNP	Trinitrophenol

PA	Picric Acid
DNT	2,4-Dinitrotoluene
NT	4-Nitrotoluene
DPC	N,N-Diisopropylcarbodiimide
GO-CS	Graphene oxide and Chitosan
AuNPs	Gold nanoparticles
CNT/PVA	Carbon nanotube/Polyvinyl alcohol
Al_2O_3/GO	Aluminium oxide and Graphene oxide
LS	Lauryl Sulphate
ZnO QDs	Zinc oxide Quantum Dots
SMA	Subminiature Version A
RPD	Relative Percentage Difference
DAQ	Data Acquisition
USEPA	US Environment Protection Agency
FETEM	Field Emission Transmission Electron Microscope
XRD	X-ray Diffraction
FESEM	Field Emission Scanning Electron Microscope
RIU	Refractive Index Unit
APTMS	3-amino-propyltrimethoxysilane
CNT	Carbon Nanotubes
THF	Tetrahydrofuran
RSD	Relative Standard Deviation
KOH	Potassium Hydroxide

Chapter 1 : Introduction and Literature Review

1.1 Introduction

Sensing different parameters is essential for acquiring valuable information and for monitoring and controlling various industrial, scientific, and environmental processes. A sensor is a device that translates changes in one physical parameter into shifts in another parameter, which can be measured more accurately and conveniently [1]. These measurable parameters include optical signals (e.g., intensity, wavelength, polarization, phase), physical signals (e.g., force, pressure, mass flow, vibration, rotation, tilt, strain, refractive index etc.), thermal signals, electrical and magnetic signals (e.g., voltage, current, resistance, capacitance, pulse duration, frequency and dielectric constant, magnetic flux density, magnetic field direction and permeability etc), and chemical or biological signals (e.g., composition, concentration, pH, glucose levels, relative humidity, gas concentration etc.). Hence, for effective process-control and performance optimization, sensors have a vast range of applications in practically all fields of research and engineering, environmental engineering, health monitoring, industrial applications as well as in homeland security.

1.2 Optical fiber sensor

The discovery of optical fiber was a significant milestone in the telecommunications industry. In the early 1970s, as fiber optic technology began to evolve for telecommunications, it was noted that optical fibers were highly sensitive to external factors such as bending, microbending, and pressure. Initially, considerable efforts were made on reducing this sensitivity to external perturbations. However, it soon became apparent that the unique sensitivity of optical fibers to these perturbations could be exploited for sensing various parameters. This realization led to the birth of optical fiber sensing technology. Advancements in fiber optics and the associated optoelectronic industry, including the development of low-loss optical fibers and sophisticated optical sources and interrogators, have greatly accelerated the progress of optical fiber sensors. These developments have made a profound impact, enabling the use of optical fiber sensors across a wide range of fields, including engineering (civil, mechanical, aeronautical, chemical, electrical, automotive), biomedical applications, general sciences, and even homeland security. The significant and outstanding advantages of

optical fiber sensing technology over conventional sensors have driven a global surge in research and development in this field. Some of the key benefits of optical fiber sensors include:

1. Fiber optic sensors offer exceptional sensitivity, enabling the detection of even the slightest variations in the physical parameters they are designed to measure.
2. As optical devices, optical fiber sensors (OFSs) are completely immune to electromagnetic interference (EMI). This inherent immunity to EMI makes them highly reliable.
3. Low-loss optical fibers combined with fiber amplifiers allows propagation of light across thousands of kilometres. Such long-distance signal propagation without any attenuation facilitates effective remote sensing.
4. High bandwidth of optical fibers enables an unparalleled information-carrying capacity (ICC) exceeding 100 Tb/s-km, this is far beyond what electrical systems can achieve. This capacity enables: (a) multiplexing of large number of sensors, each assigned to a specific optical channel, over a single fiber transmission line, (b) distributed sensing, allowing continuous measurement along the entire fiber, and (c) multi-parameter sensing capabilities.
5. As optical fibers are composed of dielectric materials, OFSs are naturally electrically isolated from the interrogating electronics.
6. Ease of miniaturization, allowing the development of compact, lightweight, and flexible sensors. Their small size and lightweight nature make optical fiber sensors easy to surface-mount or embed within composite materials without intrusion.
7. Wide temperature range and ability to function in harsh environments, making them versatile for diverse applications.

Owing to these significant advantages, the optical fiber sensors are now successfully and accurately used to monitor nearly all parameters of practical importance, such as pressure,

temperature, liquid level, refractive index, pH, antibodies, electric current, voltage, rotation, displacement, acceleration, acoustics, electric and magnetic fields, tilt, torsion, and strain, not only in controlled test environments but also in real-field applications.

Optical fiber sensors are broadly categorized as either extrinsic or intrinsic. In an extrinsic sensor, the fiber simply serves as a pathway, directing light to and from the sensing region where external environmental factors modulate the optical signal. In contrast, an intrinsic sensor uses the fiber itself as the sensing element, with the environmental change directly affecting an inherent property of the transmitted light, such as its phase, polarization, wavelength, or intensity. Consequently, intrinsic fiber sensors can be further classified by the type of modulation they employ, such as intensity, wavelength, phase and polarization modulation. Among these, intensity, wavelength and phase modulation are particularly popular among researchers due to their relatively simple implementation.

1.2.1 Intensity modulation based optical fiber sensors

Intensity modulation based optical fiber sensors hold significant practical importance due to their simple fabrication process. Intensity modulation in optical fiber can be achieved through various methods. Among these, the intensity modulation through evanescent wave absorption technique is widely employed by researchers. An optical fiber consists of a cylindrical core of radius a and index of refraction n_1, surrounded by a cladding of outer radius b and index of refraction n_2, where $n_1 > n_2$ as shown in Fig. 1.1. In general, when a light beam travelling inside denser medium (n_1) at an angle θ encounters the interface between the denser and the rarer medium (such as core-clad interface in the case of optical fiber), light gets partially reflected

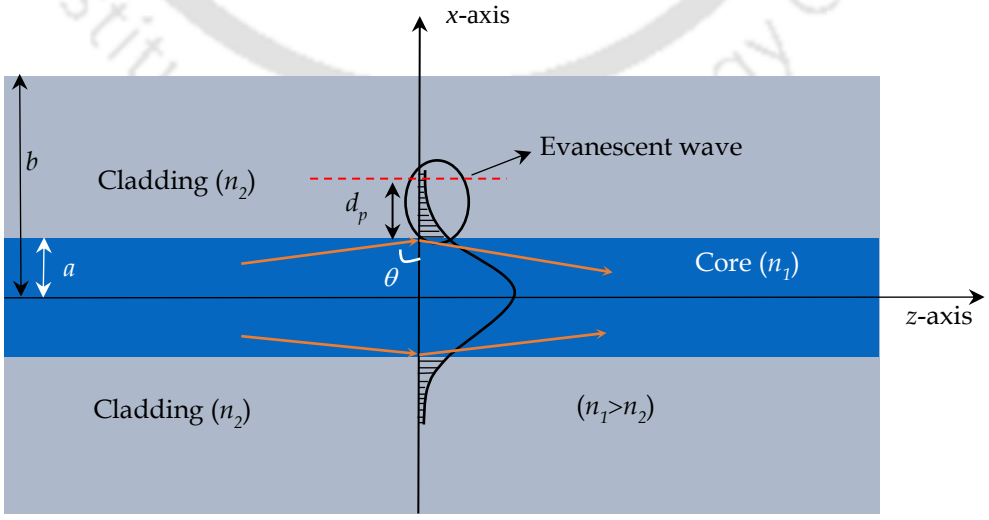

Figure 1.1: Schematic diagram of total internal reflection and evanescent wave inside an optical fiber.

and partially refracted. Here, θ is measured with respect to the normal at the interface (Fig. 1.1). If the angle θ is greater than the critical angle, given by $\theta_c = sin^{-1}\left(\frac{n_2}{n_1}\right)$, the phenomenon of total internal reflection takes place. Solving Maxwell's equations and applying boundary conditions at the interface reveals the presence of a wave in the rarer medium, known as the evanescent wave. This evanescent wave is mathematically expressed as:

$$\mathbf{E} = \mathbf{E}_o e^{-\beta x} exp\left[i\left(k\frac{n_1 sin\theta}{n_2}z - \omega t\right)\right] \tag{1.1}$$

here, x represents the direction perpendicular to the interface. $\mathbf{E}_o$ is the amplitude of the wave, say at $x = \pm a$ in Fig. 1.1, k is the propagation constant in the rarer medium, β is the decay coefficient, given by $\beta = \frac{n_2}{n_1}\sqrt{sin^2\theta - \frac{n_1^2}{n_2^2}}k$, z is the direction along the interface and ω is the angular frequency of the wave. As can be observed from the equation, the evanescent wave propagates along the interface, while its amplitude decays exponentially in the direction perpendicular to the interface.

In the case of optical fiber, which is cylindrically symmetric dielectric waveguide, if a light beam launched inside the fiber core at an angle ϕ with respect to the axis of the fiber (equivalent to the angle θ with respect to the normal at the core-cladding interface as depicted in Fig. 1.1) suffers TIR at the upper core-cladding interfaces, it also suffers TIR at the lower core-clad interface. Such light beams are trapped within the fiber core and propagate via successive TIRs down the fiber length. Importantly, there exists a set of discrete values for the angle ϕ at which light beams are guided by the optical fiber. Also, corresponding to the light beam travelling at $+\phi$, there exists another light beam that travels at an angle of $-\phi$ within the fiber. Such beams travelling at $\pm\phi$ superimpose with each other, and form the guided modes of the optical fiber. As an example, the intensity distribution of the fundamental mode within the optical fiber is shown in Fig. 1.1. As can be observed from the figure, intensity distribution of this guided mode is not confined to the core, but also extends into the cladding region. This is due to the evanescent wave associated to the TIR. The extent of the extension of the intensity distribution into the cladding region is mode specific. However, a key parameter associated with the evanescent wave is the penetration depth (d_p). The penetration depth indicates the distance from the core-clad interface at which the amplitude of the evanescent wave decreases to 1/e of its value at the interface. One can readily obtain the penetration depth from Eq. 1.1. However, in

order to exploit evanescent wave for designing intensity modulation based optical fiber sensor, cladding of the optical fiber is removed over a short section. This decladded portion of the fiber core is then directly exposed to the measurand (gas, liquid etc.). This exposed section defines the sensing region of the optical fiber sensor. Within this sensing region, the critical angle is denoted as θ_{cs}, and given by:

$$\theta_{cs} = sin^{-1}\left(\frac{n_{cs}}{n_1}\right) \tag{1.2}$$

where n_{cs} is the refractive index of the sensing region. The penetration depth in the sensing region is given by [2]:

$$d_p = \frac{\lambda}{2\pi n_1\left(\cos^2\theta_{cs} - \cos^2\theta \sin\theta_\phi\right)^{1/2}} \tag{1.2}$$

where λ is the wavelength of light launched into the fiber; θ_ϕ is the skewness angle, which is equal to $\pi/2$ for meridional rays; θ represents the angle of the guided ray relative to the normal at the core-cladding interface. The penetration depth d_p is usually smaller than the operating wavelength λ. The penetration depth determines the sensing volume in which the evanescent wave can interact with the surrounding environment and gets attenuated due to absorption, scattering, or changes in the refractive index. An optical fiber can accommodate multiple guided modes. The effective evanescent wave field surrounding the fiber core arises from the superposition of the field distributions of all these guided modes within the fiber. The amount of energy available for interaction with the measurand in the evanescent field is described by the fraction of total guided power (r) present in the cladding region, which is defined as [2]:

$$r = \frac{P_{clad}}{P_{total}} \tag{1.4}$$

where P_{clad} is the power present in the cladding region and P_{total} is the total guided power. Values of r is generally less than 1% for weakly guiding multimode fibers [38]. However, as the angle θ approaches the critical angle of the sensing region, both the d_p and r increase significantly. In a straight optical fiber, the angle θ remains constant throughout the sensing region. As a result, the minimum possible value of θ in the sensing region is equal to the critical angle θ_c of the fiber. In practical scenarios, $n_2 > n_{cs}$, and therefore θ cannot approach θ_{cs} in the case of straight optical fiber. Hence, in straight optical fiber significant enhancement of d_p and

r cannot be achieved. Enhancing d_p and r is essential for achieving higher sensitivity and can be accomplished through various techniques, such as bending the optical fiber in the sensing region [3], tapering the sensing region [4], or by lower mode removal via masking at the launch optics [5]. In single-mode fiber (SMF), the values of d_p and r are significantly higher than in multimode fiber (MMF). The initial step in developing an optical fiber sensor (OFS) that employs intensity modulation through evanescent wave absorption is ensuring the direct access of the evanescent wave. However, removing the silica cladding of SMF is challenging. One approach to get an access of the evanescent wave in SMF is by preparing a side-polished half-block [6]. This process requires precise alignment and controlled pressure. Alternatively, the cladding can be etched using Hydrofluoric (HF) acid [7], though extreme caution is essential due to HF's hazardous nature. Moreover, due to the core diameter being of the order of few microns, achieving precise alignment and efficient power coupling in SMF is quite challenging. In the case of MMF, d_p and r are comparatively lower. However, the cladding of specially fabricated multimode fibers, such as plastic-clad-silica (PCS) fibers, can be easily removed, allowing straightforward access to the evanescent wave. Additionally, the high throughput-power and ease of power coupling in multimode fibers make them a preferred choice for designing evanescent wave based sensors.

There are two ways of sensor development exploiting intensity modulation through evanescent wave absorption. When the wavelength spectrum of the light source with peak wavelength λ_{max} falls within the absorption band of the analyte, direct absorption of power carried in the evanescent wave takes place. This is known as direct sensing. In contrast, if the wavelength spectrum of the light source does not fall within the absorption band of the analyte, a different approach is required. One option is to switch to a light source with a wavelength spectrum that falls within the absorption band of the analyte. However, this may not always be feasible due to the limitations in available light sources or if possible, source might be extremely costly. In such cases, the second approach, known as indirect sensing, is employed. Here, one of the available sources is retained, and the bare core of the fiber is chemically synthesized with a favourable chemical. The selection of this chemical is crucial, as it must be reactive to the analyte. Upon exposure to the analyte, it should modify its physical or chemical properties in a way that can be mapped at the wavelength spectrum of the light source.

1.2.2 Phase modulation based optical fiber sensor.

Phase modulation is another very popular technique which is widely employed in optical fiber sensing across various applications. In order to detect phase variations in an optical fiber caused by environmental disturbances, interferometric methods are employed to transform phase modulation into intensity modulation. The commonly employed interferometers include the Sagnac interferometer, Mach-Zehnder interferometer (MZI), Michelson interferometer (MI), and Fabry-Perot interferometer (FPI) [8], [9]. The optical fiber Sagnac interferometer launches light in opposite directions through a fiber loop, detecting rotation-induced phase fluctuations as a time difference between the beams. Optical fiber MZIs split light into a reference and sensing arm, with recombined beams forming an interference pattern. Any change in the length of one arm, such as mechanical or thermal strain in the sensing arm, induces a phase shift between the beams. This phase shift alters the observed interference pattern, enabling precise measurement of the strain or other parameters influencing the arm's length. Similarly, optical fiber Michelson interferometers use a single directional coupler to split and recombine light. The light is divided into sensing and reference arms, travels through these arms, reflects back, and recombines at the original coupler; thus, effectively doubling the optical phase shift per unit length [8].

1.2.3 Polarization modulation based optical fiber sensor

Polarization modulation based optical fiber sensor utilizes the birefringence properties of optical fibers to measure various physical parameters. When strain is applied to an optical fiber, it alters the birefringence, creating a measurable phase difference between the two polarization states of light. This phase difference can be detected and correlated to the strain or stress applied to the fiber. By monitoring changes in the polarization state, these sensors can precisely measure strain, pressure, temperature, and even biochemical parameters in some cases. In recent decades, polarization maintaining photonic crystal fiber (PM-PCF) based Sagnac interferometers have been extensively used to develop polarization modulation based optical fiber sensors [10]-[12]. PM-PCF offers several advantages over conventional fibers, including endless single-mode guidance, reduced temperature sensitivity, a large mode area, and high birefringence. Additionally, PM-PCF exhibits very low bending loss due to its large numerical aperture and small core diameter. These characteristics make PM-PCF-based sensors highly suitable for applications in aerospace, civil engineering, telecommunications, and healthcare industries, where precise and reliable measurements are essential in challenging environments.

1.2.4 Wavelength modulation based optical fiber sensor

Another widely used technique for developing optical fiber sensors across various scientific, engineering, and industrial applications is the wavelength modulation technique. This approach exploits changes in the wavelength of light to detect different parameters of interest. Wavelength-modulation schemes can be implemented through various mechanisms, including wavelength-dependent absorption, dispersion, interference, and scattering [13]. However, with the invention and advancements of fiber-based devices, particularly fiber gratings such as fiber Bragg gratings (FBGs) and long-period gratings (LPGs), these have become synonymous with optical sensing technology, especially for real-field applications [14], [15]. Hence, FBG and LPG are among the most commonly employed wavelength modulation scheme by researchers. Another widely recognized method for achieving wavelength modulation in optical fiber sensor is through the localized surface plasmon resonance (LSPR). Experiencing remarkable progress in the recent decade, nanotechnology has greatly influenced other research areas, such as, photonics, medical science, environmental engineering, electronics engineering etc. Among various developments, metal nanoparticles stand out due to their unique optical properties, which enable them to absorb and scatter light in specific regions of the visible spectrum [16]. What distinguishes these nanoparticles is their capacity to transform the energy of incoming light into a collective oscillation of electrons, known as localized surface plasmon resonance (LSPR). LSPR is pivotal not only for its wavelength-selective absorption and scattering but also for its ability to produce significant electromagnetic field enhancements at the nanoparticle surface. This effect has proven invaluable in applications such as spectroscopic analysis and heat-mediated molecular release [17], [18]. Today noble metal nanoparticles have been extensively used across a wide range of fields, including electro-optical and semiconducting materials [19], catalytic materials [20], biological imaging agents [21], and biosensor technologies [22].

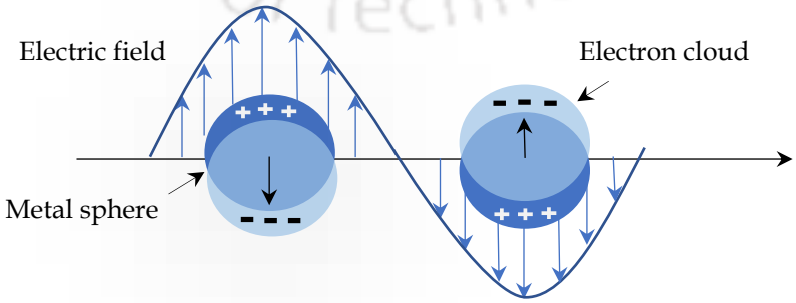

Figure 1.2: Localized surface plasmon resonance.

1.2.4.1 Localized surface plasmon resonance

When light interacts with metallic nanoparticles, the conduction electrons in the metal collectively oscillate in response to the oscillating electric field of the incident light, as depicted in Fig. 1.2. Additionally, an attractive Coulomb force between the electrons and nuclei contributes to the oscillation, forming an "electric cloud" around the nucleus. These coherent oscillations of electrons are referred to as LSPR, with the resonance frequency being dependent on the dielectric constant of the metal.

In order to find out the electric field outside the metal nanoparticle, consider a metal sphere of radius *a,* which is embedded within an external medium—such as a vacuum, gas, or liquid. The dielectric constant of the external medium is ϵ_{out}. The metal sphere itself has a dielectric constant ϵ_{in}, which is considered independent of its size. This embedded metal sphere is illuminated by a linearly (*z*-) polarized laser light of wavelength λ propagating along the x-axis

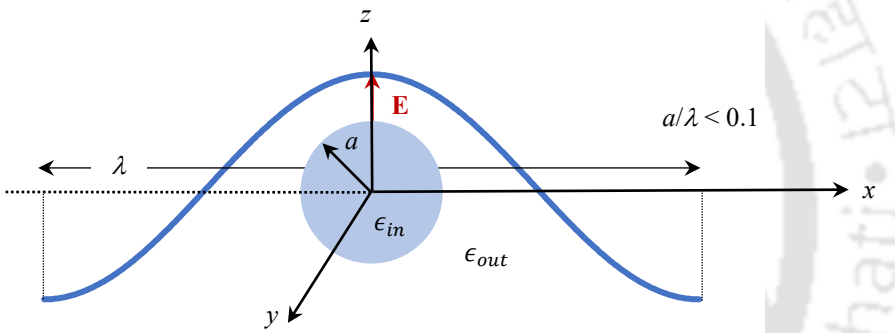

Figure 1.3: A metal sphere of radius *a,* embedded in a dielectric medium with permittivity ϵ_o, is illuminated by a linearly (z-) polarized light of wavelength λ propagating along the x-axis. Here, $a/\lambda<0.1$, that corresponds to the quasi-static field case.

(Fig. 1.3). The electric field **E** associated with the optical beam coming out from the laser is generally expressed as:

$$\mathbf{E} = E_x\hat{x} + E_y\hat{y} + E_z\hat{z} \tag{1.5}$$

where $\hat{x}, \hat{y}, \hat{z}$ are unit vectors along the Cartesian axes *x*, *y*, *z*. For the *z*-polarized light, $E_x = E_y = 0$ and $\mathbf{E} = E_z\hat{z}$. Thus, for the light polarized along the *z*-axis and propagating along the *x*-axis, E_z is given as:

$$E_z = E_0 \cos(kx - \omega t) \tag{1.6}$$

Applying the long wavelength approximation ($\lambda > 400$ nm, hence $kx << \omega t$) and assuming the metal nanosphere is much smaller than the wavelength ($a/\lambda < 0.1$) as required for the case of metal nanoparticle, the electric field associated with the laser output ($\mathbf{E} = E_z\hat{z} = E_0\hat{z} = \mathbf{E}_o$) can be considered spatially independent for distances comparable to the size of the metal sphere. Additionally, the externally applied field $\mathbf{E}_o$ remains nearly constant over time ensuring that:

$$\frac{\partial \mathbf{E}}{\partial t} = 0 \text{ and } \frac{\partial \mathbf{B}}{\partial t} = 0 \tag{1.7}$$

Thus, the electric field around the metal nanoparticle can be treated as quasi-static [23]. As a result, Maxwell's equations simplify to the fundamental equations of electrostatics and magnetostatics:

$$\nabla . \mathbf{E} = \frac{\rho}{\epsilon_0} \tag{1.8}$$

$$\nabla \times \mathbf{E} = 0 \tag{1.9}$$

$$\nabla . \mathbf{B} = 0 \tag{1.10}$$

$$\nabla \times \mathbf{B} = \frac{\mathbf{j}}{\epsilon_0 c^2} \tag{1.11}$$

where ρ is volume charge density and $\mathbf{j}$ is volume current density. In order to determine the electric field $\mathbf{E}(x,y,z)$, inside as well as outside the metal sphere, electrostatic equation 1.8 needs to be solved. Since the metal sphere is a conductor with no net charge density (i.e. $\rho = 0$), Eq. (1.8) reduces to:

$$\nabla . \mathbf{E} = \mathbf{0} \tag{1.12}$$

In order to determine the electric field, the scalar potential $\Phi(x,y,z)$ is determined first. From the scalar potential, the electric field can be derived as:

$$\mathbf{E} = -\nabla\Phi \tag{1.13}$$

The scalar potential, $\Phi(x,y,z)$, can be determined from the Laplace's equation:

$$\nabla^2\Phi = 0 \tag{1.14}$$

Laplace's equation in spherical coordinates is given by:

$$\nabla^2(r,\theta,\phi)\Phi_{l,m}(r,\theta,\phi) = 0 \tag{1.15}$$

Using the separation of variables method and applying appropriate boundary conditions, solution of the Laplace's equation is obtained as:

$$\Phi_{l,m}(r,\theta,\phi) = \left[A_l r^l + B_l r^{-(l+1)}\right] P_l^{|m|}(\cos\theta)\, e^{im\phi} \tag{1.16}$$

with $l = 0, 1, 2, \ldots$ and $m = -l, -l+1, \ldots -2, -1, 0, 1, 2, \ldots l-1, l$. Here, $P_l^{|m|}(\cos\theta)$ are associated Legendre functions. As shown in Fig. 1.3, the metal sphere irradiated by quasi-static field exhibits azimuthal symmetry; and hence, the solutions must be independent of the azimuthal angle ϕ. This corresponds to the $m = 0$ in Eq. (1.16).

In general, the electric field inside the sphere differs from the electric field outside the sphere. Further, the incident electric field remains unaffected by the metal sphere as one moves far from this sphere (at $r \to \infty$). Additionally, the field at the center of the sphere ($r \to 0$) should have some finite (nonzero) value [23]. These conditions can be mathematically expressed as:

1) $\mathbf{E}_{in} \neq \mathbf{E}_{out}$

2) as $r \to \infty$, $\mathbf{E}_{out} \to E_0\hat{z}$ (1.17)

3) as $r \to 0$, $\mathbf{E}_{in} \to$ finite

Using the above conditions, Eq. (1.16) yields $A_0 = B_0 = 0$ for $m = 0$, $l = 0$. In order to solve Eq. (1.16) for $m = 0$, $l = 1$, let us write Eq. (1.13) in Cartesian coordinates:

$$\mathbf{E}(x,y,z) = -\left(\frac{\partial}{\partial x}\hat{x} + \frac{\partial}{\partial y}\hat{y} + \frac{\partial}{\partial z}\hat{z}\right)\Phi_{10}(x,y,z) \tag{1.18}$$

Substituting the expression of Φ_{10} from Eq. (1.16) in Eq. (1.18) and solving in Cartesian coordinate gives the electric field as,

$$\mathbf{E}(x,y,z) = -A_1\hat{z} - B_1\left[\frac{\hat{z}}{(x^2+y^2+z^2)^{3/2}} - \frac{3z(x\hat{x}+y\hat{y}+z\hat{z})}{(x^2+y^2+z^2)^{5/2}}\right] \tag{1.19}$$

Let is define the expression of electric field inside and outside the metal sphere as,

$$\mathbf{E}_{in}(x,y,z) = -A_{1,in}\hat{z} - B_{1,in}\left[\frac{\hat{z}}{(x^2+y^2+z^2)^{3/2}} - \frac{3z(x\hat{x}+y\hat{y}+z\hat{z})}{(x^2+y^2+z^2)^{5/2}}\right] \quad (1.20a)$$

$$\mathbf{E}_{out}(x,y,z) = -A_{1,out}\hat{z} - B_{1,out}\left[\frac{\hat{z}}{(x^2+y^2+z^2)^{3/2}} - \frac{3z(x\hat{x}+y\hat{y}+z\hat{z})}{(x^2+y^2+z^2)^{5/2}}\right] \quad (1.20b)$$

The term in the square bracket of Eq. (1.20a) goes to ∞ as $r \rightarrow 0$. Thus, applying the condition "3" of Eq. (1.17) yields

$$B_{1,in} = 0 \quad (1.21)$$

Similarly, the term in the square bracket of Eq. (1.20b) goes 0 as $r \rightarrow \infty$. Thus, applying the condition "2" of Eq. (1.17) yields

$$-A_{1,out} = E_0 \quad (1.22)$$

Remaining constants, namely, $A_{1,in}$ and $B_{1,out}$, are determined by applying the following continuity conditions at the surface of the metal sphere ($r = a$):

1) $\epsilon_{in}\mathbf{E}_{in} = \epsilon_{out}\mathbf{E}_{out}$

2) E_θ and E_ϕ are continuous

Applying these continuity conditions, gives:

$$-A_{1,in} = \left[\frac{3\epsilon_{out}}{2\epsilon_{out}+\epsilon_{in}}\right]E_0 \quad (1.23)$$

$$B_{1,out} = a^3E_0\left[\frac{\epsilon_{in}-\epsilon_{out}}{\epsilon_{in}+2\epsilon_{out}}\right] \quad (1.24)$$

Substituting the values of $A_{1,in}$, $B_{1,in}$, $A_{1,out}$ and $B_{1,out}$ in Eq. (1.20a) and Eq. (1.20b), the resulting solution for the electromagnetic field inside the nanoparticle is expressed as:

$$\mathbf{E}_{in}(x,y,z) = \left(\frac{3\epsilon_{out}}{2\epsilon_{out}+\epsilon_{in}}\right)E_0\hat{z} \quad (1.25)$$

Whereas, the resulting solution for the electromagnetic field outside the nanoparticle is expressed as:

$$\mathbf{E}_{out}(x,y,z) = E_0\hat{z} - \left[\frac{\epsilon_{in}-\epsilon_{out}}{\epsilon_{in}+2\epsilon_{out}}\right]a^3E_0\left[\frac{\hat{z}}{r^3} - \frac{3z}{r^5}(x\hat{x}+y\hat{y}+z\hat{z})\right] \tag{1.26}$$

where the first term $E_0\hat{z}$ is the incident field. The dielectric constant ϵ_{in} varies significantly with wavelength, and thus, the expression in the first square bracket of the second term in Eq. (1.26) determines the dielectric resonance condition of the metal particle. When the dielectric constant of the metal nanoparticle is approximately equal to $-2\epsilon_{out}$, the electromagnetic (EM) field is amplified relative to the incident field. For metals like silver and gold nanoparticles, this resonance condition is satisfied in the visible region of the spectrum. Additionally, the size of the nanoparticle (a) and the external dielectric constant (ϵ_{out}) also play crucial roles in determining the EM field outside the particle. The extinction spectrum of the metal nanoparticle, as determined using the electromagnetic field outside the metal nanoparticle ($\mathbf{E}_{out}$), is expressed as [23], [24]:

$$E(\lambda) = \frac{24\pi^2 N a^3 \epsilon_{out}^{3/2}}{\lambda \ln(10)}\left[\frac{\epsilon_i(\lambda)}{(\epsilon_r(\lambda)+\chi\epsilon_{out})^2+\epsilon_i(\lambda)^2}\right] \tag{1.27}$$

Here, ϵ_r and ϵ_i are the real and imaginary components of the metal dielectric function, respectively; N represents number of polarizable particles that interact with the applied electric field. The value of χ is 2 in case of sphere, but it takes on values as large as 20 to account the particle geometries with high aspect ratios [25].

In addition to the extinction of the metal nanoparticles, it is important to understand how the LSPR is used for both sensing/spectroscopic applications. For example, the LSPR extinction (or scattering) wavelength maximum, λ_{max}, is sensitive to the refractive index. Thus, any change in the local environment, such as the adsorption of a species onto the nanoparticle surface, can induce a shift in λ_{max}. To analyse this effect, let us consider the situation where a layer of thickness d and of the refractive index n_A is introduced onto the nanoparticle surface. Beyond this layer (i.e., at distances greater than d), the surrounding medium is assumed to have a refractive index of n_E. Thus, the refractive index variation can be expressed as:

$$n(z) = \begin{cases} n_A & 0 \le z \le d \\ n_E & d \le z \le \infty \end{cases} \tag{1.28}$$

The wavelength shift in the LSPR spectrum that results from the adsorption layer introduced onto the metal nanoparticle surface is expressed as [23]:

$$\Delta\lambda_{max} = m\left(n_{final} - n_{initial}\right) \tag{1.29}$$

Here, m represents the bulk refractive index sensitivity of the nanoparticle. $n_{initial}$ is defined as the refractive index of the surrounding medium before the introduction of adsorption layer around the nanoparticles (i.e., n_E), whereas, n_{final} is defined as the refractive indices of the final states, that is, after the introduction of the adsorption layer. Importantly, n_{final} is very complex as it comprises of a combination of the refractive indices of the adsorbed layer and the surrounding (external) medium. Hence, n_{final} can be represented by effective refractive index, n_{eff} (not to be confused with the effective refractive index of the guided modes within an optical fiber). This effective refractive index is defined as the *z*-dependent refractive index (Eq. 1.28) normalized by the relative field intensity (I/I_0), and is given by [23]:

$$n_{eff} = \frac{2}{l_d}\int_0^{\infty} n(z)exp\left(-\frac{2z}{l_d}\right)dz \tag{1.30}$$

Here, the field intensity (I) corresponds to the electromagnetic field that probes the local refractive index. This field can be approximated as an exponentially decaying field with a characteristic length l_d [23]:

$$E(z) = E_0 exp\left(-\frac{z}{l_d}\right) \tag{1.31}$$

Evaluating this integral in Eq. (1.30) while substituting $n(z)$ from Eq. (1.28) gives:

$$n_{eff} = n_A\left[1 - exp\left(-\frac{2d}{l_d}\right)\right] + n_E exp\left(-\frac{2d}{l_d}\right) \tag{1.32}$$

Substituting n_{eff} for n_{final} and n_E for $n_{initial}$ in Eq. (1.29), yields:

$$\Delta\lambda_{max} = m\left\{n_A\left[1 - exp\left(-\frac{2d}{l_d}\right)\right] + n_E exp\left(-\frac{2d}{l_d}\right) - n_E\right\} \tag{1.33}$$

This relation describes the dependence of λ_{max} on the changes in the local environment, such as the adsorption of a species onto the nanoparticle surface. Upon simplification, it can be written as:

$$\Delta\lambda_{max} = m\Delta n\left[1 - exp^{(-2d/l_d)}\right] \quad (1.34)$$

where $\Delta n = n_A - n_E$. Thus, the resonance wavelength of LSPR is highly sensitive to even the slightest changes in the surrounding medium. This characteristic of the resonance wavelength of LSPR enables the development of sensors with exceptional sensitivity, potentially achieving single-molecule detection [26]. By combining the LSPR technique with fiber optics it becomes possible to harness the strengths of both the technologies for the development of optical fiber sensors. To develop an LSPR-based optical fiber sensor, the cladding of the optical fiber is removed in a small section. This decladded section is coated with a layer of metal nanostructures (e.g., gold nanoparticles). The sensing medium (dielectric region) surrounds this nanostructure-coated area. A broadband light source is used for launching light into the fiber. The surface plasmons in the metal nanostructures are excited by the evanescent field of light propagating through the fiber core. At resonance, transmitted light within a specific spectral range is absorbed by the nanoparticle layer, resulting in a distinctive dip in the transmitted (output) spectrum. When the sensing region is exposed to the analyte, it alters the refractive index of the surrounding medium near the gold nanoparticles, leading to a shift in the LSPR resonance wavelength in the transmitted spectrum.

1.3 Environmental monitoring and Homeland security

Environmental contamination by toxic substances is a growing concern, significantly impacting, both, human health and ecosystems. Rapid industrialization, technological advancements, population growth, and the continual discharge of agricultural and domestic waste have introduced a wide range of pollutants into aquatic environments. Of particular concern are heavy metal ions, which are persistent, toxic, and bio accumulative. These pollutants can travel through the food chain, magnifying their effects. Heavy metals such as arsenic, mercury, lead, cadmium, and fluoride are particularly harmful because they are non-degradable and pose serious health risks [27]. Mercury ion (Hg^{2+}), among the most toxic of these ions, is primarily introduced through industrial effluents. Elevated mercury levels in water can cause severe health conditions, including Hunter-Russell syndrome, Minamata disease, and kidney damage [28]. The World Health Organization (WHO) has set a safety

threshold of 6 parts per billion (ppb) for mercury ion in drinking water. Similarly, arsenic (As^{3+}) is another highly toxic heavy metal ion that is introduced mainly into water bodies through natural geothermal processes. Prolonged consumption of arsenic contaminated water can result in arsenic poisoning, significantly increasing the risk of cancers, such as skin, lung, kidney, and bladder cancer [29]. The WHO recommends a maximum allowable limit of 10 µg/L (10 ppb) for arsenic in drinking water to minimize these health risks. Considering these serious health risks posed by Hg^{2+} and As^{3+}, it is essential to prioritize the development of reliable and sensitive detection methods for these water contaminants.

Several analytical techniques have been developed to detect water contaminants like Hg^{2+} and As^{3+}. These include atomic absorption spectrometry [30, 31], inductively coupled plasma mass spectrometry (ICPMS) [32, 33], high-performance liquid chromatography (HPLC) [34, 35], colorimetric [36, 37], and electrochemical methods [38]. These methods are highly accurate and sensitive. However, they have several drawbacks such as complex mechanisms, making them difficult to operate. Additionally, they are time-consuming and expensive. Furthermore, these techniques require bulky instrumentation and skilled personnel. In contrast, Surface Plasmon Resonance (SPR) and Localized Surface Plasmon Resonance (LSPR) techniques have emerged as a promising alternative for heavy metal ion detection due to their simplicity, rapid response, cost effective, easy sample preparation and high sensitivity. Both LSPR and SPR are highly responsive to changes in localized refractive index, thereby showing a corresponding shift in the resonance wavelength. Therefore, this field has caught the attention of researchers and hence several LSPR and SPR based Hg^{2+} and As^{3+} have been reported. For example, Taniguchi et al. [39] developed a prism-based SPR sensor employing DNA elements for detecting Hg^{2+} ions. The sensor demonstrated a linear response within 10-10^4 µg/L and achieved a limit of detection (LOD) of 5 µg/L (5 ppb). Fauzi et al. [40] proposed another prism-based SPR sensor using chitosan/maghemite as the sensing material. It exhibited a dynamic range of 0.01–0.5 parts per million (ppm) and an LOD of 0.01 ppm (10 ppb). Castillo et al. [41] proposed a liquid-phase based LSPR Hg^{2+} sensor utilizing gold nanoparticles as the sensing material. The sensor showed a sensitivity of 0.026 µg/L and an LOD of 172 ng/L (172 ppb). Jiang et al. [42] presented a prism-based SPR sensor using 1,6-hexanedithiol as the sensing material. This sensor displayed a linear response from 0–100 mg/L, a sensitivity of 1.25×10^{-2} °/mg/L, and an LOD of 80 ppb, along with good selectivity towards Hg^{2+}. Huang et al. [43] proposed a liquid-phase based LSPR Hg^{2+} sensor employing silver/gold nanocages.

The sensor exhibited a linear response in the range of 0.01–0.5 ppm and an LOD of 5 ppb. On the other hand, Pratima et al. [44] proposed an As^{3+} sensor employing the prism-based SPR technique with a self-assembled monolayer of β-mercaptoethanol on a gold substrate. This sensor exhibited a linear response within the range of 0-2.5 µg/ml As^{3+} concentration, a detection limit of 0.01 µg/ml (10ppb), and a rapid response time of 30 s. Anindita et al. [45] presented a liquid-phase based LSPR As^{3+} sensor utilizing gold nanorods. This sensor exhibited a linear dynamic range of 10-500 ppb with a detection limit of 10 ppb. These techniques demonstrated a good LOD for Hg^{2+} and As^{3+} ions. However, most of the reported sensors do not meet the regulatory standards set by the WHO for Hg^{2+} and As^{3+} ions in drinking water. Consequently, further improvements are necessary to achieve the ultra-low LOD required to meet the regulatory standards set by WHO for Hg^{2+} and As^{3+} detection in drinking water. Furthermore, these LSPR and SPR methods lack crucial features such as remote sensing and multiplexing capabilities, which are essential for practical and efficient real-field applications.

In the past decade, there has been a global effort to strengthen counterterrorism measures, driven by the increasing use of explosives by terrorists. This has highlighted the urgent need for reliable detection methods to ensure civilian security. High explosives such as 1,3,5-Trinitro-1,3,5-triazinane (RDX), 2,4,6-Trinitrotoluene (TNT), and related compounds, including Trinitrophenol (TNP) or picric acid (PA), 2,4-Dinitroanisole, 2,4-Dinitrotoluene (DNT), and 4-Nitrotoluene (NT), have drawn significant attention for defence and security applications. Among these, TNP is an extremely powerful explosive, even stronger than TNT [46]. Additionally, TNP is highly soluble in water, and even trace concentrations can be extremely toxic. Exposure to TNP can result in a range of health problems, including damage to the eyes, skin, and respiratory system, as well as chronic issues like anemia and cancer [47]. Despite these adverse consequences, the utilization of TNP remains unavoidable in sectors such as dye manufacturing, pharmaceuticals, rocket fuel production, and chemical laboratories. Consequently, due to its widespread application across various industries and its high-water solubility, TNP is polluting water. TNP's high solubility in water also enables its infiltration into groundwater near landmines and underwater mine sites. Thus, detecting TNP in groundwater is crucial for locating unexploded landmines, underwater mines, and determining water contamination at war sites, military bases and industrial zones to ensure public safety and to protect human health and the environment [48]. Regulatory standards, such as the "Surface Water Environmental Quality Standards" (GB3838-2002), limit TNP concentrations

in water to 0.5 mg/L (ppm). This emphasizes the need for precise TNP detection methods in aqueous environments. Developing highly selective sensors capable of detecting TNP at very low concentrations is essential for safeguarding environmental health and public safety.

For detecting nitro-explosives such as TNP, a variety of analytical techniques are available. These include high-performance liquid chromatography [49], surface-enhanced Raman spectroscopy [50], mass spectrometry [51], Raman scattering [52], colorimetry [53], [54], and electrochemical analysis [55] – [57], etc. While these techniques offer high accuracy and sensitivity, they also have several drawbacks that hinders their widespread application. One major drawback is their complex mechanisms, which makes them challenging to operate. Additionally, these methods are expensive and time-consuming. Furthermore, these techniques require bulky instrumentation, which makes them impractical for onsite detection. Moreover, these techniques require skilled personnel, which further restrict their widespread application. In contrast, fluorescent probes have emerged as a promising alternative for detecting nitro explosives due to their simplicity, rapid response, portability, straightforward sample preparation, and high sensitivity. Consequently, this area has caught significant attention from researchers, leading to the development of several fluorescent sensors for detecting TNP. For instance, Kumari et al. [48] reported a fluorescence quenching based TNP sensor using two fluorescent coumaryl-linked imidazolium salts. The sensors exhibited detection limits of 107 nM (24.41 ppb) and 87 nM (19.93 ppb) with quenching constants of 2.2×10^4 M^{-1} and 5×10^4 M^{-1}, respectively. Both the fluorescent sensors demonstrated selectivity towards TNP. Similarly, Fan et al. [58] used carbon dots as label-free fluorescence probes. Sensor demonstrated a detection limit of 51 nM (11.68 ppb) and a linear range of 0.1–26.5 µM. The sensor also exhibited a fast response time of 10 s and showed selectivity towards TNP. Luo et al. [59] developed a turn-off fluorescence sensor using a 2-pyridone derivative (D-TPCA). The sensor demonstrated selective detection of TNP with a detection limit of 56 nM (12.83 ppb). Further, Li et al. [60] proposed a membrane-based fluorescence sensor employing 5-(-N-carbazole styryl)-1,3-dimethyl-barbituric acid and polystyrene. The sensor showed a selective and sensitive response with linear range from 0-140 µM and a detection limit of 228 ppb. In another work, Dong et al. [61] employed iridium (III) complex containing carbazole moieties for sensing TNP. Sensor demonstrated a linear response in the range of 0-314 µM TNP concentration with a quenching constant of 1.9×10^4 M^{-1} and a limit of detection of 10 µM (2291 ppb). Guo et al. [62] developed a fluorescence sensor employing pyrazoline derivatives for the

detection of TNP. The sensor exhibited a selective and sensitive detection of TNP with a quenching constant of 4.36×10^4 M^{-1} and a limit of detection 0.68 µM (155.78 ppb). Moreover, Remani et al. [63] utilized solgel ceria nanoparticles synthesized in the presence of fenugreek extract for fluorescence detection of TNP in water. Sensor exhibited linear response in the range of 0.33- 41.6 µM TNP concentration with a quenching constant of 57.54×10^4 M^{-1} and a very low limit of detection of 0.33 µM (75.6 ppb). Among these reported sensors, many of the them reported LOD that exceeds the surface water environmental quality standards threshold for TNP in water. This makes them not suitable for effective monitoring of TNP in water. Additionally, despite the promising results, these fluorescent probes have certain limitations. One of the major drawbacks is fluorescence quenching upon interaction with TNP, meaning that once the probe detects TNP, their fluorescence signal diminishes, rendering them non-reusable. Additionally, they also face selectivity issues, and difficulties in on-site detection applications. The main unresolved challenge in the field of explosive sensing is the remote detection of trace amounts of explosives, such as landmines, which remains exceptionally difficult.

Optical fiber sensors are an ideal solution for detecting water contaminants, such as As^{3+} and Hg^{2+}, as well as explosives like TNP. They effectively overcome all the limitations (mentioned above) of optical sensing methods, such as LSPR, SPR, and fluorescence. Optical fiber sensor offer high sensitivity which allows the detection of minute changes in Hg^{2+}, As^{3+} and TNP concentration, enabling the sensor to achieve lower LOD. These sensors also exhibit rapid response times, making them ideal for real-time monitoring. Additionally, optical fiber sensors are compact and cost-effective, facilitating their deployment in real-field applications. Their ability to support remote sensing further enhances their practicality. These features collectively make optical fiber sensors highly suitable for water contamination (Hg^{2+} and As^{3+}) and explosive (TNP) detection, offering a reliable and efficient solution for environmental monitoring and homeland security. However, not many Hg^{2+}, As^{3+} and TNP optical fiber sensors are reported so far. For example, Yuan et al. [64] proposed an SPR based optical fiber Hg^{2+} sensor utilizing marcaptopyridine functionalized gold nanoparticles as the sensing material. The sensor exhibited high selectivity towards Hg^{2+} ions with a linear response in the range of 0-100 nM, an LOD of 3.34 nM (1.6 ppb) and response time of 30 min. Prakashan et al. [65] proposed an SPR based optical fiber Hg^{2+} sensor using copper silver core-shell nanoparticles as the sensing material. The sensor showed piece-wise linear response in the

ranges of 0-1 μM and 1-1000 μM, with an LOD of 10 nM (2 ppb) and exhibited selective response towards Hg^{2+}. Yuan et al. [66] developed an SPR based optical fiber Hg^{2+} sensor employing thymine-functionalized gold nanoparticles as the sensing material. The sensor demonstrated linear response in the range of 0-20 μM with an LOD of 9.98 nM (1.99 ppb) and also offered high selectivity towards Hg^{2+}. In another study, Raj et al. [67] proposed an SPR based optical fiber Hg^{2+} sensor using gold nanoparticles PVA hybrid as the sensing material. The sensor showed linear response in the range of 0-25 μM with an LOD of 1 μM (200 ppb). Zhong et al. [68] proposed an LSPR based optical fiber Hg^{2+} sensor using chitosan/poly-acrylic acid bilayer as the sensing material. The sensor exhibited a linear response in the range of 0-30 μM with an LOD of 0.52 μM (104.3 ppb) and also showed selectivity towards Hg^{2+}. Boruah et al. [69] proposed an LSPR based optical fiber Hg^{2+} sensor utilizing chitosan-mediated silver nanoparticles as the sensing material. The sensor exhibited linear response in the range of 0-10 ppb, with an LOD of 1.5 ppb, response time of 11 min and also offered high selectivity. Similarly, Shukla et al. [70] presented an LSPR based optical fiber Hg^{2+} sensor employing glucose-capped silver nanoparticles as the sensing material. This sensor showed a non-linear response in the range of 0-200 ppb, with an LOD of 2 ppb and exhibited high selectivity towards Hg^{2+}. Further, Khan et al. [71] proposed an intensity modulation based optical fiber Hg^{2+} sensor. The sensor used multi-walled carbon nanotubes as the sensing material. The sensor exhibited a linear response in the range of 0-5 ppm, with an LOD of 0.1 ppm (100 ppb) and a fast response time of 6.3 s. Wu et al. [72] presented an SPR based optical fiber Hg^{2+} sensor, using sodium sulfide as the sensing material. This sensor showed a linear response in the range of 10-60 nM, with an LOD of 8.15 nM (1.63 ppb) and exhibited high selectivity towards Hg^{2+}. Nguyen et al. [73] proposed a turn-on fluorescence based optical fiber sensor for detecting Hg^{2+} utilizing fluorescent polymeric material as the sensing material. The sensor exhibited a linear range of 0-28 μM, with an LOD of 0.15 μM (30.08 ppb), response time of 11 min and also exhibited high selectivity towards Hg^{2+}. On the other hand, Sonika et al. [74] proposed an SPR based optical fiber sensor for As^{3+} detection, using α-Fe_2O_3/SnO_2 core-shell nanostructure as the sensing material. This sensor exhibited highly selective and sensitive non-linear response within the 0-100 μg/L As^{3+} concentration range, with an LOD of 0.47 μg/L (0.47 ppb) and a rapid response time of 10 s. Shukla et al. [75] presented an LSPR based optical fiber sensor using arsenic-specific aptamer immobilized on cysteamine-capped gold nanoparticles as the sensing material. This sensor showcased a low LOD of 1 ppb. In another study, the same research group developed an evanescent wave absorbance based optical fiber

arsenic ion sensor [76]. This sensor employed aptamer bound polyaniline as the sensing material. The sensor offered a LOD of 1 ppb with high selectivity towards arsenic ion. Among the above reported Hg^{2+} and As^{3+} ion sensors, a substantial number of sensors do not meet the regulatory standards set by the WHO for Hg^{2+} and As^{3+} ions in drinking water. This limits the suitability and applicability of these sensors for the detection of Hg^{2+} and As^{3+} in drinking water. On the other hand, sensors reported with LODs within the acceptable regulatory limits, either lack selectivity or exhibit slow response time. Furthermore, only a few of the above reported sensors demonstrate reusability, which is critical for cost-effective and sustainable use. Thus, there is a significant need to develop optical fiber sensors for Hg^{2+} and As^{3+} detection that offer exceptionally low LODs, significantly below the regularity standards, to facilitate early detection before these contaminants reach hazardous levels. Additionally, these sensors should also offer high selectivity, fast response time and reusability for effective real field applications.

On the other hand, till date, only two optical fiber-based TNP sensors are reported. For instance, Zhao et al. [77] developed a metal-organic framework integrated hydrogel optical fiber as a photoluminescence sensing platform. The sensor demonstrated a selective and sensitive linear response in the range of 0-69 μM with the quenching constant of 5.7×10^4 $M^{-1}$and LOD as low as 5.7 ppm (5700 ppb). In another work, Dasary et al. [78] also proposed an optical fiber sensor using N,N-Diisopropylcarbodiimide (DPC). The sensor exhibited a selective and sensitive linear response in the range of 0-4000 nM with an LOD of 25 ppb. However, these sensors demonstrated good LOD, there is significant scope for improvement in terms of achieving even lower detection limits. Achieving ultra-low LOD is critical for detecting trace amount of explosive (TNP), enabling the early identification of landmines and water contamination. Additionally, these sensors lacked reusability, limiting their practicality. Therefore, there is a significant need for the development of an optical fiber sensor that offers an exceptionally low LOD, high selectivity, optimal sensitivity, reusability, and fast response time for real-field applications.

1.4 Objective and summary of the thesis

The main objective of this thesis is to develop optical fiber sensors for detecting water contaminants, specifically Hg^{2+}, As^{3+}, and explosive (TNP), with exceptionally low LOD, optimal sensitivity, high selectivity, fast response time, and high degree of repeatability and

reliability. To achieve these objectives, novel sensors are developed, enabling precise and selective trace detection of Hg^{2+}, As^{3+}, and TNP. The optical fiber sensors were developed employing sensing techniques such as: intensity modulation through evanescent wave absorption and wavelength modulation using localized surface plasmon resonance. The research begins by developing a U-shaped optical fiber LSPR sensor for Hg^{2+} detection using graphene oxide and chitosan (GO-CS) composite as the sensing material. To develop the sensor, gold nanoparticles (AuNPs) were first coated onto the centrally decladded U-shaped core of the plastic-clad silica (PCS) optical fiber. The AuNPs-coated U-shaped optical fiber is then further coated with a layer of GO-CS composite using the dip coating method. This sensor demonstrates excellent sensitivity of 0.0728 nm/ppb, a remarkably low LOD of 0.29 ppb and high selectivity towards Hg^{2+}. It also exhibits a fast response time of 0.6 s. In the next work, another optical fiber Hg^{2+} sensor is developed to further enhance sensitivity and reduce the LOD by incorporating carbon nanotube/polyvinyl alcohol (CNT/PVA) nanocomposite film, while maintaining the same fiber configuration. Optimizing the sensing film configuration results in an enhanced sensitivity of 0.2458 nm/ppb over the range of 0-30 ppb Hg^{2+} concentration. The sensor also demonstrated an average response time of the sensors is 0.4s and an improved LOD of 0.08 ppb, while maintaining high selectivity towards Hg^{2+} detection. Next, an optical fiber LSPR sensor for detecting another highly toxic water contaminant As^{3+} ion is developed, employing Al_2O_3/GO nanocomposite as the sensing material. This sensor shows a high sensitivity of 0.217 nm/ppb and an LOD of 0.09 ppb, with a rapid response time of 0.5 s and high selectivity for As^{3+} ions. To further enhance sensing performance, another As^{3+} sensor is developed using lauryl sulphate functionalized gold nanoparticles. In this case, the gold nanoparticles serve both as the LSPR generator and the sensing material. This sensor achieves an enhanced sensitivity of 0.3073 nm/ppb, an even lower LOD of 0.06 ppb while maintaining a response time of 0.5 s, along with high selectivity. Following this, an optical fiber TNP sensor is developed, utilizing intensity modulation via evanescent wave absorption. A thin polymer film (PFTPA) of the appropriate thickness and composition is synthesized over the centrally decladded region of a straight PCS multimode optical fiber. The sensor exhibits a linear response between 0-50 ppb with high sensitivity of 0.0032/ppb, a remarkably low LOD of 1.06 ppb and shows high selectivity towards TNP. Further, the sensor exhibits an average response and recovery time of 2 s. In order to further enhance the sensing performance, another TNP sensor is developed using a LSPR configuration, incorporating zinc oxide quantum dots (ZnO QDs) as the sensing film. This sensor exhibits an improved LOD of 0.19 ppb and a linear

response over the same 0-50 ppb range, with a high sensitivity of 0.1288 nm/ppb. However, a slightly longer response time of 2 s is observed. It also demonstrates high selectivity towards TNP. It is worth mentioning that, all the novel sensors developed in this research exhibit high degree of reversibility, repeatability, stability and reliability. Furthermore, all the proposed sensors are tested not only in the controlled lab environments but also in real-world applications, where they are employed to detect Hg^{2+}, As^{3+}, and TNP in real water samples.

1.5 Organization of the thesis

Chapter-1

The main objective of this chapter is to establish the foundation of the research work presented in this thesis. It begins with discussing about the importance of optical fiber technology for sensing applications. The chapter then provides a detailed discussion about intensity modulation through evanescent wave and localized surface plasmon resonance techniques. In the next section, the chapter then discusses the importance of water contamination (Hg^{2+}, As^{3+}), and explosive (TNP) sensing. The chapter then provides a detailed literature review of the existing research related to water contamination (Hg^{2+}, As^{3+}), and explosive (TNP) detection and their limitations. The last section establishes the objectives of this thesis work and the methodologies employed to achieve those objectives.

Chapter-2

The main objective of research carried out and reported in Chapter 2 is to develop a novel optical fiber Hg^{2+} sensor with optimal sensitivity, a remarkably low LOD, high selectivity, and rapid response time. To fulfill the objective, the proposed sensor employs the LSPR technique using graphene oxide and chitosan (GO-CS) composite as the sensing material. It is worth mentioning that GO-CS composite is used for the first time to realize an optical fiber based Hg^{2+} sensor to the best of authors' knowledge. For the development of the sensor, first the gold nanoparticles (AuNPs) were coated onto the centrally decladded U-shaped core of the PCS optical fiber followed by the coating of GO-CS composite. AuNPs was synthesized by chemical reduction of $HAuCl_4$ using trisodium citrate [79]. GO was then synthesized using modified Hummer's method [80]. After that, GO-CS composite solution was prepared by dissolving the appropriate amount of chitosan powder and GO in a 2% acetic acid solution. In the process of optimizing sensor's response, effects of composition of the sensing film were studied. For that, multiple probes were prepared by varying the sensing film configuration. To

examine the different sensing probes having different sensing film compositions, the sensing probes were characterized in an in-house developed flow-cell (dimension 5 cm × 5 cm × 4 cm). The optical fiber sensor was connected to a Broad Band Source (Ocean Optics, HL-2000-FSHA) through one arm and to a spectrometer (Ocean Optics, RH4000) through the other arm, using a subminiature version A (SMA) connector. The spectrometer was interfaced with a computer through MATLAB program for real-time monitoring of the sensor. Hg^{2+} solutions with concentrations ranging from 0ppb to 200ppb were used to immerse the sensing region of the fiber for characterization of the sensing probe. The transmittance of the optical fiber sensor was measured for each solution concentration using the spectrometer. Experimental analysis indicates that the optimal performance was achieved with a sensing film composition of 0.2 g of GO in 0.5 g of chitosan. Notably, the sensor exhibits a linear response across the 0–200 ppb range, with a sensitivity of 0.0728 nm/ppb for Hg^{2+} concentration and an impressively low LOD of 0.29 ppb. The achieved LOD is substantially lower than the regulatory threshold set by the WHO for Hg^{2+} in drinking water, making the proposed sensor highly suitable for Hg^{2+} detection in drinking water. The proposed sensor also exhibits high selectivity towards Hg^{2+}. Furthermore, to examine the sensor's reversibility and repeatability, it was subjected to cyclic exposure to Hg^{2+} solutions ranging from 10 ppb to 200 ppb. The results confirmed consistent performance during both forward (10 ppb to 200 ppb) and reverse (200 ppb to 10 ppb) Hg^{2+} concentration changes. Additionally, the sensor demonstrates an average fast response time of 0.6 seconds. The proposed sensor was further employed to detect mercury ions in real water samples, and its results were in strong agreement with the standard ICPMS method, showing relative percentage difference (RPD) values of less than 2%, thereby validating its accuracy. Additionally, the sensor underwent rigorous stability and reliability testing. In short-term stability tests, the LSPR spectrum was continuously recorded at 1-minute intervals over 16 minutes while exposing the sensor to three different Hg^{2+} concentrations (20 ppb, 100 ppb, and 200 ppb). The maximum standard deviation observed in the resonance wavelength was ±0.083 nm demonstrating the sensor's high accuracy with a maximum resolution of ±1.14 ppb. For long-term stability and reliability test, the optimized optical fiber Hg^{2+} sensing probe was tested over a span of 18 days, with measurements taken at 5-day intervals. The fiber sensor's output was recorded for three different Hg^{2+} concentrations (20 ppb, 100 ppb, and 200 ppb) on three separate days. The experimental results showed a maximum variation of just 0.022% in the sensor’s output compared to the first day, highlighting the exceptional repeatability and reliability of the developed optical fiber Hg^{2+} sensor. Although this sensor exhibited high

sensitivity with a low LOD, there remains potential for further enhancement in improving the sensitivity and reducing the LOD. This serves as the foundation for the research presented in the following chapter.

Chapter-3

To further enhance the sensing performance for Hg^{2+} detection, another novel LSPR-based optical fiber sensing probe was developed using a carbon nanotube and polyvinyl alcohol (CNT/PVA) nanocomposite as the sensing film. This chapter focuses on designing a novel optical fiber Hg^{2+} sensor with optimal sensitivity, ultra-low LOD, high selectivity, and rapid response time. The sensor utilizes the LSPR technique, incorporating CNT/PVA nanocomposite as the sensing material. It is important to mention that CNT/PVA nanocomposite is used for the first time to realize an optical fiber mercury ion sensor to the best of authors' knowledge. The sensor preparation process begins with coating AuNPs onto the centrally decladded U-shaped core of a PCS optical fiber, followed by the deposition of the CNT/PVA nanocomposite film. The AuNPs were synthesized using the method described in Chapter 2. To optimize sensor performance, the CNT concentration in the CNT/PVA nanocomposite was varied (0.1 g, 0.15 g, and 0.2 g). The sensing probes were tested in an in-house developed flow cell, as detailed in Chapter 2. The sensor was evaluated using mercury ion solutions with concentrations ranging from 0 to 30 ppb. Experimental results revealed the optimal composition as 0.15 g CNT in the CNT/PVA nanocomposite. The optimized sensor exhibited a linear response within the 0–30 ppb range, achieving a high sensitivity of 0.2458 nm/ppb and excellent selectivity for Hg^{2+}. It demonstrated an impressively low LOD of 0.08 ppb, significantly below the WHO threshold for drinking water. Additionally, the sensor showed high reversibility and repeatability, with a fast average response time of 0.4 s. Further, the proposed sensor was employed to detect Hg^{2+} in real water samples, and its results closely matched to those obtained using the standard ICPMS method, with RPD values of less than 4%, validating its accuracy. The sensor also underwent extensive stability and reliability testing as discussed in Chapter 2. In the short-term stability test, the maximum observed standard deviations in the resonance wavelength was ±0.01 nm, confirming the sensor's high accuracy, with a maximum resolution of ±0.04 ppb for Hg^{2+} detection. In the long-term stability and reliability test, the results exhibit a maximum variation of just 0.002% compared to the initial measurement, highlighting the exceptional repeatability and reliability of the developed optical fiber Hg^{2+} sensor.

Chapter-4

The primary objective of the research presented in this chapter is to develop a novel optical fiber sensor for detecting another highly toxic water contaminant As^{3+}, with optimal sensitivity, exceptionally low LOD, high selectivity, and rapid response time. To achieve these, the proposed sensor utilizes the LSPR technique, employing an aluminum oxide/graphene oxide (Al_2O_3/GO) nanocomposite as the sensing material. It is important to mention that Al_2O_3/GO nanocomposite is used for the first time to realize an optical fiber arsenic sensor to the best of authors' knowledge. The sensor preparation begins with coating gold nanoparticles onto the centrally decladded U-shaped core of the PCS optical fiber, which is then followed by the coating of the Al_2O_3/GO nanocomposite sensing film. Both AuNPs and GO was synthesized utilising the same method as discussed in Chapter 2. To optimize the sensor performance, the amount of Al_2O_3/GO nanocomposite dispersed in IPA was varied in the order of 1mg/ml, 1.5mg/ml, 2mg/ml. To evaluate the sensing probes with varying film compositions, they were tested in an in-house developed flow-cell as discussed in Chapter 2. The proposed sensor was tested for arsenic ion solutions with concentrations ranging from 0 to 20 ppb. Experimental analysis revealed that the optimal sensor performance was achieved with a sensing film composition of 1.5 mg/mL of Al_2O_3/GO nanocomposite in IPA. The optimized sensor exhibits a linear response within the 0–20 ppb range with a high sensitivity of 0.1833 nm/ppb along with high selectivity towards As^{3+}. The proposed sensor also exhibits an impressively low LOD of 0.09 ppb, which is significantly lower than the threshold of As^{3+} set by WHO in drinking water. Additionally, the sensor exhibits high degree of reversibility and repeatability. Furthermore, the proposed sensor demonstrates an average fast response time of 0.5 s. Next, the proposed sensor was further employed to detect As^{3+} in real water samples, and its results closely matched those obtained using the standard ICPMS method, with RPD values of less than 5%, validating its accuracy. The sensor also underwent extensive stability and reliability testing as discussed in Chapter 2. In the short-term stability test, the maximum observed standard deviations in the resonance wavelength was ±0.0127 nm, confirming the sensor's high accuracy, with a maximum resolution of ±0.058 ppb for As^{3+} detection. In the long-term stability and reliability test, the results exhibit a maximum variation of just 0.004% compared to the initial measurement, demonstrating the exceptional repeatability and reliability of the developed optical fiber As^{3+} sensor. While this sensor demonstrates high sensitivity, a very low LOD, and a fast response time, there remains scope for further improvement, particularly in

enhancing sensitivity and achieving an even lower LOD. This led to the foundation of the development of an another As^{3+} sensor discussed in the following chapter.

Chapter-5

In order to further enhance the sensing performance for detecting As^{3+} ion, another sensing probe was developed using lauryl sulphate functionalized gold nanoparticles. In this case, the gold nanoparticles serve both as the LSPR generator and the sensing material unlike the sensor discussed in Chapter 3 where a sensing material is coated over the gold nanoparticles coated probe. It is important to mention that lauryl sulphate functionalized gold nanoparticles are used for the first time to realize an optical fiber arsenic sensor to the best of authors' knowledge. Lauryl sulphate functionalized gold nanoparticles was coated over the centrally decladded U-shaped core of the optical fiber. In order to examine the effect of lauryl sulphate functionalization of the AuNPs on the sensor performance, another sensing probe was prepared by coating bare AuNPs without functionalization. The developed sensing probes were characterized in a flow cell as discussed in Chapter 2. The sensing probe with lauryl sulphate-functionalized AuNPs demonstrated an enhanced sensitivity of 0.3073 nm/ppb, approximately 18 times higher than the bare AuNPs-coated probe (0.0168 nm/ppb). The sensing probe shows linear dynamic range of 0-30 ppb with a very low LOD of 0.06 ppb. The sensor also exhibits a high selectivity towards As^{3+} ions. Next, the sensor was exposed to repeated As^{3+} concentration step changes between 5ppb and 30ppb As^{3+} concentration to investigate the repeatability and reversibility characteristics. The sensor's output shows identical change during the forward (5ppb to 30ppb) and the reverse (30ppb to 5ppb) cycle of the As^{3+} concentration changes. Additionally, the proposed sensor exhibits an average response time of 0.5s. The sensor was then tested for short-term stability using the similar method as discussed in Chapter 2 for three different As^{3+} concentrations (5ppb, 15ppb, and 30ppb). The observed maximum standard deviation in the resonance wavelength is ±0.0194 nm, confirming the sensor's high accuracy, with a maximum resolution of ±0.063 ppb for As^{3+} detection. In order to test the reliability and repeatability of the sensing probe similar method is used as discussed in Chapter 2 for three different As^{3+} concentration (5ppb, 15ppb, and 30ppb). It is observed that the maximum variation in the output of the proposed optical fiber sensor in comparison to day one, is only 0.006% across all three As^{3+} concentration. This shows the excellent repeatability of the developed optical fiber As^{3+} sensor. As can be observed, an enhanced sensitivity with a slightly

lower LOD and a larger linear dynamic range is achieved in comparison to the sensor developed in Chapter 3, the time response is remained constant.

Chapter-6

The main objective of the research presented in this chapter is to develop a simple yet innovative optical fiber sensor for detecting the explosive compound TNP with optimal sensitivity, an exceptionally low LOD, high selectivity, and rapid response time. To accomplish this, a polymer PFTPA film is synthesized onto the centrally decladded straight PCS fiber. For this sensor, intensity modulation through evanescent wave absorption technique is employed. For the development of the sensor, first, Polymer PFTPA was prepared by using chemical methods. In order to optimize its performance, a detailed examination of the sensor's characteristics was conducted by varying both the composition and thickness of the sensing film. Then the sensor characterization was performed by placing the sensor in a flow cell, as described in Chapter 2. For the experiment, the optical output from a UV laser source operating at 390.26 nm was coupled to one end of the optical fiber sensor, while the distal end was connected to a photodetector via a SMA connector. The photodetector was interfaced with a computer through a data acquisition (DAQ) card and monitored in real time using MATLAB. Aqueous TNP solutions with concentrations ranging from 0 to 50 ppb were prepared. The sensor's output intensity was measured for each TNP concentration, allowing enough time for the readings to stabilize. The experimental results indicate that the fiber sensors output intensity decreases as concentration of TNP increases. Analysis of the experimental data revealed that the 3-dip coated probe having 1.3 mg/ml concentration of polymer PFTPA in THF, exhibited optimal performance. The optimized sensor demonstrates a linear response within the 0-50 ppb range, with a high sensitivity of 0.0032/ppb (73.31×10^4 M^{-1}) and a remarkably low LOD of 1.06 ppb. The sensor also shows excellent selectivity for TNP and offers a rapid response time of just 2 s. Repeatability and reversibility characteristics of the proposed sensor were investigated by exposing the sensor successively to air, 10 ppb TNP concentration, air, 50 ppb TNP concentration and again air. This cyclic exposure between air, low concentration of TNP (10 ppb) and high concentration of TNP (50 ppb) was repeated multiple times. The results show that the fiber sensor output changes instantly and smoothly during both forward and reverse TNP concentration changes, without any hysteresis, indicating a completely reversible response of the proposed sensor. The sensor’s practicality was validated by detecting TNP in

real water samples, achieving a recovery range of 98.42% to 102.94%. Further, rigorous testing confirms the sensor's stability and reliability, with a maximum intensity fluctuation of ±0.0094 and a resolution of 0.294 ppb during short-term stability tests. For long-term stability, the sensor exhibits a maximum variation of only 0.19% compared to the first day. Although this sensor demonstrated high sensitivity with very low LOD, there is still further scope of improving the sensitivity and lowering the LOD. This laid the foundation for the research work discussed in the next chapter.

Chapter-7

The sensor described in Chapter 5 utilizes intensity modulation through the evanescent wave absorption technique to detect trace amounts of TNP. To further improve the sensing performance for detecting TNP, in this work an LSPR based optical fiber sensor is developed that employs ZnO QDs as the sensing material. It is important to mention that, for the first time in the best of author's knowledge an optical fiber TNP sensor based on LSPR technique employing ZnO QDs as the sensing materials is reported. For the development of the sensor, ZnO QDs were synthesized using a chemical reaction method. To provide aqueous stability to the prepared ZnO QDs, it is capped with (3-aminopropyl) triethoxysilane (APTES). For the development of optical fiber TNP sensor, PCS fiber was used. A similar methodology as described in Chapter 2 was used for coating AuNPs on the U-shaped centrally decladded sensing region. After that for the coating of ZnO QDs dip coating method is employed. To optimize the sensor's performance, the amount of ZnO QDs dispersed in 10 mL of distilled water was varied, using 170 mg, 200 mg, and 220 mg. The sensing probes with these varying film compositions were tested in an in-house developed flow-cell, as detailed in Chapter 2. The proposed sensor was evaluated using TNP solutions with concentrations ranging from 0 to 50 ppb. Experimental analysis demonstrated that optimal sensor performance was achieved with a sensing film composition of 200 mg of ZnO QDs. This optimized sensor displays a linear response in the range of 0–50 ppb, with an enhanced sensitivity of 0.1288 nm/ppb and a remarkably low LOD of 0.19 ppb for TNP. Additionally, the sensor demonstrated high selectivity towards TNP and exhibits an average response time of 2 s. To examine the sensor's reversibility and repeatability, it was subjected to cyclic exposure to TNP solutions ranging from 5 ppb to 50 ppb. The results confirmed consistent performance during both forward (5 ppb to 50 ppb) and reverse (50 ppb to 5 ppb) TNP concentration changes. The practicality of the sensor was further validated through successful detection of TNP in real water samples,

yielding recovery rates between 94.03% and 110.22%. The sensor was then tested for short-term stability using the similar method as discussed in Chapter 2 for three different As^{3+} concentrations (5ppb, 30ppb, and 50ppb). The maximum observed standard deviations in the resonance wavelength were ±0.0249 nm with a maximum resolution of ±0.193 ppb, confirming the sensor's high accuracy. In terms of long-term stability and reliability, the optimized optical fiber TNP sensor was tested over 18 days, with measurements taken at 5-day intervals for three distinct TNP concentrations (5 ppb, 30 ppb, and 50 ppb). The results showed a maximum variation of only 0.005% compared to the initial measurements, highlighting the exceptional repeatability and reliability of the developed optical fiber TNP sensor.

Chapter-8

This chapter provides a summary and highlights of the optical fiber sensors developed for detecting Hg^{2+}, As^{3+}, and TNP using localized surface plasmon resonance and intensity modulation through evanescent wave techniques. Additionally, the chapter outlines the future scope for research in this field.

Chapter 2 : Novel LSPR based U-shaped optical fiber mercury ion sensor employing Graphene oxide and Chitosan composite

2.1 Introduction

Environmental contamination caused by toxic heavy metal ions is a significant global concern, owing to their detrimental impact on both the environment and human health [29][81]. Heavy metal ions, particularly those present in industrial wastewater, account for a significant portion of environmental pollution [82]. Among these heavy metal ions, mercury ions (Hg^{2+}) are considered the most toxic and hazardous element. They have the potential to accumulate easily in the environment and enter the human body through the skin, respiratory system, and gastrointestinal tract [28]. Excess levels of Hg^{2+} in water can cause various disorders and diseases, such as Hunter-Russell syndrome, Minamata disease, and severe kidney damage. According to the World Health Organization (WHO) and US Environmental Protection Agency (USEPA) guidelines, the minimum concentration of mercury ions in drinking water needs to be below 6 ppb and 2 ppb respectively in drinking water. Therefore, it is crucial to monitor trace levels of Hg^{2+} in pollutant samples to ensure the safety of both human health and the environment. Multiple conventional analytical techniques have been developed to detect mercury ions, including atomic absorption and emission spectrometry [30], atomic fluorescence spectrometry [83], inductively coupled plasma mass spectrometry (ICP-MS) [32], high-performance liquid chromatography (HPLC) [34], colorimetric [36], [84], [85] and electrochemical [38]. Although these techniques offer high sensitivity and accuracy in detecting mercury ions, they also come with several drawbacks such as they involve complex mechanisms, bulky instrumentations and are time consuming and expensive.

Surface plasmon resonance (SPR) and localized surface plasmon resonance (LSPR) offer a promising alternative for detecting heavy metal ions. Given their simplicity, rapid response, cost-effectiveness, and high sensitivity, SPR and LSPR overcome the limitations of conventional methods. Both LSPR and SPR are highly responsive to changes in localized refractive index, thereby showing a corresponding shift in the resonance wavelength. Hence, researchers have developed several LSPR and SPR-based sensors for detecting Hg^{2+} ions. For example, as discussed in Chapter 1 from references [39 – 43]. Although these sensors demonstrate promising LOD, most have LODs that exceed the regulatory thresholds for Hg^{2+} in drinking water set by the WHO and USEPA. Therefore, improving the LOD is crucial for

effectively detecting Hg^{2+} in drinking water applications. To achieve this, optical fiber-based SPR and LSPR sensors can be utilized, as they offer several advantages over non-optical-fiber sensors. These advantages include high sensitivity, remote sensing capabilities, rapid response, multiplexing, real-time detection, cost-effectiveness, miniaturization, and durability, making them ideal for real-field applications. Only a few SPR and LSPR-based optical fiber Hg^{2+} sensors have been reported so far. For example, as discussed in Chapter 1 from references [64–70]. Among these reported sensors many offers LOD which exceed the WHO and USEPA threshold for Hg^{2+} ions in drinking water. This limits their suitability for detecting Hg^{2+} in drinking water applications. On the other hand, sensors reported with LODs within the acceptable regulatory limits, either lack selectivity or exhibit slow response time. Furthermore, only a few sensors demonstrate reusability. Therefore, there is a significant need to develop an optical fiber sensor that achieves a very low detection limit, optimal sensitivity, high selectivity, rapid response, and reusability for being suitable towards real-field applications.

The main objective of the research work presented here is to develop an optical fiber sensor for detecting Hg^{2+} with optimal sensitivity, a remarkably low LOD, high selectivity, rapid response time and reusability. To achieve this, the proposed sensor employs the LSPR technique using graphene oxide functionalized with chitosan composite (GO-CS) as the sensing material. A thin film of GO-CS composite is coated onto the AuNPs coated centrally decladded U-shaped core of the plastic-clad-silica (PCS) optical fiber. The reason for using GO-CS as the sensing material for detecting Hg^{2+} is based on the exceptional adsorption capability of graphene oxide for heavy metal ions, primarily due to its high surface area to volume ratio. GO is a two-dimensional nanomaterial that has received significant attention due to its unique properties and cost-effective production. The monolayer of GO comprises sp^2 and sp^3 hybridized carbon atoms, alongside oxygen-rich electronegative functional groups like hydroxyl, epoxide, carbonyl, and carboxyl groups, which exhibit a strong affinity towards heavy metal ions [86]. On the other hand, chitosan, with one amino group and two hydroxyl groups per glucosamine monomer, serves as adsorption sites, particularly the amino groups, which strongly interact with Hg^{2+}. Further, chitosan offers additional advantages such as non-toxicity, excellent film-forming ability, powerful adhesion property, and high mechanical strength, making it ideal for sensor applications [87]. Therefore, combining CS with GO will increase the number of adsorption sites for Hg^{2+} ions. Consequently, GO functionalized with chitosan composite is anticipated to exhibit high sensitivity and selectivity towards Hg^{2+} ions.

It is worth mentioning that GO-CS composite is used for the first time to realize an optical fiber based Hg^{2+} sensor to the best of authors' knowledge. Experimental investigation highlights that incorporating GO-CS composite onto the AuNPs-coated LSPR sensing probe enables precise detection of Hg^{2+} ions, even at ultra-low concentrations in the sub-parts per billion range. The sensor demonstrates outstanding sensitivity of 0.0728 nm/ppb Hg^{2+} concentration and an exceptionally low limit of detection of 0.29 ppb Hg^{2+}. Additionally, it exhibits a rapid response time of 0.6 s. Furthermore, the sensor demonstrates high degree of repeatability, stability, reversibility, and reliability. The obtained results highlight the proposed sensor's potential as a highly sensitive, selective, rapid, and cost-effective mercury ion sensor for real-field applications. Moreover, the proposed sensor is utilized to detect mercury ion in real water samples and the results are validated from the standard inductively coupled plasma mass spectrometry (ICPMS) method.

2.2 Experiment

2.2.1 Synthesis of gold nanoparticles

Gold nanoparticles (AuNPs) were synthesized by the reduction of Tetrachloroauric acid ($AuHCl_4$) using Trisodium citrate ($Na_3C_6H_5O_7$) [88]. Subsequently, $AuHCl_4$ (1 mM, 150 ml) was introduced into a flask and heated until boiling. Then, $Na_3C_6H_5O_7$ (38.8 mM) was added to the boiling solution, and heating was continued for approximately 10 minutes. The reduction of Au ions to Au metal nanoparticles was facilitated by trisodium citrate in the solution. The emergence of a wine-red color within the solution indicates the formation of gold nanoparticles.

2.2.2 Characterization of gold nanoparticles

The size of the synthesized AuNPs was analyzed using a Field Emission Transmission Electron Microscope (FETEM, JEOL-2100F). Fig. 2.1(a) depicts the typical FETEM image of the prepared AuNPs, whereas, the size distribution is illustrated in Fig. 2.1(b). As can be observed from Fig. 2.1(b), diameter of the developed AuNPs is found to be predominantly in the range of 10 to 24 nm, with an average particle size of 16 ± 0.06 nm. Additionally, the synthesized AuNPs were characterized for their absorption properties using a UV-Vis spectrometer, as illustrated in Fig. 2.1(c). The results indicate that the AuNPs exhibit a characteristic localized surface plasmon peak at 526 nm, confirming the successful synthesis of gold nanoparticles

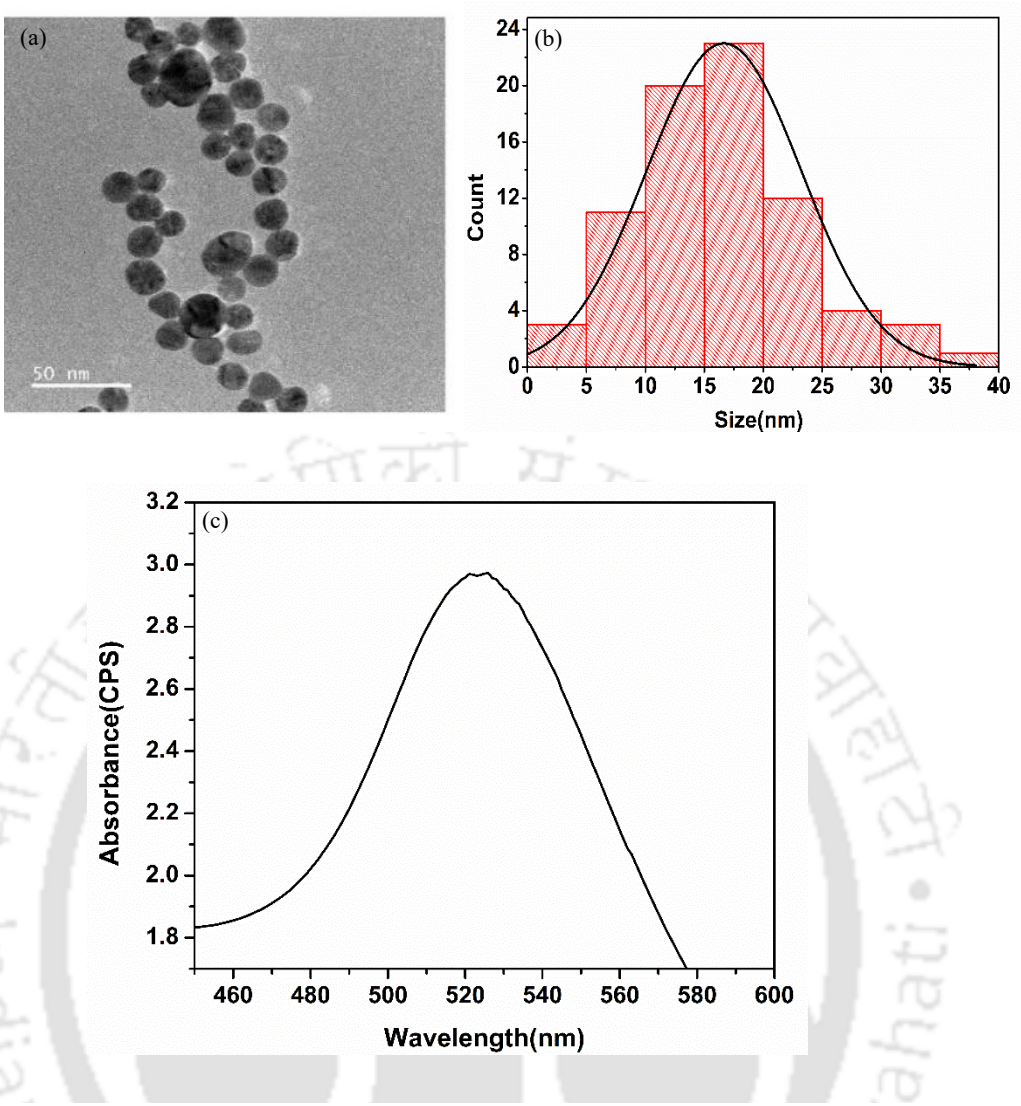

Figure 2.1: (a) FETEM image of AuNPs, (b) Size of the AuNPs, (c) UV-Vis spectrum of AuNPs.

2.2.3 Synthesis of Graphene oxide and Chitosan composite

Graphite is used to synthesize GO using the Modified Hammers method [89]. 0.5 g of graphite and 0.5 g of $NaNO_3$ were added in 23 ml of H_2SO_4 which is stirred in an ice bath for 15 minutes. Then, 3 g of oxidizing agent $KMNO_4$ is gradually added to the mixture and stirred for another 15 minutes. The resulting mixture is transferred to a deionized water bath with a temperature of 35^0C and stirred for approximately one hour. After that, 40 ml of H_2O is added to the solution and stirred for 30 minutes at 90^0C. Then, a 100 ml of H_2O and 3 ml of H_2O_2 are slowly added, causing the solution to change color from dark brown to yellow. The resulting solution is filtered and washed with 100ml of deionized water until all visible particles are removed from the precipitate, and then centrifuged. Finally, the sediment is redispersed in water using mild sonication in a table top ultrasonic cleaner to obtain a solution of exfoliated graphene oxide.

To prepare graphene oxide and chitosan (GO-CS) composite, a chitosan solution was first prepared by dissolving the appropriate amount of chitosan powder in a 2% acetic acid solution and stirring for 4-5 hours to achieve a smooth solution. Meanwhile, suitable amount of graphene oxide was dispersed in 20 mL of deionized water using an ultrasonication bath for 2 hours to form a stable suspension. This GO suspension was then slowly added to the chitosan solution under continuous stirring. The resulting mixture was stirred for an additional hour to achieve a homogeneous solution of GO-CS composite.

2.2.4 Characterization of Graphene oxide, Chitosan and Graphene oxide and Chitosan composite

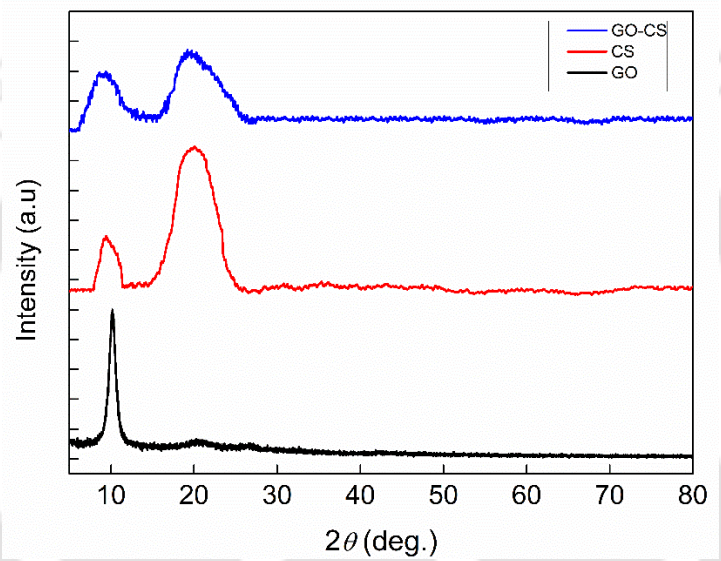

Figure 2.2: XRD of GO, CS and GO-CS composite.

For the structural characterization of the prepared GO, CS, and GO-CS composite, X-ray diffraction (XRD) patterns were recorded over a 2θ angle range of 5° to 80°. For that, an X-ray diffractometer (XRD, Rigaku TTRAX III) in Bragg Brentano geometry, operating at 5kW with Cu-Kαradiation (λ = 1.5406 Å) was used. Fig. 2.2 shows the XRD spectra for GO, CS, and the GO-CS composite. In the case of GO, a strong peak appears at 2θ = 10.2°, corresponding to the (001) crystal plane with an interlayer spacing of 8.67 Å. This confirms that the graphite powder was well-oxidized using concentrated acids and $KMnO_4$ to obtain GO. Pure chitosan powder exhibits two characteristic peaks at 9.44° and 20.1°, corresponding to the (020) and (110) crystal planes, respectively. For the GO-CS composite, two peaks appear at approximately $2\theta \sim 9.44°$ and 19.22°. The characteristic peak of GO overlaps with the

diffraction peak of CS, resulting in a broad peak at 9.44°. This overlap confirms the exfoliation of chitosan on the GO surface, indicating the successful formation of the GO-CS [90].

2.2.5 Preparation and Characterization of the sensing probe

To develop the sensing probe, a 40 cm long plastic-cladding-silica (PCS) multimode fiber with a core diameter of 600 µm was utilized. The fiber ends were carefully prepared to ensure optically-flat end faces perpendicular to the fiber axis. This is crucial for maximizing light coupling efficiency from source to the fiber and fiber to the detector. Next, 2.5 cm of cladding was removed from the central section of the fiber. The decladded portion was then throughly

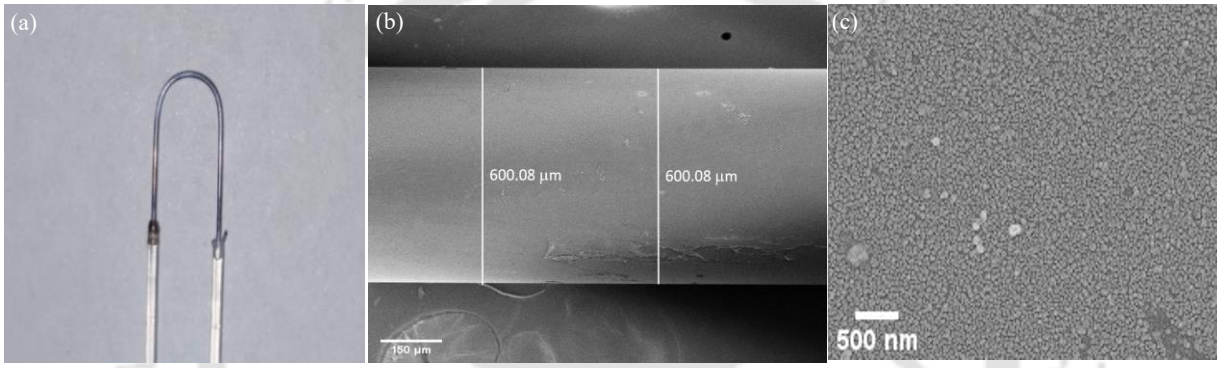

Figure 2.3: (a) AuNPs coated U-shaped probe, (b) FESEM image of the centrally decladded region of thr fiber carrying AuNPs coating, (c) FESEM picture of surface morphology of the AuNPs coated region.

cleaned with a soap solution, de-ionized water, and acetone. After cleaning, the decladded section of the fiber was then carefully bent into a U-shape by exposing it to a propane flame. Experiments were conducted only on probes having perfect U-shape and with a uniform core diameter in the U-shaped region. U-shaped probes having a bending radius of 2.5 mm are employed in this research. To prepare the sensing probe for attachment of gold nanoparticles, the U-shaped region was first soaked in chromic acid for 12 hours. Subsequently, it was sonicated in de-ionized water and dried in the oven. The U-shaped region was then immersed in a 5% (v/v) ethanol solution of 3-amino-propyltrimethoxysilane (APTMS) for 3 hours to obtain an amine-functionalized glass surface. Following this, the probe was rinsed with ethanol and dried in the oven. Next, the probe was dipped in the prepared gold nanoparticle solution for 2 hours. This results in the formation of gold nanoparticle film on the decladded fiber surface. Finally, the probe was rinsed with de-ionized water and dried in the oven for 30 minutes. The AuNPs coated U-shaped optical fiber probe is depicted in Fig. 2.3(a). The thickness of the gold nanoparticle coated probe and the surface morphology of the coated

region were analyzed using a Field Emission Scanning Electron Microscope (FESEM) (Zeiss, Sigma 300). Fig. 2.3(b) depicts the image of a section of AuNPs coated U-shaped optical fiber. An average diameter in this section is observed to be ~600.08 µm, which establishes an average thickness of the AuNPs film as ~40 nm. Fig. 2.3(c) shows the surface morphology of the deposited AuNPs film. The image illustrates not only a high density but also uniform coating of the AuNPs on the decladded fiber surface. In the next step, the AuNPs coated probe underwent further coating with GO-CS composite. In order to investigate the impact of sensing film composition on to the sensor performance, initially chitosan was fixed at 0.5g in the solution. The amount of GO dispersed in this chitosan solution was varied from 0.1g, 0.2g and 0.3g.

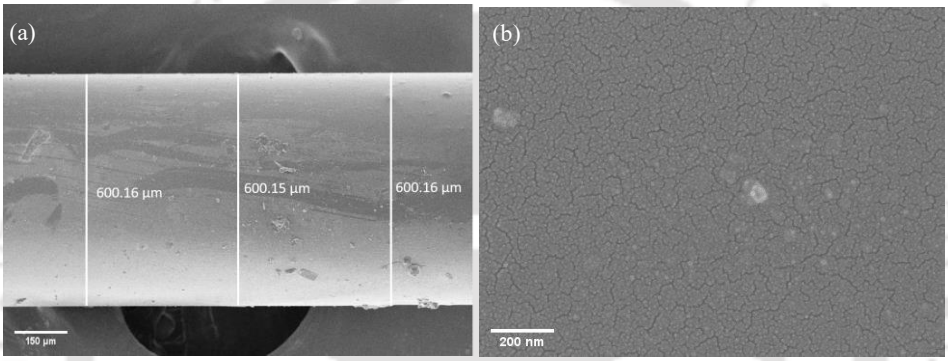

Figure 2.4: (a) FESEM image of the centrally decladded region of the fiber coated with GO-CS over the AuNPs coating film. (b) FESEM pattern of surface morphology of the GO-CS coating region.

After determining the optimal GO concentration, the chitosan concentration was varied from 0.4g to 0.6g while keeping the GO concentration fixed at the determined optimal value. Dip-coating method was employed afterwards, where AuNPs deposited U-shaped region of different probes were slowly dipped into the different solutions separately. Thereafter, these dip coated probes were left to dry for two days at room temperature. The surface morphology, nanostructure, and deposited film thickness were analyzed using a FESEM. For instance, Fig. 2.4(a) depicts an image of a section of the GO-CS composite (0.2g of GO in 0.5g of CS) coated sensing region of the U-shaped optical fiber that already carried a coating of AuNPs onto the decladded core. An average diameter of ~600.156 µm was observed for this region. As the AuNPs coating thickness is already determined to be ~40 nm, an average thickness of the GO-CS composite sensing film is observed to be ~38.33 nm. Likewise, the thickness of the sensing film for other film compositions was determined to be ~27.5 nm for a mixture of 0.1 g GO with 0.5 g of chitosan, ~63.33 nm for 0.3 g of GO with 0.5 g of chitosan, ~20 nm for 0.2 g of GO

with 0.4 g of chitosan, and ~70 nm for 0.2 g of GO with 0.6 g of chitosan. Fig. 2.4(b) illustrates the surface morphology of the deposited GO-CS composite sensing film, showcasing an interconnected, high-quality coated surface with moderate roughness.

In order to conduct the experiment and investigate the sensor's response, the sensor was fixed inside an in-house developed flow-cell (dimension 5 cm × 5 cm × 4 cm), with the sensing region positioned in the middle of the chamber, as depicted in Fig. 2.5. Light from a Broad Band Source (Ocean Optics, HL-2000-FSHA) is coupled to the optical fiber senor from one arm. The other arm is connected to a spectrometer (Ocean Optics, RH4000) using a subminiature version A (SMA) connector. The spectrometer is interfaced with a computer through MATLAB program for real-time monitoring of the sensor. During the experiment, the flow-cell was filled with the solution containing the lowest concentration of Hg^{2+}, and the transmittance through the optical fiber sensor was recorded. The Hg^{2+} solution was then drained, and both the flow-cell and sensor were thoroughly cleaned with deionized water to ensure no residual Hg^{2+} remained. The flow-cell was subsequently filled with a solution of higher Hg^{2+} concentration. This process was repeated, with Hg^{2+} concentrations varying between 0 ppb and 200 ppb. The fiber output (transmittance) was recorded for each concentration. For each experiment, the sensor was allowed to remain in the solution long enough to achieve a stable response.

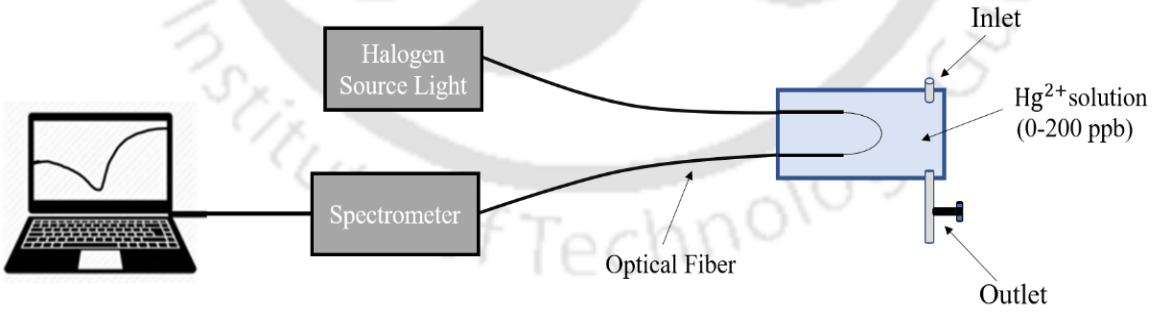

Figure 2.5: Schematic diagram of the experimental setup.

2.3 Result and Discussion

2.3.1 Response of the AuNPs coated LSPR sensor to surrounding refractive index variation

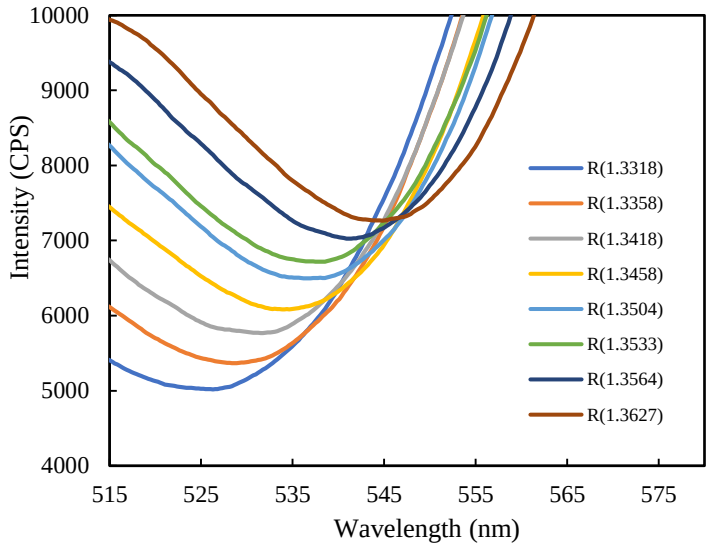

Figure 2.6: Variation of transmittance of the optical fiber LSPR sensor with refractive index change.

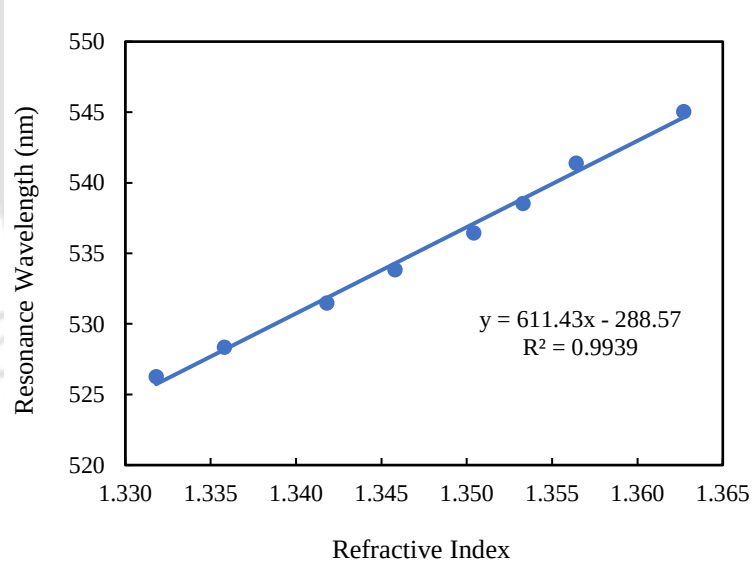

Figure 2.7: Refractive index sensitivity of the AuNPs coated optical fiber LSPR sensor.

Before applying the GO-CS composite sensing film and to test it for Hg^{2+} detection, sensitivity of the AuNP coated LSPR based optical fiber U-shaped probe towards the ambient refractive index (r.i.) variations was examined first. To do this, AuNP coated LSPR probe, fixed into the flow-cell, was exposed to the test solutions of varying refractive indices (in a range of 1.3318 to 1.3627) sequentially. These solutions were prepared by mixing methanol, ethanol, and

toluene in different ratios. The refractive indices of these solutions were measured using a refractometer (Hanna Instruments, HI96800). Change in the transmitted spectrum was observed immediately after exposing the sensor to the test solution, and the spectrum got quickly stabilized for each test solution. The resulting LSPR spectra are depicted in Fig. 2.6. As can be observed, transmittance at the resonance wavelength increases as the refractive index increases. In addition, a noticeable red shift for the dip resonance wavelength is observed with increasing refractive indices. This establishes that the gold nanoparticle-coated LSPR probe is sensitive to the surrounding refractive index variations. In order to get a better understanding of the response characteristics, the dip resonance wavelength is plotted against the varying refractive indices in Fig. 2.7. The refractive index sensitivity, measured in nm/RIU (where RIU = refractive index unit), is defined as the shift in dip resonance wavelength relative to the corresponding change in refractive index. As can be observed from Fig. 2.7, the LSPR optical fiber sensor demonstrates a linear response with a high refractive index sensitivity of 611.43 nm/RIU. This high sensitivity highlights the potential of this optical fiber sensor to effectively detect even subtle changes in the surrounding refractive index.

2.3.2 Response of the proposed LSPR based optical fiber sensor towards Hg^{2+} ions detection

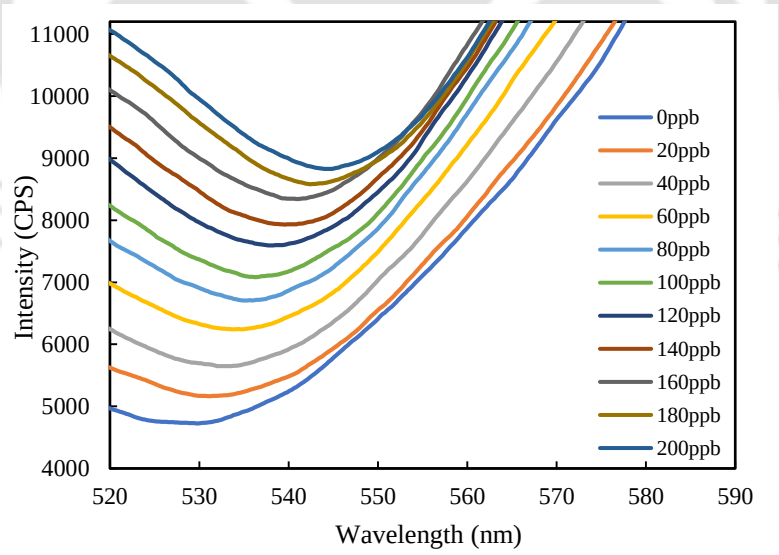

Figure 2.8: LSPR spectrum with varying mercury ion concentrations.

The proposed sensor exploits the localized surface plasmon resonance technique to detect Hg2+ ions, employing GO-CS composite as the sensing material coated onto the AuNPs coated core of a U-shaped optical fiber. To optimize the sensor response, the impact of sensing film

configuration onto the sensor performance was studied. Initially, keeping chitosan fixed at 0.5g in the solution the amount of GO was varied from 0.1 g, then to 0.2 g, and finally to 0.3 g. After determining the optimal GO concentration, the chitosan concentration was varied from a lower concentration of 0.4g to a higher concentration of 0.6g in a solution that carried optimal GO concentration. To evaluate the performance characteristics of the proposed sensor, separate solutions of mercury ions were prepared, where mercury ion concentration was varied in the range of 0-200 ppb. Proposed sensor was then exposed, at a time, to the mercury ion solution of fixed concentration, and the optical fiber sensors output was recorded. Fig. 2.8 shows the resulting LSPR spectra, as an example, for the sensing probe with film composition corresponding to 0.2 g of GO in 0.5 g of chitosan solution. The results indicate that there is a correlation between the concentration of mercury ion and the resonance wavelength. Higher concentrations of mercury ions lead to a noticeable red shift in the resonance wavelength. This shift in the LSPR resonance wavelength can be attributed to the changes in the refractive index of the surrounding medium around the AuNPs when the sensor is exposed to the Hg^{2+} ions solutions. The change in refractive index occurs as a result of the adsorption of the electropositive Hg^{2+} ions on the highly electronegative hydroxyl, carboxyl and amino sites found on the surface of GO-CS composite. This adsorption consequently induces change in the refractive index of the environment, surrounding to the gold nanoparticles (AuNPs). This, in turn, causes a red shift in the resonance wavelength of the LSPR, as observed. In order to get a deeper insight, the sensor response corresponding to each film composition was analysed by plotting the dip resonance wavelength against varying concentrations of Hg^{2+} ions. Fig. 2.9 depicts the response of the sensor carrying GO-CS composite sensing film of fixed chitosan concentration of 0.5g and varying GO concentrations. GO concentration is varied as 0.1g, 0.2g and 0.3g. As depicted in the figure, all the sensors with varied GO in the film compositions exhibit a linear response within the range of 0-200 ppb Hg^{2+} concentration. Specifically, the sensor with a film composition of 0.1g of GO demonstrates a sensitivity of 0.0558nm/ppb. With an increase in GO concentration from 0.1g to 0.2g, the sensitivity rises to 0.0728nm/ppb. This higher sensitivity can be attributed to the increased number of electronegative sites available for mercury ion adsorption, a consequence of higher GO concentration. This, in turn, led to more pronounced changes in the refractive index in the vicinity of gold nanoparticles, and hence, a larger shift in the LSPR resonance wavelength. However, as the GO concentration is further increased from 0.2g to 0.3g, the sensitivity decreases to 0.0668nm/ppb. This reduction in sensitivity is mainly due to the increasing thickness of the sensing film on the U-

shaped LSPR probe as the GO concentration increases. With 0.3g of GO, the film thickness exceeds the decay length (20-40 nm) of the LSPR [91]. The thicker film limits Hg^{2+} ions from penetrating deeper into the sensing film, that is close to the gold nanoparticles. Although more adsorption sites are present, interactions beyond the decay length do not affect the resonance wavelength shift. This was the reason for the reduced sensitivity observed in this case. This investigation establishes an optimal GO concentration of 0.2g for the sensing film composition.

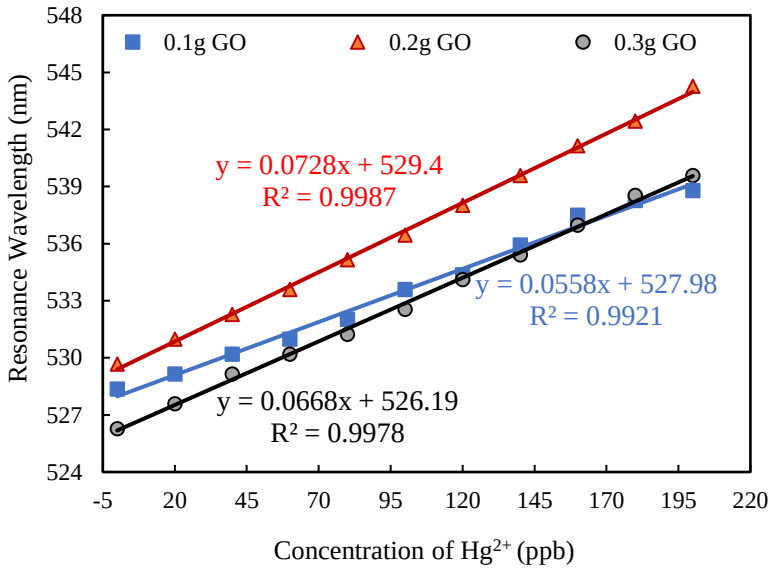

Figure 2.9: Experimentally observed sensor response of the optical fiber sensor having different film compositions (0.1g, 0.2g and 0.3g of GO in 0.5g of Chitosan).

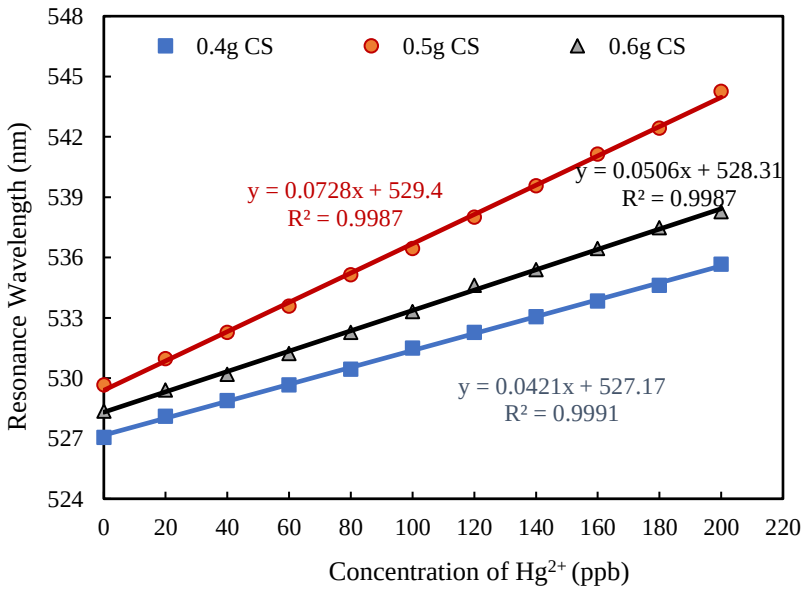

Figure 2.10: Experimentally observed sensor response of the optical fiber sensor having different film compositions (0.4g, 0.5g and 0.6g of Chitosan in 0.2g of GO).

Next, fixing the GO concentration at the optimum value of 0.2g, the film composition was further varied by changing the chitosan concentration in the solution from 0.4g to 0.5g and then to 0.6g. The corresponding sensor responses are plotted in Fig. 2.10. As can be observed from the figure, all the sensors with varied CS concentration in the film compositions exhibit a linear response within the range of 0-200 ppb Hg^{2+} concentration. The sensor with a film composition of 0.4g of chitosan demonstrates a sensitivity of 0.0421 nm/ppb. Increasing the chitosan concentration to 0.5g improves the sensitivity to 0.0728 nm/ppb which is ~1.72 times higher compared to the sensitivity observed for the 0.4g CS film composition. This sensitivity enhancement can again be attributed to the increased number of adsorption sites for mercury ions due to the increasing concentration of chitosan. Conversely, further increasing the chitosan concentration to 0.6g reduces the sensitivity to 0.0506 nm/ppb, which is ~1.43 times lower than the sensitivity observed for the 0.5g CS film composition. As with the variation in GO concentration, increasing the CS concentration also leads to a thicker sensing film. When the CS concentration reaches 0.6g, the film thickness exceeds the LSPR decay length, reducing the effectiveness of the additional adsorption sites. This results in a decrease in sensitivity. These findings indicate that the optimal film composition for the sensor is achieved with 0.2g of GO in 0.5g of chitosan.

2.3.3 Limit of detection of the sensor

In addition to sensitivity, the limit of detection (LOD) is another crucial parameter for evaluating a sensor's performance. LOD represents the sensor's ability to detect the lowest concentration of an analyte. Therefore, for the optimized sensor, LOD was calculated using the formula: LOD = $3\sigma/S$, where 'σ' is the standard deviation from multiple blank measurements, and 'S' is the sensor's sensitivity of the proposed sensor. The LOD of the optimized sensor is determined to be 0.29 ppb. The achieved LOD is approximately 20.7 times lower than the permissible limit for mercury ions in drinking water established by the WHO and 6.9 times lower than the USEPA standard. This demonstrates that the LSPR sensor is capable of accurately detecting mercury ions at concentrations well below the regulatory thresholds, highlighting its potential for ensuring the safety of drinking water.

2.3.4 Reusability, Reversibility and Response time of the sensor

Reusability/repeatability and reversibility are other critical parameters for evaluating the performance of a given sensor. To determine these characteristics, the sensor was tested by

exposing it to the minimum (10 ppb) and maximum (200 ppb) Hg^{2+} ion concentrations. First, the sensor was exposed to a 10ppb Hg^{2+} solution within the flow cell, and the corresponding LSPR spectrum was recorded. After keeping the sample for 1 minute in the flow cell, the LSPR spectrum was recorded again. After removing the 10ppb solution from the flow cell, the sensor was thoroughly cleaned with deionized water to ensure no residual Hg^{2+} ions remained onto the sensor. Sensor was then exposed to a 200ppb Hg^{2+} solution, and the LSPR spectrum was recorded at 1-minute interval. To complete one cycle, the 10ppb Hg^{2+} solution was reintroduced into the flow cell after the removal of 200ppb solution and cleaning of the sensor. Corresponding LSPR spectrum was recorded again at 1-minute interval and compared with the initial measurement. This whole cycle was repeated multiple times. Typical cyclic response is shown in Fig. 2.11(a). As can be observed, resonance wavelength remained consistent across all the cycles at the lower Hg^{2+} concentration, indicating no residual Hg^{2+} ions were left onto the sensor after the removal of solution with higher concentrations. Results illustrated in Fig. 2.11(a) also confirm consistent response of the proposed sensor during both the forward (10 ppb to 200 ppb) and reverse (200 ppb to 10 ppb) changes in Hg^{2+} ion concentration. This demonstrates the highly repeatable and completely reversible nature of the proposed sensor.

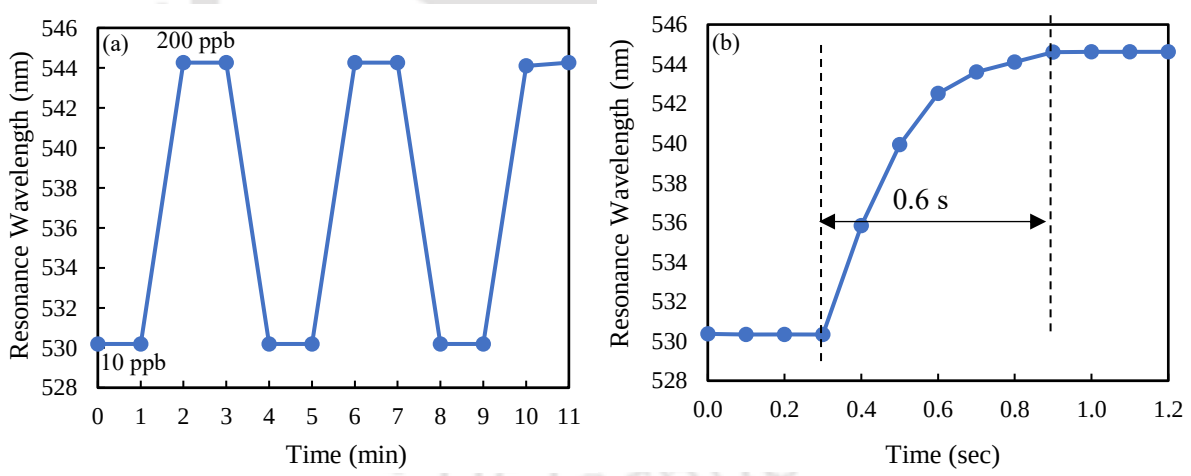

Figure 2.11: (a) Repeatability and reversibility characteristics of the proposed sensor, (b) response time (during the variation from air to 200 ppb Hg^{2+}).

The speed of detection is another very critical parameter for evaluating the performance characteristics of a given sensor. Achieving a rapid response time holds significant importance for a sensor. To evaluate the response time of the proposed sensor, the resonance wavelength of the LSPR sensor was measured before and after introducing Hg^{2+} ion solution of 200ppb concentration into the flow cell. LSPR spectra were recorded after every 0.1 sec, and the

corresponding resonance wavelength values were determined. The findings from these measurements are illustrated in Fig. 2.11(b), where the resonance wavelength values are plotted against time. As observed, the resonance wavelength is constant before the introduction of the Hg^{2+} solution into the flow cell (sensor being exposed to air). Upon introducing Hg^{2+} ion solution into the flow cell, the resonance wavelength initially exhibits a red shift, and then gradually stabilizes after approximately 0.6 seconds. This establishes a rapid response time of 0.6 seconds for the proposed sensor.

2.3.5 Selectivity of the sensor

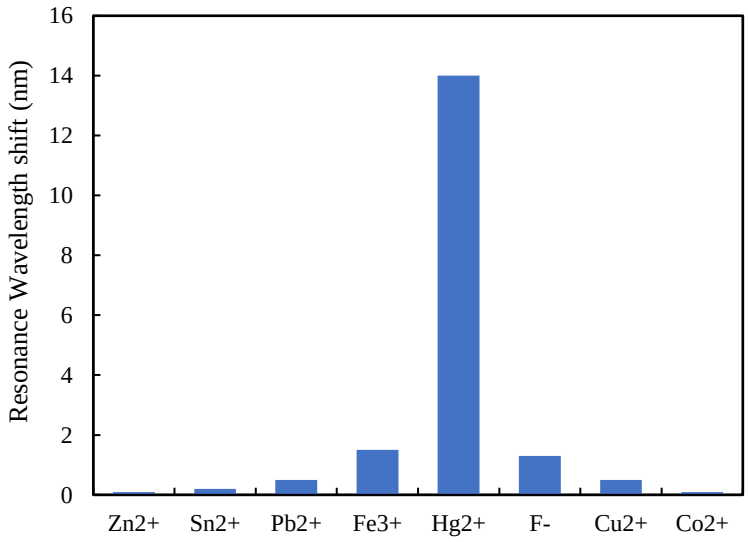

Figure 2.12: Comparison of the resonance wavelength shift of the sensor with different heavy metal ions.

Additionally, selectivity is another very crucial parameter for evaluating the sensor performance characteristics. Hence, the selectivity of the proposed sensor is evaluated. For this, experiments were conducted using a range of heavy metal ions, commonly found in groundwater, such as, Zn^{2+}, Sn^{2+}, Pb^{2+}, Fe^{3+}, F^{-}, Cu^{2+}, and Co^{2+}. These heavy metal ions can potentially interfere in the detection of Hg^{2+}. For the experiment, the concentration of each ion in the solution was kept constant at 2 ppm, except for Hg^{2+} ions which was tested at 10 times lower concentration of 200 ppb. The sensor was submerged in each heavy metal ion solution, and the resulting LSPR spectrum was observed using the same experimental setup, used for detecting mercury ions. The shift in the resonance wavelength was determined for each heavy metal ions while varying their concentration from 0 to 2 ppm, except for Hg^{2+} ions, where the shift in the resonance wavelength was determined while varying the concentration from 0 to

200 ppb. Fig. 2.12 depicts the experimentally observed wavelength shifts for each ion. As can be observed from Fig. 2.12, proposed sensor exhibits significantly higher shift in the resonance wavelength for mercury ions in comparison to any other ions, even the concentration of Hg^{2+} was as low as 200 ppb. This high selectivity of the proposed sensor towards Hg^{2+} ions can be attributed to the surface modification of GO with chitosan while the formation of GO-CS composite, which increases the number of adsorption sites for Hg^{2+} ions. Chitosan has a known selective sensitivity towards Hg^{2+} ions, as established in prior studies [69, 92]. This results in a more pronounced shift in the resonance wavelength specifically for mercury ions. Therefore, this study confirms the proposed optical fiber sensor's high selectivity towards mercury ions, indicating its potential application in mercury ion detection in real-field.

2.3.6 Comparative Analysis of the response characteristics.

Table 1: Comparison of the proposed sensor with some published reports for Hg^{2+} ion detection by SPR and LSPR sensors.

Sensing material	Method of Detection	Limit of Detection	Response Time	References
DNA element	SPR (prism based)	5 ppb	---	[39]
chitosan/maghemite	SPR (prism based)	10 ppb	---	[40]
1,6-hexanedithiol	SPR (prism based)	80 ppb	6 h	[42]
AuNPs	LSPR (liquid-phase based)	172 ppb	---	[41]
Ag-Au nanocages	LSPR (liquid-phase based)	5 ppb	80 min	[43]
Marcaptopyridine functionalized gold nanoparticles	SPR (optical fiber based)	1.6 ppb	30 min	[64]
Copper-silver core shell nanoparticles	SPR (optical fiber based)	2 ppb	---	[65]
Thymine modified gold nanoparticles	SPR (optical fiber based)	1.99 ppb	---	[66]
AuNPs PVA hybrid	SPR (optical fiber based)	200 ppb	---	[67]
chitosan /poly acrylic acid	LSPR (optical fiber based)	104.3 ppb	---	[68]
Chitosan mediated silver nanoparticles	LSPR (optical fiber based)	1.5 ppb	11 min	[69]
Glucose capped silver nanoparticles	LSPR (optical fiber based)	2 ppb	---	[70]
Graphene oxide and Chitosan composite	LSPR (optical fiber based)	0.29 ppb	0.6 sec	Present Work

The response characteristics of the proposed sensor was compared with that of the other reported Hg^{2+} sensors employing SPR and LSPR scheme. Table 1 presents limit of detection as well as response time of various other sensors for comparative analysis. As can be observed from the table, the proposed optical fiber Hg^{2+} ion sensor significantly outperforms all the reported sensors by demonstrating outstandingly low LOD of 0.29 ppb. Among all the reported works, [69] showcases the lowest LOD. The achieved LOD of the proposed sensor is ~5.2 times lower than the LOD reported in [69]. Additionally, the proposed sensor exhibits the fastest response time of 0.6 seconds (lowest amongst all the sensors), which is 1100 times faster than the fastest response time reported in [69].

2.3.7 Stability and reliability of the sensor

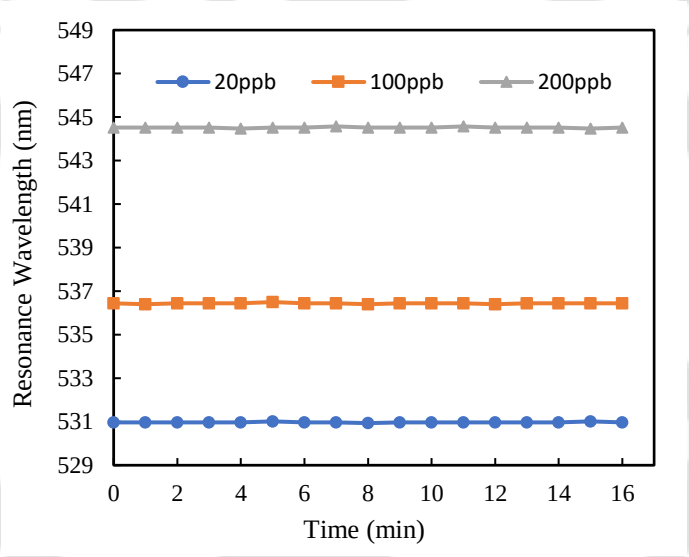

Figure 2.13: Short term stability test: continuous resonance wavelength for 16 minutes at 20ppb, 100ppb and 200ppb Hg^{2+} concentration.

The stability and reliability are other critical parameters in the detection of Hg^{2+} ions. Thus, a thorough examination was conducted to determine the short-term and long-term performance of the proposed sensor. For evaluating the short-term stability of the sensor, the LSPR spectrum was continuously recorded at 1-minute interval over 16 minutes while subjecting the sensor separately to three distinct Hg^{2+} ion concentrations (20 ppb, 100 ppb, 200 ppb). The obtained results are illustrated in Fig. 2.13. Standard deviations of the resonance wavelength were observed to be ± 0.016 nm, ± 0.023 nm, and ± 0.024 nm at 20 ppb, 100 ppb, and 200 ppb Hg^{2+} ion concentrations, respectively. Accordingly, maximum resolution of the proposed sensor is observed to be ± 0.32 ppb for Hg^{2+} ion detection, highlighting its exceptional stability and

accuracy in Hg^{2+} detection. For the long-term stability/reliability test, the developed optical fiber Hg^{2+} sensor underwent testing on four different days with a 5-day interval. These tests were conducted at three different Hg^{2+} concentrations (20 ppb, 100 ppb, and 200 ppb) over an 18-day span. The observed results over the course of 18 days are presented in Fig. 2.14. Notably, it can be observed from the figure that the maximum variation in the resonance wavelength of the developed Hg^{2+} optical fiber sensor, compared to day one at all the three concentrations, is observed to be less than 0.005%. This outcome highlights the excellent repeatability and reliability of the developed optical fiber Hg^{2+} sensor.

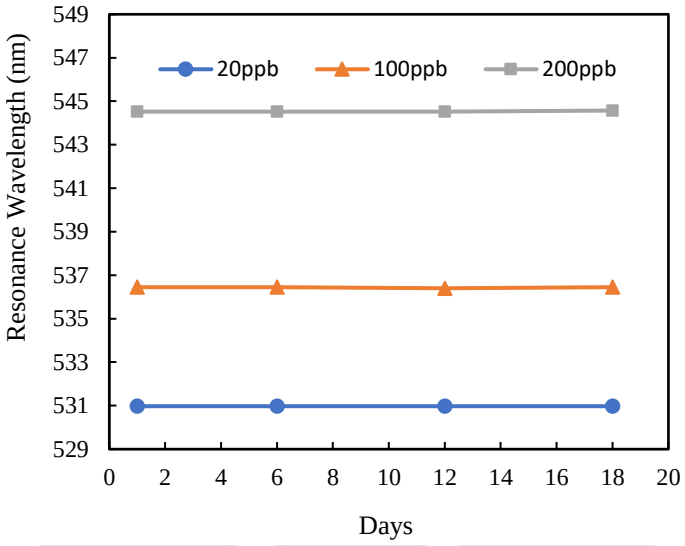

Figure 2.14: Repeatability and reliability test: resonance wavelength on four different days at 20ppb, 100ppb and 200ppb Hg^{2+} concentration.

2.3.8 Detection of Mercury ions in real water sample and validation of the sensor

To validate the commercial application potential of the proposed sensor, experiments were conducted using real drinking water samples. Samples were collected from various sources in Guwahati, Assam, India. These sources included drinking water from Indian Institute of Technology Guwahati, tap water from nearby locality, water from a site near a mill in Guwahati city, and samples from the Brahmaputra river. To verify the Hg^{2+} ion detection accuracy of the proposed sensor a comparison was made between the data obtained by employing proposed optical fiber sensor and the well-established inductively coupled plasma mass spectrometry (ICPMS) while analysing various real drinking water samples. Prior to testing the real water samples, they were diluted with 5% HNO_3 as a necessary preparatory step for ICPMS analysis. This step ensures the stability of the samples during analysis, with no additional water treatment

was done thereafter. After dilution with 5%HNO_3 these real drinking water samples were analysed employing proposed optical fiber sensor and ICPMS. The experimental results, shown in Table 2, reveal a strong correlation between the Hg^{2+} concentrations determined by standard ICPMS (Agilent 7850) method and those obtained from the proposed optical fiber sensor. Additionally, the relative percentage difference (RPD) was calculated to assess the accuracy of the proposed sensor. The smaller the RPD value, the greater is the accuracy of the proposed method in comparison to the established method [93]. In order to find RPD, absolute change between the values obtained from ICPMS and from the optical fiber sensor were first measured. RPD was then calculated by dividing this absolute change by the average of the two values (one from ICPMS and the other from optical fiber sensor). As shown in Table 2, the calculated RPD values from the experimental data are below 1.5%. This indicates strong agreement between the two methods. These findings strongly confirm that the proposed optical fiber LSPR sensor serves as a reliable, simple, and cost-effective alternative to traditional methods like ICPMS for detecting Hg^{2+} ions accurately.

Table 2: Hg^{2+} concentration from different real water samples using ICPMS analysis and optical fiber sensor.

Sample	Mercury ion concentration ICPMS	Mercury ion concentration optical fiber sensor	RPD	RPD%
Drinking water	4.1 ppb	4.06 ppb	0.0098	0.98
Well water	4.4 ppb	4.42 ppb	0.0061	0.61
Tap water	4.8 ppb	4.79 ppb	0.0011	0.11
Near mill water	6.7 ppb	6.63 ppb	0.0103	1.03
Brahmaputra river	10.9 ppb	11.03 ppb	0.0125	1.25

2.4 Conclusion

A simple and reliable LSPR-based optical fiber mercury ion sensor with high sensitivity and selectivity is developed. GO-CS composite is used as the sensing material. The sensor exhibits a linear relationship between the mercury ion concentration and the LSPR wavelength shift

within the range of 0 to 200 ppb. Further, the proposed sensor is characterized with a sensitivity of 0.0728nm/ppb Hg^{2+} ion concentration. The sensor exhibits excellent selectivity for mercury ions compared to other heavy metal ions, and offers a remarkably low limit of detection of 0.29 ppb, which is significantly below the acceptable limit of mercury ions in drinking water recommended by the WHO and USEPA. Further, the proposed sensor exhibits fast response time of 0.6 sec. Additionally, the sensor shows high degree of repeatability, reversibility, stability and reliability. Furthermore, when the proposed sensor was utilized to detect mercury ion in real water samples, its results were in a good agreement with the standard ICPMS method validating the proposed sensors accuracy. Therefore, this sensor provides an efficient, simple, cost-effective, reliable and practical solution for monitoring mercury ions in real-field applications. Although the sensor shows high sensitivity, low LOD, and rapid response, there remains scope for further improving the sensitivity and achieving an even lower LOD. This laid the foundation for the development of another Hg^{2+} sensor, which is discussed in the next chapter.

Chapter 3 : LSPR based novel optical fiber mercury ion sensor employing CNT/PVA nanocomposite

3.1 Introduction

The previous chapter described the development of an LSPR based optical fiber mercury ion sensor utilizing GO-CS composite as the sensing film. While this sensor exhibited high sensitivity, a low detection limit, and a fast response time, there remains room for further enhancement—particularly in improving sensitivity and achieving an even lower detection limit. Hence, another novel LSPR based optical fiber mercury ion sensor is developed, which is reported in this chapter. Main objective is not only to achieve enhanced sensitivity, and a very low limit of detection, but also to achieve a response characteristic that is highly selective towards Hg^{2+} detection along with quick response time. To accomplish this, carbon nanotubes and Polyvinyl Alcohol (CNT/PVA) nanocomposite thin film was synthesized over a centrally decladded plastic-clad silica (PCS) fiber coated with gold nanoparticles. CNT was chosen for its exceptional adsorption capability towards Hg^{2+} ions [94]. On the other hand, PVA exhibits high sensitivity towards Hg^{2+} ions [67]. Combining these materials to form a nanocomposite is expected to enhance the sensitivity and selectivity towards Hg^{2+} ions. It is important to mention that CNT/PVA nanocomposite is used for the first time to realize an LSPR based optical fiber mercury ion sensor to the best of authors' knowledge. Experimental investigations demonstrate that the proposed sensor can accurately detect Hg^{2+} ions at ultra-low concentrations in the sub-parts per billion range, with a sensitivity of 0.2458 nm/ppb and a detection limit of 0.08 ppb. The sensor also demonstrates excellent selectivity towards Hg^{2+} ions and a rapid response time of 0.4 s. Additionally, the proposed sensor exhibits high degree of repeatability, stability, reversibility, and reliability. Furthermore, the proposed sensor is employed to detect mercury ions in real water samples, and the obtained results are validated from the standard inductively coupled plasma mass spectrometry (ICP-MS) method. These findings highlight the sensor's potential as a highly sensitive, selective, fast, and cost-effective tool for mercury ion detection in real-field applications.

3.1 Experiment

3.1.1 Synthesis of Carbon nanotubes and Polyvinyl Alcohol nanocomposite

To prepare the CNT/PVA nanocomposite, Polyvinyl Alcohol (PVA) (1 g) was dissolved in 10 ml of deionized water. The solution was then stirred continuously at 70-90 °C for 6 hours to

ensure complete dissolution of the PVA. Following this, a suitable amount of carbon nanotubes (CNTs) was dispersed in deionized water for 20 min using ultrasonication bath. After that, the CNT solution was added drop-wise into the PVA solution. The final solution is then stirred for 24 hr and ultrasonicated for 1 hr to form CNT/PVA nanocomposite [95].

3.1.2 Characterization of Carbon nanotbes and Polyvinyl Alcohol nanocomposite

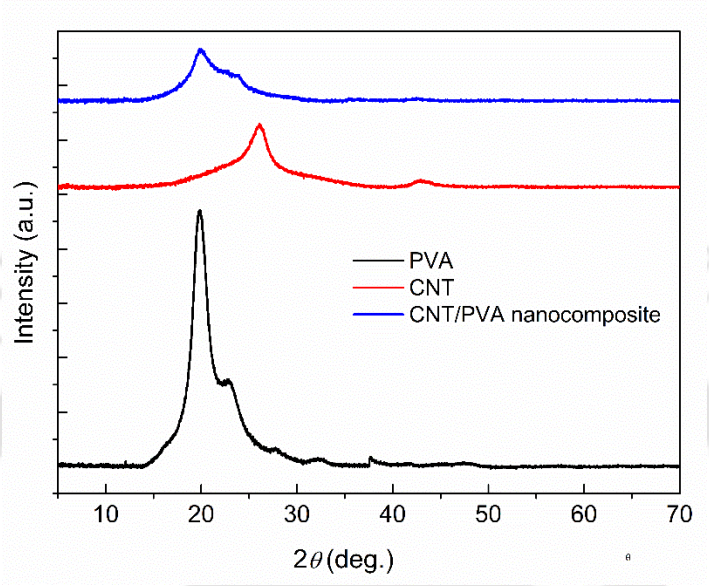

Figure 3.1: XRD of PVA, CNT and CNT/PVA nanocomposite.

For the structural characterization of PVA, CNT, and the CNT/PVA nanocomposite, X-ray diffraction (XRD) analysis was performed over a 2θ angle range of 5° to 80°. The measurements were conducted using a Rigaku TTRAX III X-ray diffractometer in Bragg-Brentano geometry, operating at 5 kW with Cu-Kα radiation (λ = 1.5406 Å). Fig. 3.1 presents the XRD patterns of PVA, CNT, and CNT/PVA nanocomposite. The diffraction pattern of PVA exhibits a peak at 19.87°, corresponding to the (101) plane, confirming its semi-crystalline nature [29]. The XRD pattern of CNT displays diffraction peaks at 26.10° and 42.94°, attributed to the (002) and (100) planes of the graphite structure of CNT. In the case of the CNT/PVA nanocomposite, only the characteristic diffraction peak of PVA (2θ = 19.87°) is observed, while the CNT peaks disappear. This suggests that the PVA peak overlaps with the CNT diffraction region, indicating a homogeneous dispersion of CNTs within the PVA matrix forming CNT/PVA nanocomposite [96].

Further, in order to investigate the nanostructure of CNT, FETEM analysis was conducted. Fig. 3.2 shows a typical FETEM image showcasing the morphology of multi walled CNTs. As can be observed from the figure the CNTs were curved and exhibited less tangling. Additionally, the CNTs showed a smooth surface with average diameter of the CNTs is determined to be 7±0.06 nm. Furthermore, the edges of the CNT were without caps and degraded (Fig. 3.2(b)).

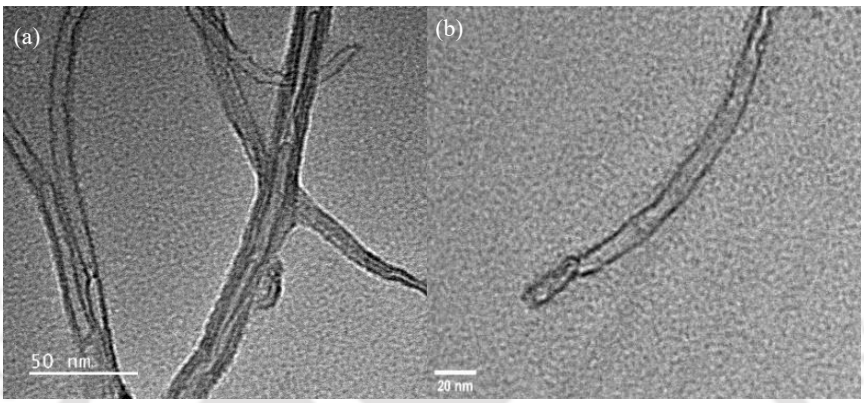

Figure 3.2: (a,b) FETEM image of CNT.

3.1.3 Preparation and Characterization of the sensing probe

To fabricate the sensing probe, a 40 cm-long plastic-clad silica (PCS) multimode fiber with a 600 µm core diameter was used. The fiber ends were meticulously prepared to ensure optically flat surfaces perpendicular to the fiber axis. This is a critical step for maximizing light coupling efficiency from source to the fiber and fiber to the detector. Subsequently, a 2.5 cm of the cladding was removed from the central region of the fiber. The decladded portion was thoroughly cleaned using a soap solution, deionized water, and acetone. After cleaning, the decladded section was carefully bent into a U-shape by exposing it to a propane flame. Probes only with a perfect U-shaped geometry and uniform core diameter in the bent region were selected for experimentation. In this study, U-shaped probes with a bending radius of 2.5 mm were employed. To prepare the sensing probe for gold nanoparticle attachment, same procedure is used as discussed in chapter 2. The AuNPs coated U-shaped optical probe is depicted in Fig 3.3(a). The thickness and the surface morphology of the coated region of the optical fiber core were examined using a Field Emission Scanning Electron Microscope (FESEM) (Zeiss, Sigma 300). Fig 3.3(b) depicts the image of a section of AuNPs coated U-shaped optical fiber. In this region, an average fiber diameter of approximately 600.08 µm was observed. This establishes a thickness of the AuNPs film as ~40 nm. Fig. 3.3(c) highlights the surface morphology of the

deposited AuNPs film, demonstrating a high-density and uniform coating of nanoparticles on the decladded fiber surface.

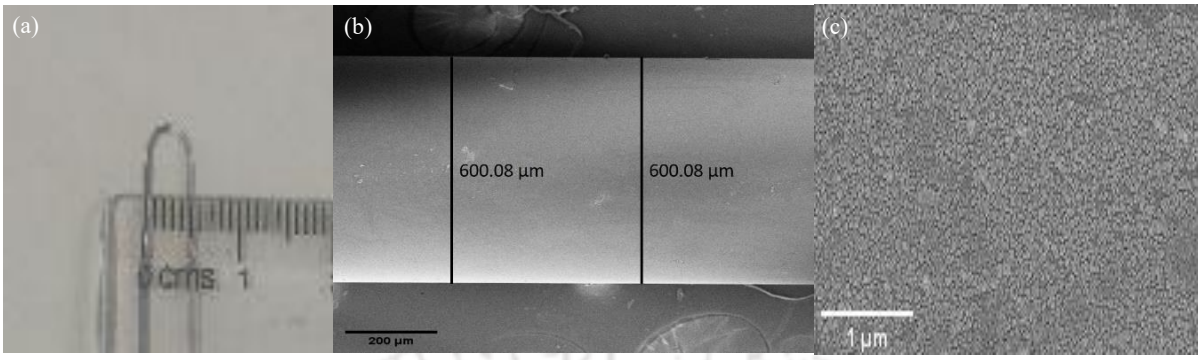

Figure 3.3: (a) AuNPs coated U-shaped probe, (a) FESEM image of the centrally decladded region of the fiber carrying AuNPs coating, (b) FESEM picture of surface morphology of the AuNPs coated region.

In the subsequent step, the AuNP-coated probe was further coated with CNT/PVA nanocomposite. To evaluate the effect of the sensing film composition on the sensor performance, the amount of CNT used in the formation of the CNT/PVA nanocomposite was varied from 0.1 g, 0.15 g, and 0.2 g. Afterwards, the dip-coating method was employed, wherein the AuNP-coated U-shaped region of optical fiber probe was dipped into the CNT/PVA nanocomposite solution of fixed CNT concentration. Separate sensors were developed by coating AuNP-coated probe with varying CNT concentration in the CNT/PVA nanocomposite solution. Afterwards, these dip coated probes were allowed to dry at room temperature for two days. The surface morphology, nanostructure, and thickness of the deposited films were analyzed using a Field Emission Scanning Electron Microscope (FESEM). For example, Fig. 3.4(a) shows the FESEM picture of a section of U-shaped optical fiber probe having CNT/PVA

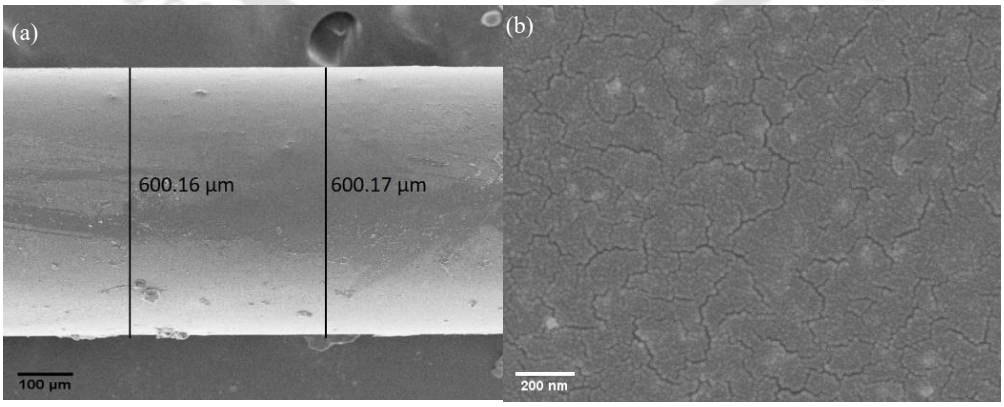

Figure 3.4: (a) FESEM image of the centrally decladded region of the fiber coated with CNT/PVA nanocomposite over the AuNPs coating film. (b) FESEM pattern of surface morphology of the CNT/PVA nanocomposite coating region.

nanocomposite coating that corresponds to 0.15g CNT in 1g PVA solution. The measured average diameter of this region is observed to be approximately 600.165 µm. Considering ~40 nm thickness of the gold nanoparticles layer, this establishes an average thickness of ~42.5 nm for the CNT/PVA nanocomposite film. Similarly, the sensing film thickness for other compositions is observed to be ~25 nm for 0.1 g CNT and ~57.5 nm for 0.2 g CNT. Fig. 3.4(b) illustrates the surface morphology of the CNT/PVA nanocomposite sensing film, revealing an interconnected structure with a high-quality, moderately rough surface coating.

Similar procedures, as explained in chapter 2, were followed in order to characterize each sensing probe. During the experiment Hg^{2+} concentrations were varied from 0-30 ppb.

3.2 Result and Discussion

3.2.1 Response of the proposed LSPR optical fiber sensor towards Hg^{2+} ions detection

The proposed sensor exploits the localized surface plasmon resonance (LSPR) technique to detect Hg^{2+} ions, utilizing a CNT/PVA nanocomposite as the sensing material, which is coated onto the gold nanoparticles coated core of a U-shaped optical fiber. To optimize the sensor's response characteristics, the effect of the sensing film configuration onto the sensor's performance were investigated. For that, the concentration of CNT in the PVA solution was varied, starting at 0.1 g then increasing to 0.15 g and finally 0.2 g. Each change in CNT concentration resulted in a corresponding increase in the sensing film's thickness, as measured by FESEM: approximately 27.5 nm for 0.1 g, 38.33 nm for 0.15 g, and 63.33 nm for 0.2 g. To evaluate the performance characteristics of the proposed sensor, outputs of the proposed sensor were monitored in real time while exposing it to mercury ion solutions with varying concentrations ranging from 0 to 30 ppb. As an example, Fig. 3.5 presents the resulting LSPR spectra for the sensing probe with a film composition of 0.15 g of CNT. These results establish a strong correlation between the Hg^{2+} ion concentration and the LSPR response, as increasing the Hg^{2+} ion concentration results in a noticeable red-shift in the resonance wavelength. This shift in the LSPR wavelength can be attributed to the changes in the refractive index of the surrounding medium around the AuNPs when the sensor is exposed to the Hg^{2+} ion solution. When the proposed sensor is exposed to Hg^{2+} ions solution, the Hg^{2+} ions get adsorbed onto the highly electronegative hydroxyl groups on the surface of the CNT/PVA nanocomposite. Due to the adsorption of the Hg^{2+} ions onto the CNT/PVA nanocomposite film, refractive index

of the environment surrounding the gold nanoparticles increases. This, in turn, causes a red shift in the resonance wavelength of the LSPR spectrum. In order to get a deeper insight, the response for each film composition was analyzed by plotting the dip resonance wavelength against varying Hg^{2+} ion concentrations. Fig.3.6 shows the response of the sensors with varying film composition.

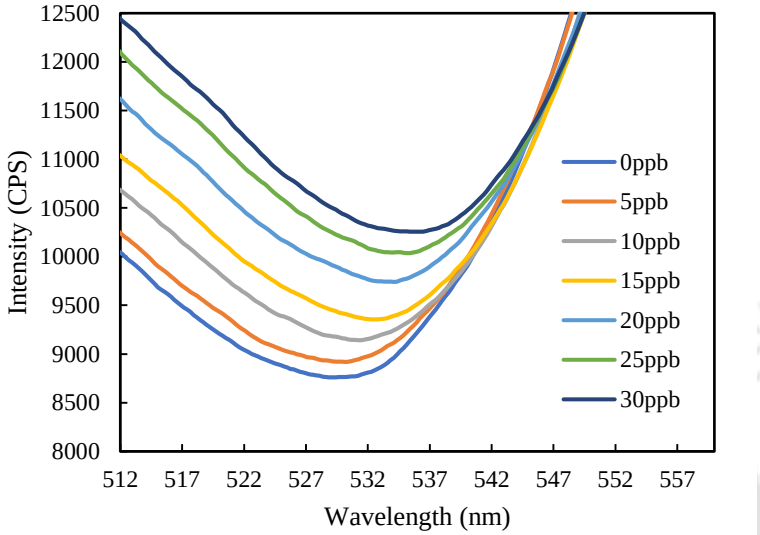

Figure 3.5: LSPR spectrum with varying mercury ion concentrations.

As can be observed from the figure, all the sensors with different film compositions exhibit a linear response across the range of 0–30 ppb for Hg^{2+} concentrations. The sensor with film composition of 0.1 g CNT in the CNT/PVA nanocomposite demonstrated a sensitivity of 0.1881 nm/ppb. Increasing the CNT concentration in the nanocomposite from 0.1g to 0.15g enhanced the sensitivity to 0.2458 nm/ppb, approximately 1.3 times higher than that of the 0.1g of CNT composition. This improvement in sensitivity is attributed to the greater number of electronegative sites available for Hg^{2+} ion adsorption, resulting from the increased CNT concentration. The higher adsorption led to more significant changes in the local refractive index near the gold nanoparticles, thereby causing a larger resonance wavelength shift in the LSPR spectrum. However, further increasing the CNT concentration in the nanocomposite from 0.15g to 0.2g resulted in a sensitivity decrease to 0.1639 nm/ppb, about 1.49 times lower than the sensitivity observed for the 0.15g composition. This reduction in sensitivity is primarily due to the increased thickness of the sensing film. In the case of 0.2g of CNT in CNT/PVA nanocomposite, the thickness of the film exceeds the LSPR decay length (20–40 nm) [91]. When the film thickness surpasses the decay length, Hg^{2+} ions are hindered from

reaching regions close to the gold nanoparticles. Interaction of Hg^{2+} ions with CNT/PVA nanocomposite beyond the decay length didn't contribute significantly to the sensing process, and hence, didn't significantly impact the resonance wavelength shift. This is the reason for the reduced sensitivity of the 0.2g CNT in CNT/PVA nanocomposite film composition. These findings establish that there exists an optimal film composition of 0.15g of CNT in the CNT/PVA nanocomposite.

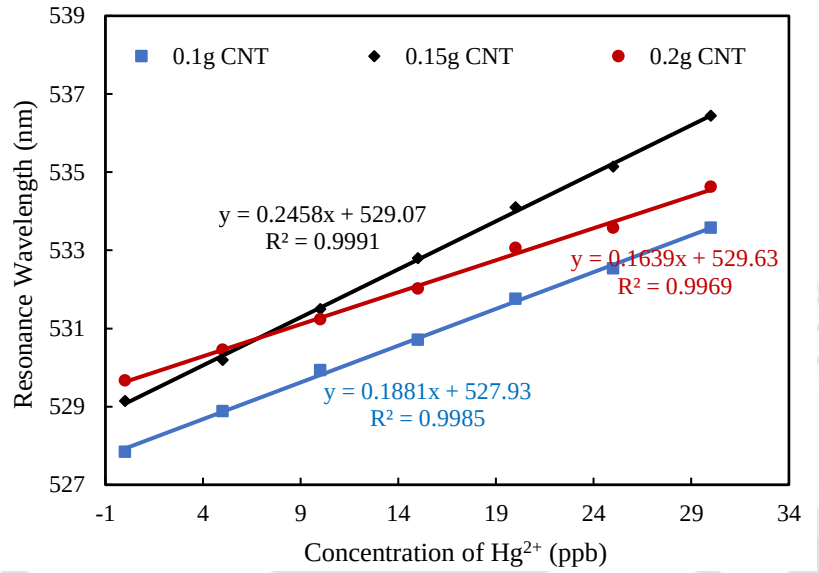

Figure 3.6: Sensor response with different film compositions (0.1g, 0.15g and 0.2g of CNT in CNT/PVA nanocomposite).

3.2.2 Limit of detection

In addition to sensitivity, as already discussed, the limit of detection (LOD) is a critical parameter for assessing a sensor's performance. The LOD reflects the sensor's ability to detect the lowest concentration of an analyte. The LOD of the optimized sensor was determined to be 0.08 ppb. The achieved LOD is approximately 75 times lower than the permissible limit for mercury ions in drinking water established by the WHO and 25 times lower than the USEPA standard. This demonstrates that the LSPR sensor can accurately detect mercury ions at concentrations well below the regulatory thresholds, highlighting its potential for ensuring the safety of drinking water.

3.2.3 Reusability, Reversibility and Response Time of the sensor

Reusability/repeatability and reversibility are other essential parameters for evaluating sensor performance. To evaluate these characteristics, the sensor was tested by exposing it to both the minimum (5 ppb) and maximum (30 ppb) Hg^{2+} ion concentrations. Initially, the sensor was exposed to a 5 ppb Hg^{2+} solution within the flow cell, and the corresponding LSPR spectrum was recorded. After allowing the sample to remain in the flow cell for 1 minute, the LSPR spectrum was recorded again. Subsequently, the 5 ppb solution was removed, and the sensor was thoroughly rinsed with deionized water to eliminate any residual Hg^{2+} ions. The sensor was then exposed to a 30 ppb Hg^{2+} solution, and LSPR spectra were recorded at 1-minute intervals. To complete one cycle, the 30 ppb solution was removed, the sensor was cleaned, and the 10 ppb Hg^{2+} solution was reintroduced into the flow cell. The LSPR spectrum was again recorded at 1-minute intervals and compared to the initial measurement. This whole cycle was repeated several times. Typical response for 4 cycles is presented in Fig. 3.7(a). The resonance wavelength remained consistent across cycles at the lower Hg^{2+} concentration, confirming the absence of residual ions on the sensor after exposure to higher concentrations. The results confirm the sensor's capability to produce consistent responses during both forward (5 ppb to 30 ppb) and reverse (5 ppb to 30 ppb) changes in Hg^{2+} ion concentration. These results demonstrate that the proposed sensor is highly repeatable and fully reversible.

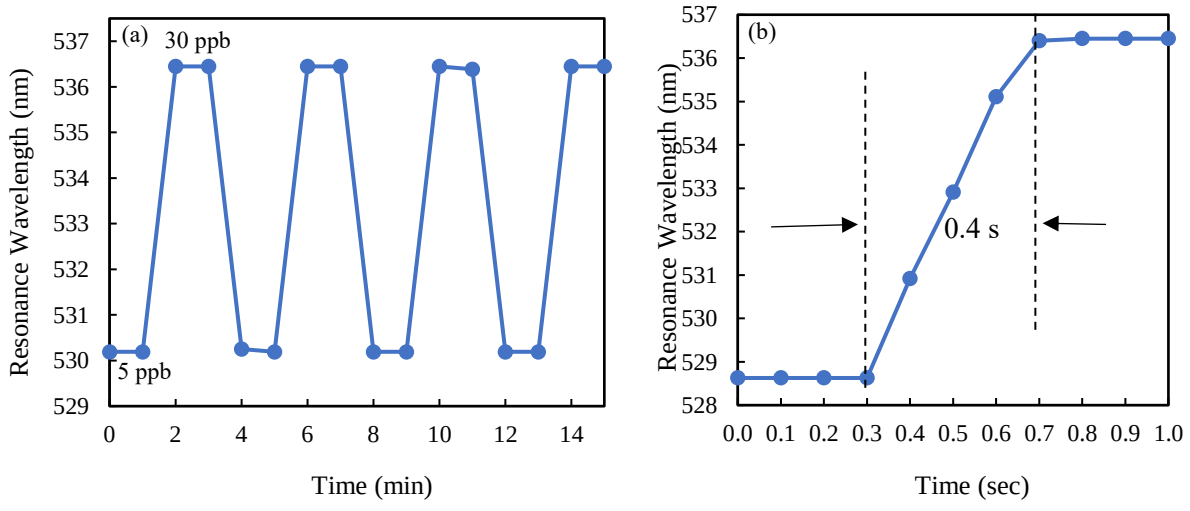

Figure 3.7: (a) Repeatability and reversibility characteristics of the proposed sensor. (b) Response time (during the variation from air to 30 ppb Hg^{2+}).

The detection speed is another crucial parameter for evaluating sensor performance. Achieving a rapid response time being particularly significant for a sensor. To assess the response time of

the proposed sensor, the LSPR resonance wavelength was measured both before and after introducing a 30 ppb Hg^{2+} ion solution into the flow cell. LSPR spectra were recorded at every 0.1 seconds, and the corresponding resonance wavelength values were determined. The results of these measurements are presented in Fig. 3.7(b), which plots resonance wavelength values against time. As can be observed, the resonance wavelength remains stable prior to the introduction of the Hg^{2+} solution (when the sensor is exposed to air). Upon introducing the Hg^{2+} ion solution into the flow cell, the resonance wavelength initially undergoes a red shift, then gradually stabilizes at approximately 0.4 seconds. These findings highlight the proposed sensor's rapid response time of 0.4 seconds.

3.2.4 Selectivity of the sensor

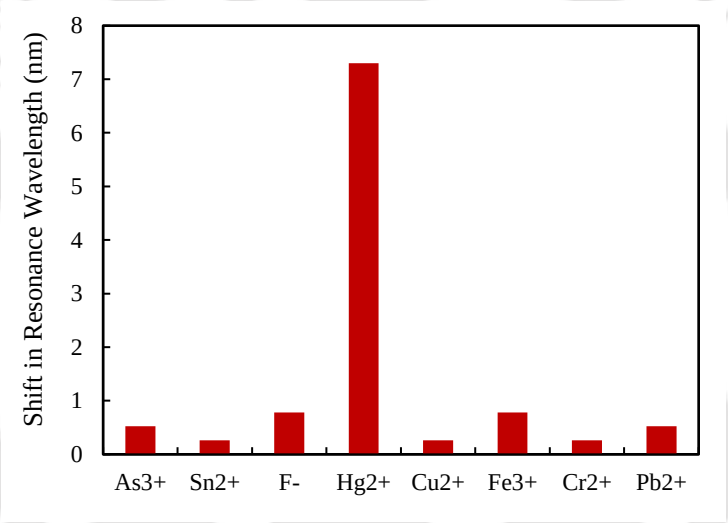

Figure 3.8: Comparison of the resonance wavelength shift of the sensor with different heavy metal ions.

Selectivity is another very critical parameter for evaluating the performance of a sensor. To determine the selectivity of the proposed sensor, experiments were conducted with various heavy metal ions commonly found in groundwater, including As^{3+}, Sn^{2+}, F^{-}, Cu^{2+}, Fe^{3+}, Cr^{2+}, and Pb^{2+}. These heavy metal ions can potentially interfere in the detection of Hg^{2+}. For the experiment, the concentration of each heavy metal ion solution was maintained at 10 parts per million (ppm), except for Hg^{2+}, which was tested at ~333 times lower concentration of 30 ppb. During the experiment, the sensor probe was immersed in each heavy metal ion solution, and the corresponding LSPR spectrum was recorded using the same experimental setup employed for mercury ion detection. The shift in the resonance wavelength was measured for changes in concentration from 0 to 10 ppm for all heavy metal ions, while for Hg^{2+}, the wavelength shift

was evaluated for concentrations ranging from 0 to 30 ppb. As shown in Fig. 3.8, the sensor probe exhibited a significantly greater shift in resonance wavelength for mercury ions compared to other heavy metal ions, even when the concentration of Hg^{2+} is as low as 30 ppb. The exceptional selectivity of the proposed sensor for Hg^{2+} ions can be attributed to the synergistic effect of combining CNT and PVA into a nanocomposite, which significantly enhances its adsorption capacity for Hg^{2+} ions. The superior adsorption efficiency of PVA for Hg^{2+} ions, compared to other heavy metal ions, further amplifies the sensor's selectivity [97]. This results in a more pronounced shift in the resonance wavelength specifically for mercury ions. These findings demonstrate that the proposed optical fiber sensor is highly selective for mercury ions, highlighting its potential for effective mercury ion detection in real-world applications.

3.2.5 Stability and Reliability of the sensor

Stability and reliability are other critical parameters of a sensor. To evaluate these characteristics, a comprehensive analysis was performed to determine both the short-term and long-term performance of the proposed sensor. Short-term stability of the sensor was examined by continuously recording the LSPR spectrum at 1-minute intervals over a period of 16 minutes while exposing the sensor to three different Hg^{2+} ion concentrations (5 ppb, 20 ppb, and 30 ppb). The results, presented in Fig. 3.9. The standard deviations of the resonance wavelength were found to be ±0.008 nm, ±0.01 nm, and ±0.01 nm for 5 ppb, 20 ppb, and 30 ppb Hg^{2+} ion concentrations, respectively. This corresponds to a maximum resolution of ±0.04 ppb for Hg^{2+} ions, underscoring the sensor's remarkable stability and accuracy. To evaluate the long-term stability or reliability test, the developed optical fiber Hg^{2+} sensor was tested on four different days with a 5-day interval, at three different Hg^{2+} concentrations (5 ppb, 20 ppb, and 30 ppb) over an 18-day span. The results observed over the course of 18 days are presented in Fig. 3.10. As can be observed from the figure that the maximum variation in the resonance wavelength of the developed Hg^{2+} optical fiber sensor is less than 0.002% of the resonance wavelength recorded on the first day. This outcome highlights the exceptional repeatability and reliability of the developed optical fiber Hg^{2+} sensor.

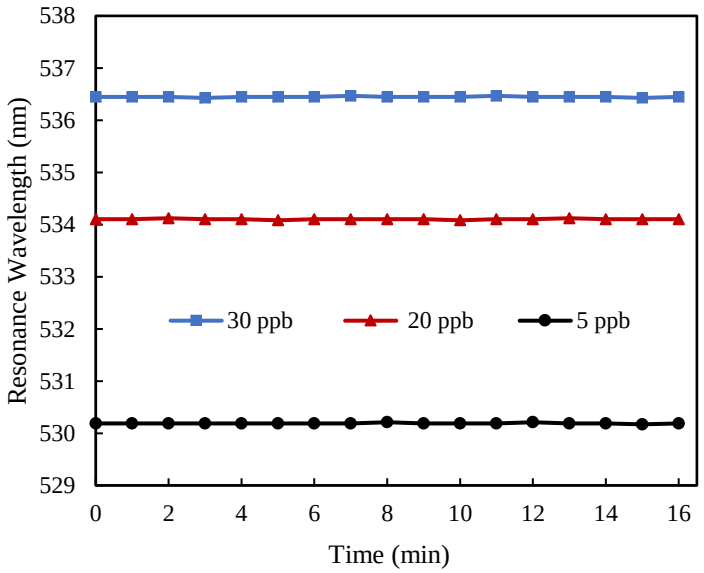

Figure 3.9: Short term stability test: Continuous resonance wavelength for 16 minutes at 5ppb, 20ppb and 30ppb Hg^{2+} concentration.

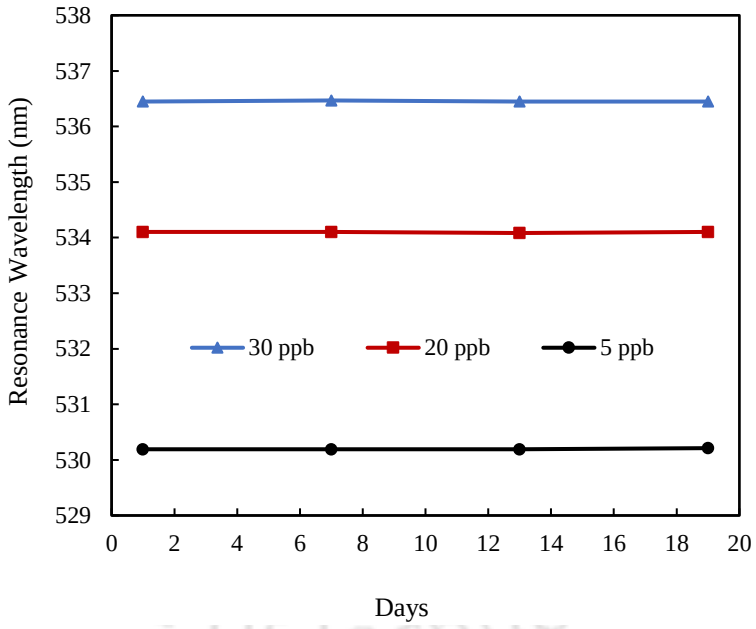

Figure 3.10: Repeatability and reliability test: Resonance wavelength on four different days at 5ppb, 20ppb and 30ppb Hg^{2+} concentration.

3.2.6 Mercury detection in real samples and validation of the sensor

To validate the commercial applicability of the proposed sensor, experiments were conducted using real drinking water samples collected from various sources in Guwahati, Assam, India. These sources included drinking water from Indian Institute of Technology Guwahati, tap water from a nearby locality, water from a site near a mill in Guwahati city, and samples from the

Brahmaputra River. To validate the accuracy of the proposed sensor for detecting Hg^{2+} ions, the results obtained from the optical fiber sensor were compared with those from the established inductively coupled plasma mass spectrometry (ICPMS) method. Before testing the real water samples, they were diluted with 5% HNO_3 which is a necessary preparatory step for ICPMS analysis. The experimental results, presented in Table 3, demonstrate a strong correlation between the Hg^{2+} concentrations measured using the standard ICPMS (Agilent 7850) method and those obtained from the proposed optical fiber sensor. To evaluate the accuracy of the proposed sensor, the relative percentage difference (RPD) was calculated. A lower RPD value indicates higher accuracy of the proposed method compared to the established method [93]. As shown in Table 3, the RPD values from the experimental data are below 4%, indicating excellent agreement between the two methods. These findings confirm that the proposed optical fiber LSPR sensor is a reliable, straightforward, and cost-effective alternative to conventional techniques like ICPMS for accurate Hg^{2+} ion detection.

Table 3: Hg^{2+} concentration from different real water samples using ICPMS analysis and proposed optical fiber sensor.

Sample	Mercury ion concentration ICPMS	Mercury ion concentration optical fiber sensor	RPD	RPD%
Drinking water	4.1 ppb	4.13 ppb	0.0089	0.89
Well water	4.4 ppb	4.34 ppb	0.0116	1.16
Tap water	4.8 ppb	4.77 ppb	0.0055	0.55
Near mill water	6.7 ppb	6.89 ppb	0.0287	2.87
Brahmaputra river	10.9 ppb	10.50 ppb	0.0371	3.71

3.3 Conclusion

A simple and reliable LSPR based optical fiber sensor for mercury ion detection is developed, employing CNT/PVA nanocomposite as the sensing material. The sensor demonstrates a linear relationship between mercury ion concentration and the LSPR wavelength shift within the range of 0 to 30 ppb, with a high sensitivity of 0.2458 nm/ppb. It offers excellent selectivity for mercury ions over other heavy metal ions and achieves an exceptionally low limit LOD of 0.08 ppb. This achieved LOD is well below the acceptable mercury ion limits in drinking water

recommended by the WHO and USEPA. The sensor also exhibits a rapid response time of just 0.4 seconds and exhibits outstanding repeatability, reversibility, stability, and reliability. Further, when tested on real water samples, the sensor's results closely matched those obtained using the standard ICPMS method, validating its accuracy. Therefore, this proposed LSPR based optical fiber Hg^{2+} sensor provides a highly efficient, practical, and cost-effective solution for monitoring mercury ions in real-world applications. Moreover, it is evident that, the reported sensor demonstrates an enhanced sensitivity, an even lower LOD (~3.6 times) and a faster response time in comparison to chapter 2, while maintaining high selectivity, stability, repeatability and reliability.

Chapter 4 : Localized Surface Plasmon Resonance based Novel Optical Fiber Arsenic Ion Sensor Employing Al_2O_3/GO Nanocomposite

4.1 Introduction

Arsenic, another very toxic heavy metal, poses a substantial health risk even at low concentrations. It's often found in groundwater due to natural geothermal processes and can be released into the environment through human activities, including the use of pesticides, herbicides, and mining processes. Continuous consumption of arsenic-contaminated water can result in arsenic poisoning and various cancers like skin, lung, kidney, and bladder cancer [29]. The World Health Organization (WHO) has established a maximum allowable limit of 10µg/L (10 ppb) for arsenic in drinking water. In natural water settings, arsenic contamination occurs primarily in two inorganic forms: arsenite (As^{3+}) and arsenate (As^{5+}). As^{3+} is significantly more toxic, being 20-60 times more potent than As^{5+}, and it's also more challenging to eliminate [98]. Given the severe effects of As^{3+}, it's crucial to prioritize the development of a reliable and sensitive detection method. Various conventional techniques have been devised for arsenic ion detection, including atomic absorption spectroscopy [31], inductively coupled plasma mass spectroscopy [33], high-performance liquid chromatography [35], hydride generation atomic fluorescence [99] and colorimetric sensors [37], [100], [101]. These methods are highly accurate and sensitive. However, they have drawbacks such as they are complex, bulky, expensive, time-consuming, and require skilled personnel, which limits their widespread use. In contrast, Surface plasmon resonance (SPR) and Localized Surface Plasmon Resonance (LSPR) have emerged as a promising alternative for heavy metal ion detection due to their simplicity, rapid response, cost effective, easy sample preparation and high sensitivity. Both LSPR and SPR are highly responsive to changes in localized refractive index, thereby showing a corresponding shift in the resonance wavelength. Therefore, this field has caught the attention of researchers and hence several LSPR and SPR based As^{3+} have been reported. For instance, as discussed in Chapter 1 from references [44 – 45]. These techniques show good limit of detection (LOD), but the LOD needs to be further improved for detecting As^{3+} in drinking water. Compared to the non-optical fiber based LSPR and SPR sensors, optical fiber based LSPR and SPR sensors offer several advantages, e.g., high sensitivity, remote sensing, multiplexing, rapid response, real-time detection, cost-effectiveness, and durability for real-field applications with a possibility of miniaturization. Only few SPR or LSPR based optical

fiber As^{3+} sensors are reported so far. For example, as discussed in Chapter 1 from references [74, 102, 75]. This sensor showcased a low LOD of 1 ppb. Among these reported sensors, observed LOD for many were above the threshold, WHO has set for As^{3+} ions in drinking water. This limits the suitability and applicability of these sensors for the detection of As^{3+} ion in drinking water. Some reported sensors with low LODs lack selectivity; while others exhibit slow response time. Additionally, only few sensors demonstrated reusability. Consequently, there is a significant need to develop an optical fiber sensor that is characterized with a very low detection limit, high selectivity, optimal sensitivity, reusability, and rapid response for being suitable towards real-world applications.

Main objective of the research work presented here is to develop LSPR based optical fiber arsenic sensor to achieve high sensitivity, low limit of detection, high selectivity and rapid response time. To achieve this, a novel optical fiber sensor is proposed where a thin (nanostructured) film of Al_2O_3/GO nanocomposite is synthesized over the centrally decladded region of plastic-clad-silica (PCS) fiber already coated with gold nanoparticles. The reason for using Al_2O_3/GO nanocomposite as the sensing material for detecting arsenic ion is based on the exceptional adsorption capability of graphene oxide (GO) for heavy metal ions, primarily due to its high surface area to volume ratio [103]. GO, a crucial derivative of graphene, is a two-dimensional nanomaterial. The monolayer of GO contains sp^2 and sp^3 hybridized carbon atoms, alongside oxygen-rich functional groups like hydroxyl and epoxide groups on the basal plane, and carbonyl and carboxyl groups at the edge [104]. These functional groups possess a strong binding affinity to heavy metal ions [103]. On the other hand, Al_2O_3 exhibits high sensitivity and selectivity in detecting As^{3+} ions, which is attributed to its oxygen-rich electronegative adsorption sites and already established in [105], [106]. Combining these materials to form a nanocomposite creates a synergistic effect, increasing the number of adsorption sites due to the large surface to volume ratio, thereby enhancing suitable sensitivity and selectivity [107], [108]. Hence, Al_2O_3/GO nanocomposite is expected to enhance the sensitivity and selectivity of As^{3+} detection. It is important to mention that Al_2O_3/GO nanocomposite is used for the first time to realize an optical fiber arsenic sensor to the best of authors' knowledge. Experimental investigation highlights that the integration of Al_2O_3/GO nanocomposite onto the gold nanoparticles (AuNPs) coated LSPR sensing probe enables the sensor to accurately detect arsenic (As^{3+}) ions, even at extremely low concentrations in the sub-parts per billion range. Most importantly, the proposed sensor exhibits a remarkable sensitivity

of 0.217 nm/ppb As^{3+} ion concentration and an exceptionally low limit of detection of 0.09 ppb As^{3+} ion concentration. The sensor also exhibits a very fast response time of 0.5 s. Moreover, the sensor exhibits high degree of repeatability, stability, reversibility and reliability. The results obtained from this investigation highlight the potential of the proposed sensor as a highly sensitive, selective, rapid and cost-effective arsenic sensor for real-field applications. Furthermore, the proposed sensor is utilized to detect arsenic in real water samples and the results are validated from the standard inductively coupled plasma mass spectrometry (ICPMS) method.

4.2 Experiment

4.2.1 Synthesis and characterization of Al_2O_3/GO nanocomposite

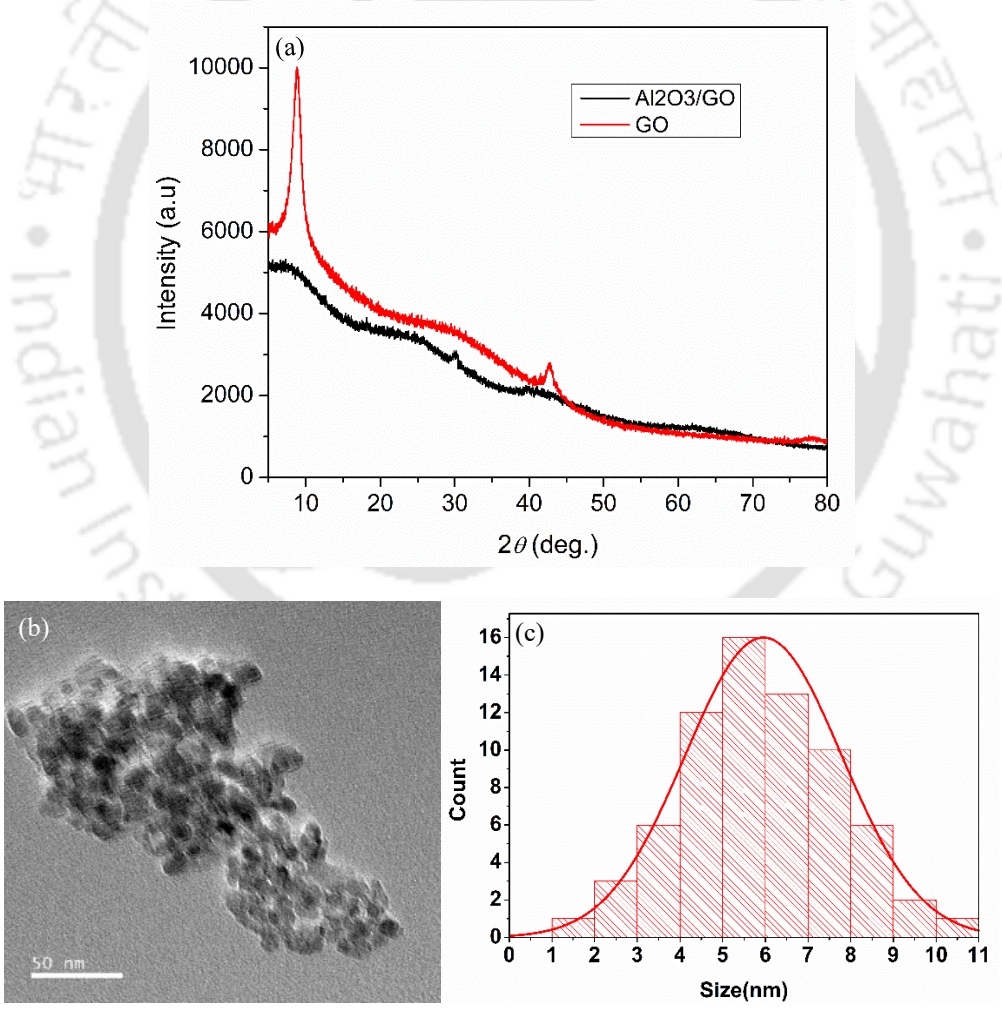

Figure 4.1: (a) XRD pattern of GO and Al_2O_3/GO nanocomposite, (b) FETEM image of Al_2O_3/GO nanocomposite, (c) Size distribution within the Al_2O_3/GO nanocomposite.

Graphene oxide (GO) was synthesized from graphite by using the Modified Hammers method [89]. To synthesize Al_2O_3/GO nanocomposite, 1g of GO was dispersed in 100 mL of DI water using an ultrasonic bath for 1 hour. Subsequently, 5g of aluminium nitrate ($Al(NO_3)_3 \cdot 9H_2O$) was added to the mixture. The solution was then subjected to ultrasonic treatment for 2 hours at a controlled temperature below 30°C. Afterward, the suspension was dried at 100°C for 10 hours. Finally, the solid sorbent was heated in a furnace at 500°C for 2 hours, resulting in the production of Al_2O_3 nanoparticles on the surface of GO. This process yielded a grey product known as Al_2O_3/GO nanocomposite.

For the structural characterization of the prepared GO and Al_2O_3/GO nanocomposite, X-ray diffraction patterns (XRD) were obtained. For that, the data were recorded in the 2θ range of 5° to 80° using an X-ray diffractometer (XRD, Rigaku TTRAX III) with Cu-Kα radiation (λ = 1.5406 Å) operating at 5 kW in Bragg–Brentano geometry. Fig. 4.1(a) displays the XRD spectra of GO and Al_2O_3/GO nanocomposite. GO exhibits a prominent peak at 10.2° (001) in its XRD pattern, indicating an interlayer spacing of approximately 0.8 nm. In the Al_2O_3/GO nanocomposite, the characteristic peaks of GO are no longer observed. Instead, the XRD pattern displays a smooth background with a high intensity at low angles that gradually decreases at higher theta angles. This pattern resembles simulated XRD patterns for nano-sized, single layers of carbon structures [109]. The absence of distinct peaks in the XRD pattern of the nanocomposite suggests the absence of crystalline entities within the nanocomposite. It can be explained by the amorphous nature of Al_2O_3 in the composite, as Al_2O_3 tends to adopt an amorphous structure when treated at temperatures ≤ 500°C [110]. In order to investigate the surface morphology and size distribution of the developed nanocomposite, further analysis was carried out using a field-emission transmission electron microscope (FETEM, JEOL-2100F). Fig. 4.1(b) displays a typical FETEM image of Al_2O_3/GO nanocomposite, which indicates that the Al_2O_3 nanoparticles are uniformly entrapped and distributed on the surface of GO. Fig. 4.1(c) illustrates the size distribution within the developed Al_2O_3/GO nanocomposite. As can be seen, particle size is predominantly in the range of 3–9nm, with an average particle size of 6±0.06nm.

4.2.2 Sensor preparation and characterization

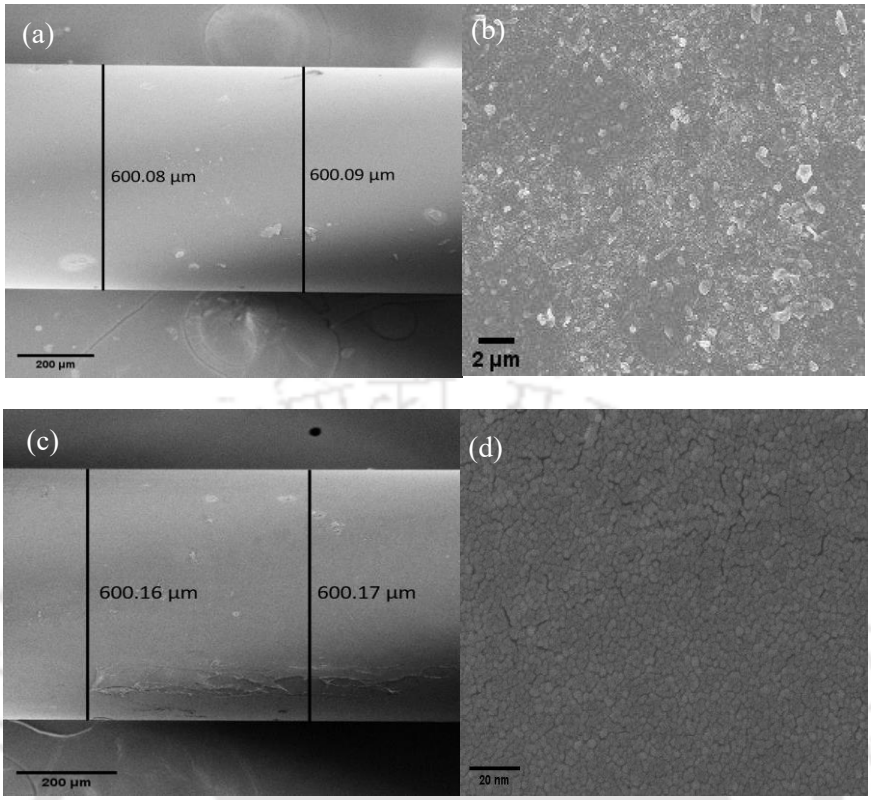

Figure 4.2: (a) FESEM image of the centrally decladded region of the fiber carrying AuNPs coating. (b) FESEM pattern of surface morphology of the AuNPs coated region. (c) FESEM image of the centrally decladded region carrying Al_2O_3/GO nanocomposite film over the AuNPs coated fiber core. (d) FESEM pattern of the surface morphology of Al_2O_3/GO nanocomposite coated region.

A plastic clad silica (PCS) multimode optical fiber of 600 µm core diameter is used to develop the sensor. Total length of 40cm was taken and both the ends of the fiber were polished to get optically flat end-faces in the transverse section of the fiber. This is critically important in order to achieve maximum power coupling efficiency from source to the fiber and fiber to the detector. Cladding was removed from the 2.5 cm long central section of the fiber. The decladded section was cleaned with soap solution, de-ionized water, and acetone. Afterwards, this decladded section of the fiber was carefully bent into a U-shape by exposing it to a propane flame. Experiments were performed only on the probes having perfect U-shape and uniform core diameter in the U-shaped region. U-shaped probes having a diameter of 4 mm are employed in this research. In order to attach gold nanoparticle, similar procedures are employed to as discussed in chapter 2. The thickness and surface morphology of the gold nanoparticle coating on the optical fiber core was analyzed using a Field Emission Scanning Electron Microscope (FESEM) (Zeiss, Sigma 300). Fig 4.2(a) depicts image of the coated region of optical fiber. An average diameter of ~600.085 µm was observed for this region, which

establishes the average thickness of AuNPs film as ~42.5 nm. Surface morphology of the deposited AuNPs film onto the fiber core is depicted in Fig. 4.2(b). This image illustrates not only a high density but also a uniform coating of AuNPs on the decladded fiber surface.

In the next step and to add a coating of Al_2O_3/GO nanocomposite onto the probe, already coated with AuNPs, an appropriate amount of Al_2O_3/GO nanocomposite was dissolved in a suitable amount of Isopropyl Alcohol (IPA) under continuous stirring for 1-2 hours. In order to investigate the effect of sensing film composition on the sensor performance, amount of Al_2O_3/GO nanocomposite dispersed in IPA was varied as 1mg/ml, 1.5mg/ml, 2mg/ml. Dip-coting method was employed afterwards, where AuNPs deposited U-shaped region of different probes were slowly dipped into the three solutions separately. Thereafter, these dip-coated probes were dried for two days at room temperature. Surface morphology, nanostructure, and deposited film thickness were examined using FESEM. Fig. 4.2(c) displays an image of the nanocomposite coated sensing region of the optical fiber that already carried a coating of AuNP onto the decladded core, as an example, for the Al_2O_3/GO nanocomposite concentration of 1.5mg/ml in IPA. An average diameter of ~600.165 µm is observed for this region. With the thickness of AuNP coating already determined as ~42.5 nm, this establishes an average thickness of ~40 nm for the Al_2O_3/GO nanocomposite sensing film. Similarly, the thicknesses for the other two film compositions are determined to be ~22.5 nm (for 1mg/ml of nanocomposite) and ~62.5 nm (for 2mg/ml of nanocomposite). Surface morphology of the final sensing probe is shown in Fig. 4.2(d), which illustrates an interconnected, high-quality coated surface with moderate roughness.

To analyze the response characteristics, the same procedures discussed in Chapter 2 for sensing probe characterization were followed. Throughout the experiment, As^{3+} concentrations were varied from 0 ppb to 20 ppb.

4.3 Result and discussion

4.3.1 Response of the proposed LSPR based optical fiber sensor towards As^{3+} ions detection

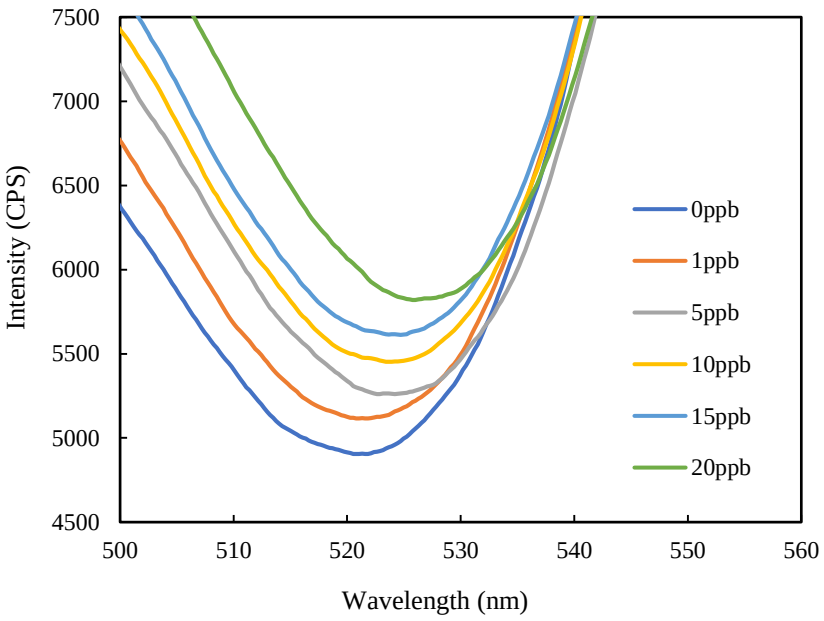

Figure 4.3: Variation of transmittance of the optical fiber with different arsenic ion concentrations.

Proposed sensor exploits the phenomena of localized surface plasmon resonance through a thin sensing film of Al_2O_3/GO nanocomposite, synthesized onto the gold nanoparticles coated U-shaped optical fiber probe. In order to optimize the response characteristics of the sensor, impact of the composition of the sensing film was studied. For this, concentration of Al_2O_3/GO nanocomposite was varied in IPA to create different sensing film compositions. Specifically, the amount of nanocomposite in IPA solution was varied from 1mg/ml, to 1.5mg/ml, and finally, to 2mg/ml. Varying composition of the sensing film resulted in a proportional change in the thickness of the film. FESEM measurements reveal a film thickness of ~22.5nm for 1mg/ml, ~40nm for 1.5mg/ml, and ~62.5nm for 2mg/ml nanocomposite composition. To examine the performance characteristics of the proposed sensor, outputs from the sensor were monitored in real-time while exposing the sensor to the solutions of As^{3+} concentrations varying in the range of 0–20ppb. Fig. 4.3 depicts the resulting LSPR spectra, as an example, for the sensing probe having film composition of 1.5mg/ml Al_2O_3/GO nanocomposite in IPA solution. Notably, a significant red shift for the dip resonance wavelength, accompanied by an increase in the transmittance is observed while increasing the concentration of arsenic ions. This is because of the fact that, when the sensor is exposed to As^{3+} ions solution, As^{3+} ion gets adsorbed

on the electronegative sites (hydroxyl, epoxide, carbonyl, carboxyl) present on the surface of Al_2O_3/GO nanocomposite. The adsorption of As^{3+} ions on the surface of the nanocomposite increases the refractive index of the surrounding medium of the gold nanoparticles. This results in the observed red shift of the resonance wavelength in the LSPR spectrum. In order to get a deeper insight, the dip resonance wavelength corresponding to the applied arsenic concentration is plotted in Fig. 4.4 for each composition of the sensing film. As can be observed from the figure, all the sensors with different film composition exhibit linear response over the measurement range of 0–20 ppb for As^{3+} concentration. The sensor with film composition corresponding to 1mg/ml shows sensitivity of 0.1167nm/ppb. Upon increasing the concentration of Al_2O_3/GO nanocomposite from 1mg/ml to 1.5mg/ml, sensitivity increases to 0.217nm/ppb, which is ~1.85 times higher than the sensitivity observed for 1mg/ml film composition. This higher sensitivity can be attributed to an increase in the number of electronegative sites available for the adsorption of As^{3+} ions, a consequence of the higher Al_2O_3/GO nanocomposite concentration. This, in turn, led to more substantial changes in the refractive index within the vicinity of the gold nanoparticles, resulting in a greater shift in the resonance wavelength of the LSPR. Conversely, when the Al_2O_3/GO nanocomposite concentration was further elevated from 1.5mg/ml to 2mg/ml, sensitivity declines to 0.1833nm/ppb, which is ~1.18 times lower than the sensitivity detected for 1.5mg/ml film composition. This decline is primarily attributed to the increasing thickness of the sensing film as the Al_2O_3/GO nanocomposite concentration in the sensing film increases. For nanocomposite concentration of 2mg/ml, film thickness exceeded the decay length (20-40 nm) of the LSPR [91]. Increased thickness resulted in the hindrance for the As^{3+} ions to penetrate deeper into the sensing film, that is, close to the gold nanoparticles. Consequently, even though there were more electronegative sites available to adsorb arsenic ions in this case, they were no longer effectively involved in the sensing process. Interaction of As^{3+} ions with Al_2O_3/GO nanocomposite beyond the decay length didn't contribute significantly to the sensing process, and hence, didn't significantly impact the resonance wavelength shift. This was the reason for the reduced sensitivity observed in this case. These investigations establish an optimal film configuration for the sensor that corresponds to 1.5mg/ml of Al_2O_3/GO nanocomposite in IPA solution.

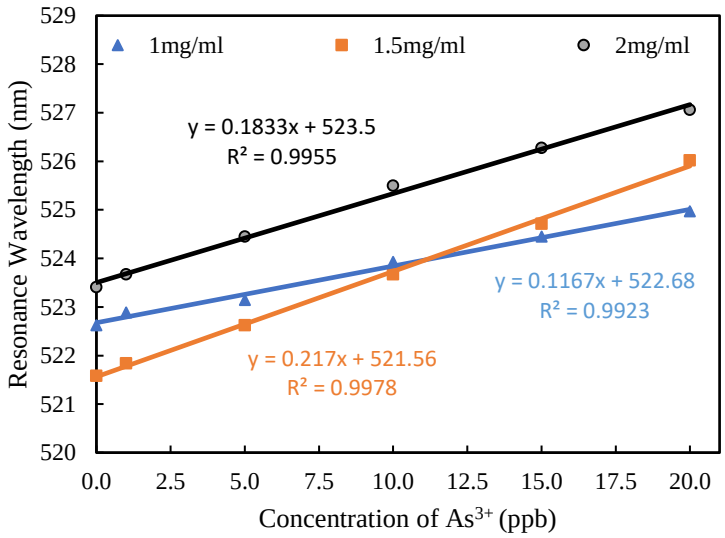

Figure 4.4: Sensor response with different sensing film compositions (1mg/ml, 1.5mg/ml and 2mg/ml concentration of Al_2O_3/GO nanocomposite in IPA).

4.3.2 Limit of detection for the sensor

Apart from sensitivity, the limit of detection (LOD) is another figure of merit, which is critically important while evaluating the performance characteristics of a given sensor. The LOD for the optimized probe is determined to be 0.09 ppb. The LOD of the proposed sensor is significantly lower than the maximum permissible limit for arsenic ions in drinking water set by the WHO (10 ppb). This implies that the proposed LSPR sensor is capable of accurately detecting arsenic ions at concentrations lower than the regulatory threshold, thus making it a promising tool for ensuring the safety of drinking water.

4.3.3 Reusability, Reversibility and Response time of the sensor

As mentioned previously reusability/Repeatability and reversibility are the other crucial parameters for evaluating the performance of a given sensor. To investigate these characteristics, the sensor was tested by exposing it to the minimum (1 ppb) and maximum (20 ppb) As^{3+} ion concentrations. Initially, the sensor was exposed to As^{3+} ion solution of 1ppb concentration within the flow cell, and the corresponding LSPR spectrum was recorded. The sample was left in the flow cell for 1 min and the LSPR spectrum was recorded again. The resonance wavelengths extracted from these two spectra provided insights into the consistency or stability of the sensor. After removing the 1 ppb solution from the flow cell, the sensor was cleaned with deionized water in order to ensure no trace deposition of As^{3+} ion solution onto

the sensor. Sensor was then exposed to As^{3+} ion solution of 20ppb concentration. Corresponding LSPR spectrum was recorded again at an interval of 1 min. To complete one cycle, As^{3+} ion solution of 1ppb concentration was reintroduced into the flow cell after the removal of 20ppb solution and cleaning of the sensor. Corresponding LSPR spectrum was recorded again at an interval of 1 min and compared with the initial measurement. This whole cycle was repeated three times, and the observed response is shown in Fig. 4.5. As can be seen, resonance wavelength remained consistent for each measurement at lower concentration of As^{3+} ion solution in various cycles, indicating no residual As^{3+} ions were left onto the sensor after the removal of solution with higher concentration. The figure illustrates that the sensor produces consistent results during both the forward (1 ppb to 20 ppb) and backward (20 ppb to 1 ppb) change in As^{3+} ion concentration. This establishes the highly repeatable and completely reversible nature of the proposed sensor.

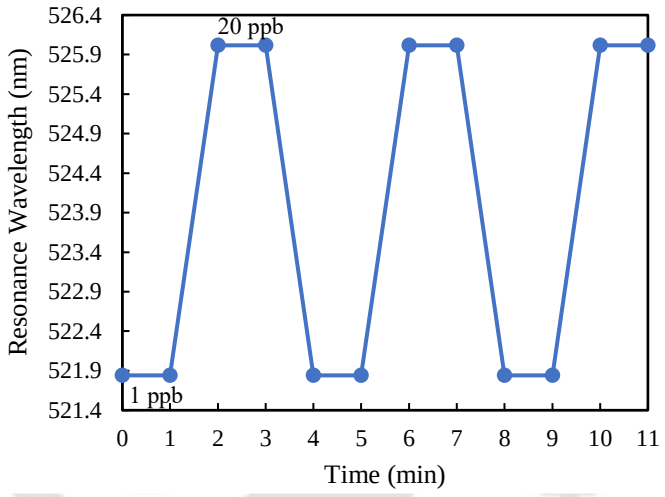

Figure 4.5:Repeatability and reversibility test for the optimized optical fiber LSPR sensor against cyclic variation of As^{3+} ion concentration.

As mentioned earlier the speed of detection is another very critical parameter for evaluating the sensor performance. Achieving a rapid response time holds significant importance for a sensor. To examine the response time of the proposed sensor, the resonance wavelength of the LSPR sensor was measured before and after pouring As^{3+} ion solution of 20ppb concentration into the flow cell. For this, LSPR spectra were recorded after every 0.125 sec, and the corresponding resonance wavelength values were determined. The results of these measurements are presented in Fig. 4.6, where the resonance wavelength values are plotted against time. As can be observed, resonance wavelength is constant before the introduction of As^{3+} solution into the flow cell (sensor being exposed to air). Upon introduction of the As^{3+} ion solution into the flow cell, the resonance wavelength initially exhibits red shifts, and then

gradually stabilizes after approximately 0.5 second. This establishes a response time of 0.5 second for the proposed sensor.

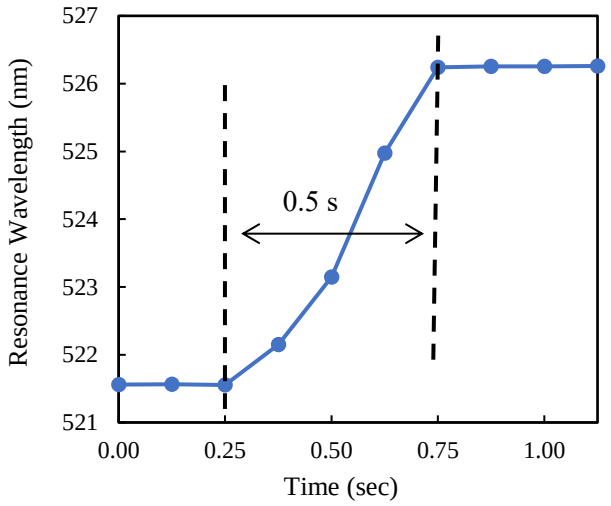

Figure 4.6: Response time (during the variation from air to 20 ppb As^{3+}) for the optimized optical fiber LSPR sensor.

4.3.4 Comparative analysis of the response characteristics

Table 4: Response comparison of the proposed sensor with other As^{3+} ion sensors utilizing different sensing techniques.

Ref.	Sensing Technique	Limit of Detection (ppb)	Response time (s)
[37]	Colorimetric	1.8	-
[100]	Colorimetric	2	240
[101]	Colorimetric	0.53	-
[117]	UV-VIS Spectroscopy	4.5	-
[118]	Fluorescence	27	-
[119]	Electrochemical	46	-
[120]	Electrochemical	5.6	-
[44]	SPR (prism based)	10	30
[45]	SPR (optical fiber based)	0.47	10
[74]	LMR (optical fiber based)	0.99	10
[75]	LSPR (liquid-phase based)	10	-
[76]	LSPR (optical fiber based)	1	-
This work	LSPR (optical fiber based)	0.09	0.5

In order to have a comparative analysis, the limit of detection and the response time of previously reported As^{3+} sensors, employing different sensing schemes, along with that of the

proposed sensor are reported in Table 4. As can be observed from Table 4, proposed sensor brilliantly surpasses all the other sensors employing various sensing schemes, and stands out with its outstandingly low LOD of 0.09 ppb. Observed LOD for the proposed LSPR sensor is ~5.2 times lower than the previously reported lowest LOD in [45]. Additionally, proposed senor exhibits an ultrafast response time of 0.5 s (lowest amongst all the reported sensors), which shows 20 times faster response time than the previously reported fastest response time in [45] and [75].

4.3.5 Selectivity of the sensor

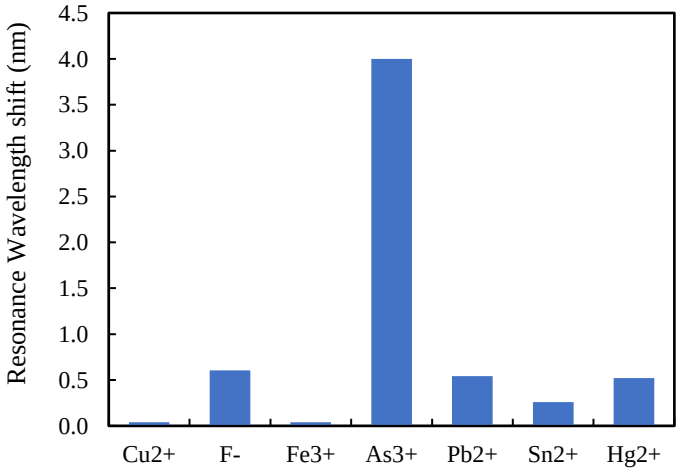

Figure 4.7: Comparison of the resonance wavelength shift of the proposed optical fiber LSPR sensor with different heavy metal ions.

Furthermore, selectivity is another very important parameter as for as the performance characteristics of a sensor is concerned. Hence, selectivity of the proposed sensor is evaluated. For this, experiments were performed by testing the optimized LSPR sensor against various heavy metal ions, such as, Sn^{2+}, Pb^{2+}, Fe^{3+}, F^{-}, Cu^{2+}, and Hg^{2+}, which are commonly found in groundwater. These heavy metal ions can potentially interfere in the detection of As^{3+}. The concentration of each ion was kept constant at 20 ppb. The sensor was immersed in each solution, and the corresponding LSPR spectrum was observed using the same experimental setup, used for detecting arsenic ions. The shift in the resonance wavelength is determined for each heavy metal ions while varying their concentration in the range of 0 to 20 ppb. Fig. 4.7 shows the observed wavelength shifts for each ion. As can be observed from Fig. 4.7, proposed sensor exhibits significantly higher shift in the resonance wavelength for arsenic ions, in comparison to any of the other ions tested in this experiment. This can be attributed to the

surface modification of GO with Al_2O_3 while the formation of nanocomposite, which increases the adsorption capability for As^{3+} ions. Al_2O_3 has a known selective sensitivity towards As^{3+} ions, as established in prior studies [105,106]. Additionally, the larger molecular size of the other heavy metal ions limits their interaction with the sensing layer, resulting in lower sensitivity. Thus, experimental results obtained in this part of study confirm high selectivity of the proposed sensor towards As^{3+} ions, highlighting its potential application in detecting arsenic in real field environment.

4.3.6 Stability and reliability of the sensor

Stability and reliability are other critical parameters for As^{3+} detection. Subsequently, rigorous analysis was carried out to thoroughly examine the short-term and long-term performance of the proposed sensor. To assess the sensor's short-term stability, the LSPR spectrum was recorded continuously at 1-minute intervals for 16 minutes while exposing the sensor to three distinct As^{3+} ion concentrations (1 ppb, 10 ppb, 20 ppb). Results, depicted in Fig. 4.8, conclusively demonstrate high stability in the response characteristics of the proposed sensor. Standard deviations of the resonance wavelength are observed to be ± 0.0098 nm, ± 0.0115 nm, and ± 0.0127 nm at 1 ppb, 10 ppb, and 20 ppb As^{3+} ion concentrations, respectively. Hence, maximum resolution of the sensor for As^{3+} detection is observed to be ± 0.058 ppb, highlighting its exceptional stability and accuracy in As^{3+} detection.

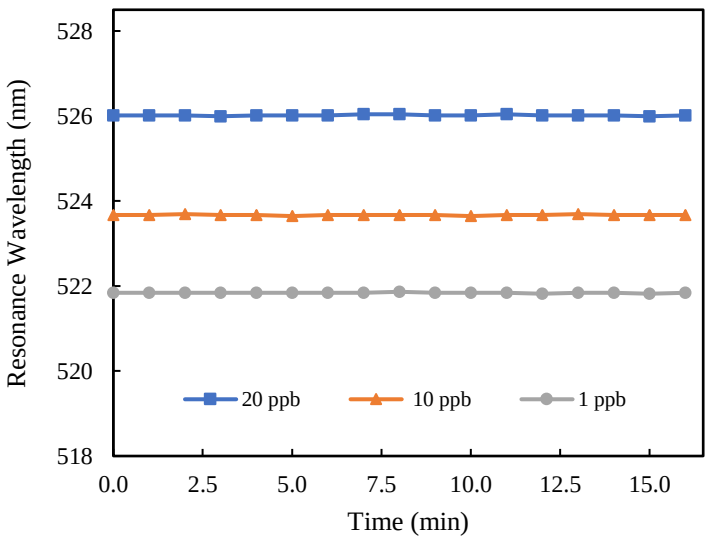

Figure 4.8: Short term stability test: Continuous resonance wavelength for 16 minutes at 20ppb, 10ppb and 1ppb As^{3+} concentration.

For the long-term stability/reliability test, the developed LSPR optical fiber As^{3+} sensor underwent testing on four different days with an interval of 5 days, thus spanning a total of 18 days. Fig. 4.9 displays the proposed optical fiber sensor output corresponding to the three different As^{3+} concentrations (1 ppb, 10 ppb, and 20 ppb), observed over the course of these 18 days. Maximum variation in the resonance wavelength of the developed As^{3+} optical fiber sensor, compared to day one at all the three As^{3+} concentrations, is observed to be less than 0.004%. This underscores the excellent repeatability and reliability of the developed optical fiber As^{3+} sensor.

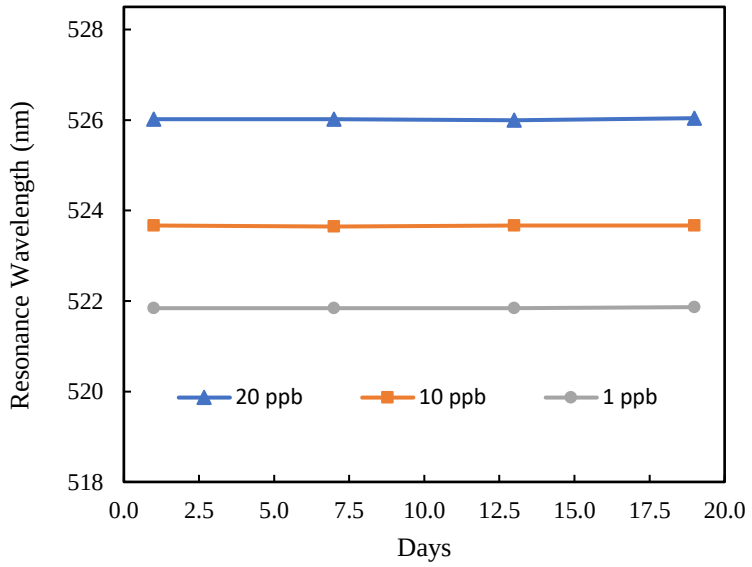

Figure 4.9: Repeatability and reliability test: Resonance wavelength on four different days at 20ppb, 10ppb and 1ppb As^{3+} concentration.

4.3.7 Arsenic detection in real sample and validation of the sensor

To validate the commercial application of the proposed sensor, experiments were carried out using real drinking water samples. Samples were collected from diverse drinking water sources in Guwahati, Assam, India. These water samples included the drinking water within IIT Guwahati, tap water from the neighbouring locality, water from a location near a mill in Guwahati city, samples from the Brahmaputra River taken both from the IIT Guwahati side and the city side. All these water samples were diluted in 5% HNO_3 and no further sample treatment was done. In order to validate the accuracy of As^{3+} ions detection for the proposed optical fiber sensor, a comparison was made between the data obtained from analyzing various real drinking water samples using the proposed optical fiber sensor, and the data obtained using

established method of inductively coupled plasma mass spectrometry (ICPMS). The obtained experimental results, shown in Table 5, demonstrate a close correlation between the concentrations of As^{3+} ions determined by the standard ICPMS (Agilent, 7850) method and those derived from the proposed optical fiber sensor. Additionally, the relative percentage difference (RPD) was also calculated, which is an indicator of the accuracy of the proposed sensor. The smaller the RPD value, the greater is the accuracy of the proposed method in comparison to the established method [93]. As can be observed from Table 5, calculated RPD values from the experimental data are less than 5%. This also indicates a strong agreement between the outcomes of the two methods. These findings strongly support the notion that the proposed optical fiber LSPR sensor serves as a reliable, straightforward, cost effective alternative to conventional techniques like ICPMS for the precise detection of As^{3+} ions.

Table 5: As^{3+} ion concentration from different real water samples using ICPMS analysis and proposed optical fiber sensor.

Real water Sample	Arsenic (As^{3+}) concentration (ICPMS)	Arsenic (As^{3+}) concentration (Optical fiber sensor)	RPD	RPD%
Drinking water	0.98 ppb	0.93 ppb	0.047	4.7
Tap water	1.24 ppb	1.29 ppb	0.043	4.3
Near mill water	20.1 ppb	20.17 ppb	0.003	0.3
Brahmaputra river city side	6.96 ppb	6.94 ppb	0.001	0.1
Brahmaputra river IIT side	4.2 ppb	4.18 ppb	0.004	0.4

4.4 Conclusion

A highly sensitive and selective U-shaped optical fiber arsenic sensor based on LSPR is developed using Al_2O_3/GO nanocomposite as the sensing material. The sensor displays a linear correlation between arsenic ion concentration and the LSPR wavelength shift within the range of 0-20 ppb. Further the proposed sensor is characterized with a sensitivity of 0.217 nm/ppb As^{3+} ion concentration. Additionally, the sensor displays excellent selectivity for arsenic over other heavy metal ions and has a remarkably low limit of detection of 0.09 ppb, which is significantly below the WHO's recommended limit for arsenic in drinking water. Further, the sensor exhibits a very fast response time of 0.5 s. Also, the sensor demonstrates high degree of repeatability, stability, reusability and reliability. Moreover, when the proposed sensor is utilized to detect arsenic in real water samples, its results are observed to be in good

agreement with the standard ICPMS method, validating the accuracy of the proposed sensor. Thus, this sensor presents a reliable, cost effective and straightforward solution for monitoring arsenic in real-world. While the sensor offered high sensitivity, very low LOD and a fast response time, there still exists scope of improving the sensitivity and LOD for detecting As^{3+}. Hence, the next chapter of this thesis aims to develop another novel optical fiber As^{3+} sensor to augment sensitivity and lower the LOD.

Chapter 5 : Novel LSPR based Arsenic Ion Sensor Employing Lauryl Sulphate Functionalized Gold nanoparticles

5.1 Introduction

In order to further enhance the sensing performance for detecting As^{3+} ion, another novel optical fiber sensor is developed using lauryl sulphate functionalized gold nanoparticles. In this case, the gold nanoparticles serve both as the LSPR generator and the sensing material unlike the sensor reported in chapter 4, where a sensing material is coated over the gold nanoparticles coated optical fiber.

Lauryl sulfate-functionalized AuNPs are selected as the sensing material because arsenic ions have a strong affinity for sulfur-containing compounds. This characteristic of arsenic ions has been previously utilized in various colorimetric arsenic ion sensors employing sulfur-based ligands [111], [112]. It is important to mention that lauryl sulphate functionalized gold nanoparticles are used for the first time to realize an optical fiber arsenic sensor to the best of authors' knowledge. A thorough experimental investigation highlights that the functionalization of gold nanoparticles with lauryl sulphate LSPR sensing probe enables the sensor to accurately detect arsenic (As^{3+}) ions, even at extremely low concentrations in the sub-parts per billion range. Most importantly, the proposed sensor exhibits a high sensitivity of 0.3073 nm/ppb As^{3+} ion concentration and a remarkably low limit of detection of 0.06 ppb As^{3+} ion concentration. The sensor also exhibits a very fast response time of 0.5 s. Additionally, the sensor demonstrates high degree of repeatability, stability, reversibility and reliability. The results obtained from this investigation underscore the potential of the proposed sensor as a highly sensitive, selective, rapid and cost-effective arsenic sensor for real-field applications. Furthermore, the proposed sensor is utilized to detect arsenic in real water samples and the results are validated from the standard inductively coupled plasma mass spectrometry (ICPMS) method.

5.2 Experiment

5.2.1 Synthesis of lauryl sulphate functionalized gold nanoparticles

Gold nanoparticles (AuNPs) functionalized with lauryl sulphate (LS) was synthesized by reducing the salts of gold ($HAuCl_4$) with tri-sodium citrate ($Na_3C_6H_5O_7$) [88]. In a flask, 50 ml solution of $AuHCl_4$ (1 mM) was mixed with 0.1 M of LS and stirred for 20 min then heated to

boiling. Following this, 2 ml of $Na_3C_6H_5O_7$ (38.8 mM) was added into the boiling solution, and further heated for approximately 10 minutes. Sodium citrate facilitates in the reduction of Au ions to AuNPs. The color of the solution turned into wine-red, which indicates the formation of AuNPs.

5.2.2 Characterization of lauryl sulphate functionalized gold nanoparticles

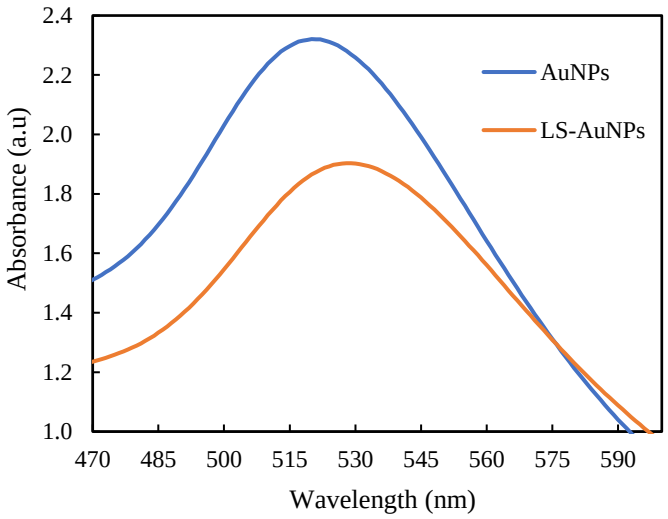

Figure 5.1: UV-Vis Absorbance of AuNPs and LS functionalized AuNPs.

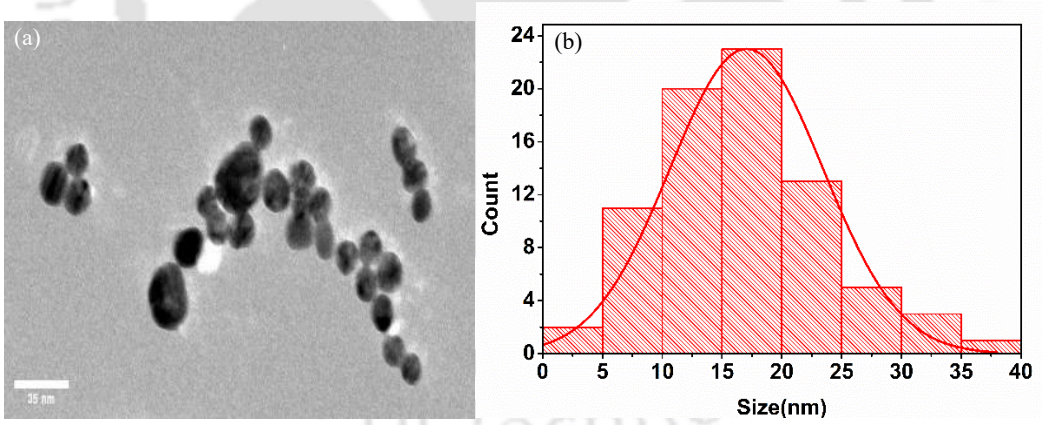

Figure 5.2: FETEM image of LS functionalized AuNPs. (b) Size distribution of the LS functionalized AuNPs.

The absorption characteristics of the synthesized LS-functionalized AuNPs and pure AuNPs were investigated using a UV-visible spectrometer. Fig. 5.1 illustrates the UV-visible spectra for both the synthesized nanoparticles. The results show that pure AuNPs display the characteristic absorption peak at 520 nm, while the LS-functionalized AuNPs display the peak at 529 nm. This observed shift in absorbance from 520 nm to 529 nm indicates successful functionalization of the AuNPs with LS. Moreover, the size of the LS functionalized gold nano

particles was determined using a Field Emission Transmission Electron Microscope (FETEM, JEOL-2100F). Fig. 5.2(a) depicts the typical FETEM image of the proposed LS functionalized AuNPs, whereas, the size distribution of the LS functionalized AuNPs is illustrated in Fig. 5.2(b). As can be observed from the Fig. 5.2(b), diameter of the developed LS functionalized AuNPs is found to be predominantly in the range of 10 – 25 nm, with an average particle size of 18 ± 0.06 nm.

5.2.3 Sensing probe preparation and characterization

A plastic-clad silica (PCS) multimode optical fiber with a core diameter of 600 µm is used to develop the sensor. The total length of 40 cm of the fiber is taken, and both ends were polished to get optically flat end-faces in the transverse section of the fiber. This step is crucial for maximizing power coupling efficiency from the light source to the fiber and from the fiber to the detector. The cladding was removed from the central 2.5 cm section of the fiber. The decladded section was then cleaned with soap solution, de-ionized water, and acetone. Following this, the decladded section was carefully bent into a U-shape by exposing it to a propane flame. Experiments were conducted only on probes that maintained a perfect U-shape and a uniform core diameter in the U-shaped region. The U-shaped probes having a bending radius of 2 mm are employed in this research. In order to attach the LS functionalized AuNPs, the U-shaped section was first soaked in chromic acid for 12 hours, followed by sonication in de-ionized water and drying in an oven. Next, it was immersed in a 5% (v/v) ethanol solution of 3-amino-propyltrimethoxysilane (APTMS) for 3 hours to functionalize the glass surface with amine groups. After rinsing with ethanol and drying in the oven, the probe was dipped in the solution of LS functionalized AuNPs for 2 hours. This resulted in the formation of a film of LS functionalized AuNPs on the decladded fiber surface. Finally, the probe was rinsed with de-ionized water and dried in the oven for 30 minutes. The AuNPs coated U-shaped optical fiber probe is depicted in Fig. 5.3(a). The thickness of the gold nanoparticle coated probe and the surface morphology of the coated region were analyzed using a Field Emission Scanning Electron Microscope (FESEM) (Zeiss, Sigma 300). Fig. 5.3(b) depicts the image of a section of AuNPs coated U-shaped optical fiber. An average diameter in this is observed to be ~600.085 µm, which establishes an average thickness of the AuNPs filam as ~42.5 nm. Fig. 5.3(c) shows the surface morphology of the deposited AuNPs film. The image illustrates not only a high density but also uniform coating of the AuNPs on the decladded fiber surface.

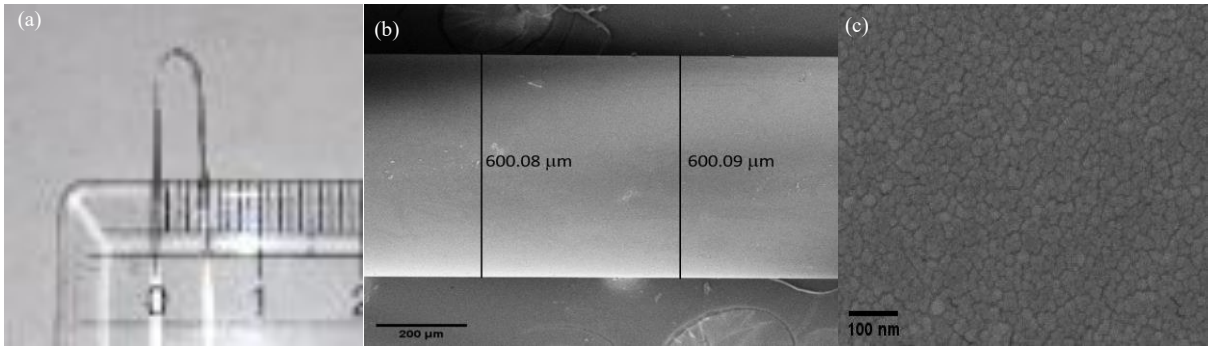

Figure 5.3: (a) AuNPs coated U-shaped probe, (b) FESEM image of the centrally decladded region of the fiber carrying LS functionalized AuNPs coating, (c) FESEM pattern of surface morphology of the LS functionalized AuNPs coated region.

To investigate the response characteristics of the sensor, similar procedures were followed as discussed in Chapter 2. During the experiment As^{3+} concentrations were varied from 0-30 ppb.

5.3 Result and discussion

5.3.1 Response of the proposed LSPR optical fiber sensor towards As^{3+} ions detection

The proposed sensor utilizes the localized surface plasmon resonance technique employing LS functionalized AuNPs as the sensing material, synthesized onto the U-shaped optical fiber probe. LS functionalized gold nanoparticles are coated over the core of the U-shaped sensing region of the optical fiber to induce LSPR. To examine the performance characteristics of the proposed sensor, outputs from the sensor were monitored in real-time while exposing it to solutions with varying concentrations of As^{3+} (0-30 ppb). Fig. 5.4 depicts the resulting LSPR spectra. Notably, the figure reveals a significant red shift in the dip resonance wavelength, accompanied by an increase in transmittance as the concentration of As^{3+} rises. This can be understood as following: when the sensor is exposed to varying concentrations of As^{3+} ions, the As^{3+} ions gets adsorbed onto the electronegative sulphur atoms present on the LS functionalized AuNPs surface. The adsorption of the As^{3+} ions increases the refractive index of the surrounding medium of the gold nanoparticles. This leads to the observed red shift of the resonance wavelength of the LSPR spectrum. To gain deeper insights, the sensor response was analyzed by plotting the dip resonance wavelength corresponding to the applied As^{3+} concentration as shown in Fig. 5.5. As depicted in the figure, the proposed sensor exhibits a linear response within the range of 0-30 ppb As^{3+} concentration, with a high sensitivity of 0.3073 nm/ppb. To determine the effect of functionalization of AuNPs onto the sensor

performance, an optical fiber sensor coated with pure AuNPs sensing film was also characterized for arsenic ion detection. For comparative analysis, the responses of the pure AuNPs coated probe along with the LS functionalized AuNPs coated probe is also plotted in Fig. 5.5. As can be observed from the figure, sensitivity for pure AuNPs is 0.0168 nm/ppb. This shows that the proposed sensor exhibits much higher sensitivity, which is over 18.29 times higher in comparison to the sensitivity observed for pure AuNPs coated optical fiber sensor.

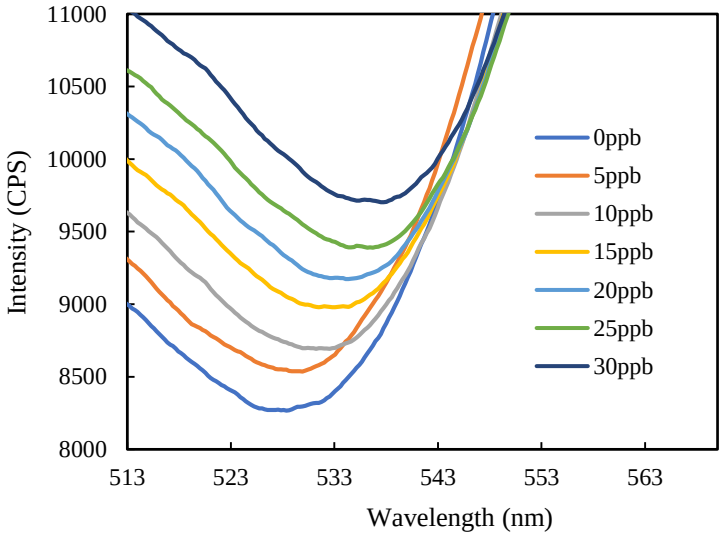

Figure 5.4: Variation of transmittance of the optical fiber with different arsenic ion concentrations.

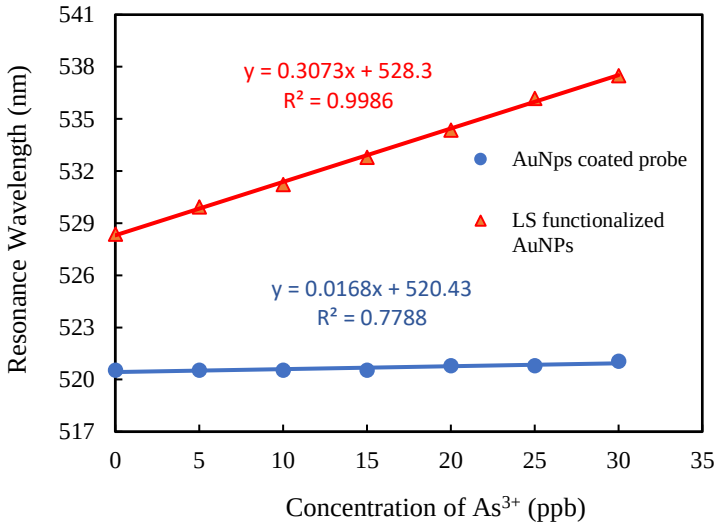

Figure 5.5: Experimentally observed sensor responses of LS functionalized AuNPs coated probe and pure AuNPs coated probes.

This can be understood as following: when the concentration of As^{3+} ion is varied within the range of 0–30 ppb, there is negligible change in the refractive index of the solution. As a result,

the pure AuNPs coated probe exhibit only a negligible shift in their resonance wavelength when exposed to these varying concentrations of As^{3+} ions. In contrast, when the LS-functionalized AuNP sensing probe is exposed to varying concentrations of As^{3+} ions, a different behaviour is observed. While the refractive index of the surrounding medium remains largely unchanged; however, the high binding affinity of the electronegative sulfur atoms in lauryl sulfate for the electropositive As^{3+} ions facilitates the adsorption of As^{3+} ions onto the surface of the LS-functionalized AuNP film. This adsorption significantly increases the local refractive index around the AuNPs, leading to a pronounced red shift in the resonance wavelength of the LSPR spectrum compared to that observed in pure or non-functionalized AuNPs coated probe.

5.3.2 Limit of detection for the sensor

As discussed earlier, the limit of detection (LOD) is another critical figure of merit when evaluating the performance characteristics of a sensor. The LOD for the optimized sensor is observed to be 0.06 ppb. This achieved LOD is significantly lower (~166.66 times) than the maximum permissible limit set by WHO for arsenic ions in drinking water (10 ppb). This indicates that the proposed LSPR sensor can detect arsenic ions at concentrations well below the regulatory threshold, making it a highly promising tool for ensuring the safety of drinking water.

5.3.3 Reusability, reversibility and response time of the sensor

Repeatability/reusability and reversibility are other important parameters in evaluating the performance of the sensor. To determine these characteristics, the sensor was tested by exposing it to the minimum (5 ppb) and maximum (30 ppb) concentrations of As^{3+} ions. Initially, the sensor was exposed to a 5 ppb As^{3+} ion solution in the flow cell, and the corresponding LSPR spectrum was recorded. The solution was kept in the flow cell for 1 minute and the LSPR spectrum was recorded again. After removing the 5 ppb solution from the flow cell, the sensor was thoroughly cleaned with deionized water to ensure no trace of As^{3+} ions remained onto the sensor. The sensor was then exposed to a 30 ppb As^{3+} ion solution, and the LSPR spectrum was recorded again at an interval of 1 min, completing one cycle of evaluation. To test repeatability, the 5 ppb solution was reintroduced into the flow cell, and the results were compared to the initial measurements. This entire cycle was repeated multiple times, typical response of the sensor for 3 cycles is presented in Fig. 5.6(a). As can be observed

from the figure, the resonance wavelength remained consistent for each measurement at the lower concentration of the As^{3+} ion solution in various cycles. This indicates that no residual

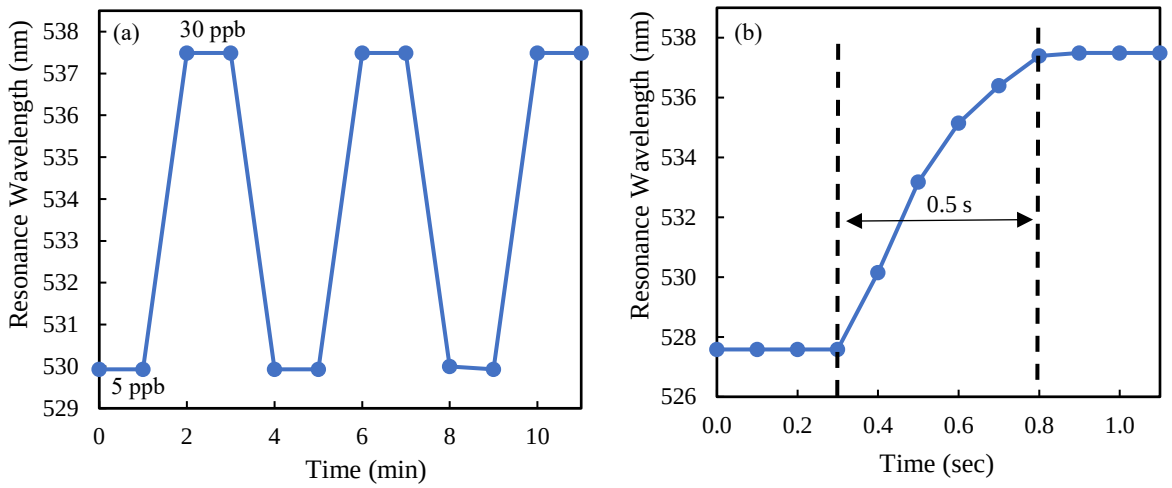

Figure 5.6: (a) Repeatability and reversibility test for the proposed optical fiber LSPR sensor against cyclic variation of As^{3+} ion concentration. (b) Response time (during the variation from air to 30 ppb As^{3+}) for the proposed optical fiber LSPR sensor.

As^{3+} ions were left onto the sensor after the higher concentration of As^{3+} ion solution was removed. The figure demonstrates that the sensor produces consistent results during both the forward (5 ppb to 30 ppb) and backward (30 ppb to 5 ppb) change in As^{3+} ion concentration. This confirms the highly repeatable and fully reversible nature of the proposed sensor.

The speed of detection is another crucial parameter for evaluating the sensor performance. Achieving a fast response time being significantly important for a sensor. To determine the response time of the proposed sensor, the resonance wavelength of the LSPR sensor was measured before and after introducing a 30 ppb As^{3+} ion solution into the flow cell. LSPR spectra were recorded after every 0.1 sec, and the corresponding resonance wavelength values were determined. The results of these measurements are shown in Fig. 5.6(b), where the resonance wavelength values are plotted against time. From the figure it can be observed that before the As^{3+} solution was introduced, the resonance wavelength remained constant as the sensor was exposed to air. Once the As^{3+} ion solution entered the flow cell, the resonance wavelength exhibited an initial red shift, gradually stabilizing after about 0.5 sec. This establishes a response time of 0.5 seconds for the proposed sensor, demonstrating its rapid detection capability.

5.3.4 Selectivity of the sensor

Selectivity of the proposed sensor is evaluated, which is another very important parameter of a sensor performance. The selectivity of the sensor was evaluated by testing it with various heavy metal ions, commonly found in groundwater such as Sn^{2+}, Cu^{2+}, F^{-}, Fe^{3+}, Hg^{2+}, Pb^{2+}, Cd^{2+}, Mg^{2+}, Ni^{2+}, Co^{2+}, and Zn^{2+}. These heavy metal ions could potentially interfere in the detection of As^{3+}. The concentration of each ion was kept constant at 10 ppm, except for As^{3+} which was tested at a very lower concentration (~333.4 times) of 30 ppb. The sensor probe was immersed in each solution, and the corresponding LSPR spectrum was observed using the same experimental setup used for detecting arsenic ions. The shift in the resonance wavelength is determined for the change in the concentration of each heavy metal ions from 0 to 10 ppm. As demonstrated in Fig. 5.7, the sensor exhibited a significantly higher shift in the resonance wavelength corresponding to arsenic ions compared to any of the other ions tested even at a lower concentration as low as 30 ppb. This can be attributed to the surface modification of AuNPs with LS, which increases its adsorption capability for As^{3+} ions. This observation confirms the sensor's high selectivity towards As^{3+} ions, highlighting its potential application in detecting arsenic in real field.

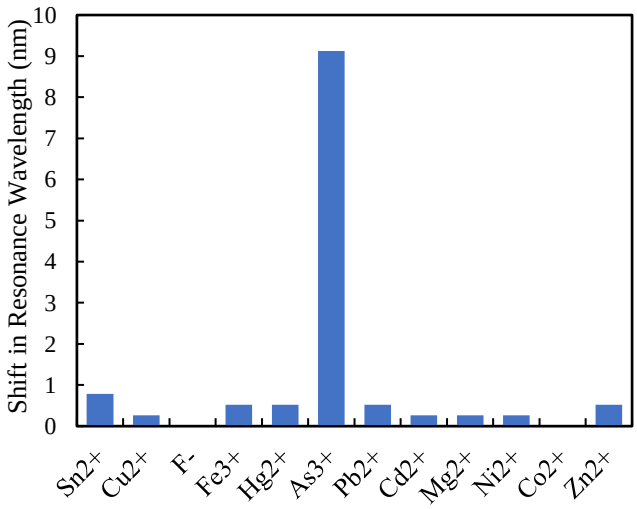

Figure 5.7: Comparison of the resonance wavelength shift of the proposed optical fiber LSPR sensor with different heavy metal ions.

5.3.5 Stability and reliability of the sensor

Stability and reliability are other essential parameters for effective As^{3+} detection. To thoroughly examine these aspects, the proposed sensor underwent comprehensive short-term

and long-term performance testing. To examine the sensor's short-term stability, the LSPR spectrum was recorded continuously at every minute for 16 minutes at three different As^{3+} ion concentrations (5 ppb, 15 ppb, and 30 ppb) separately. The observed results are shown in Fig. 5.8. The standard deviations of the resonance wavelength measured to be ±0.0180 nm, ±0.0166 nm, and ±0.0194 nm for 5 ppb, 15 ppb, and 30 ppb concentrations, respectively. Therefore, maximum resolution of the sensor for As^{3+} detection is observed to be ±0.063 ppb, confirming the sensor's high stability and accuracy in detecting As^{3+} ions.

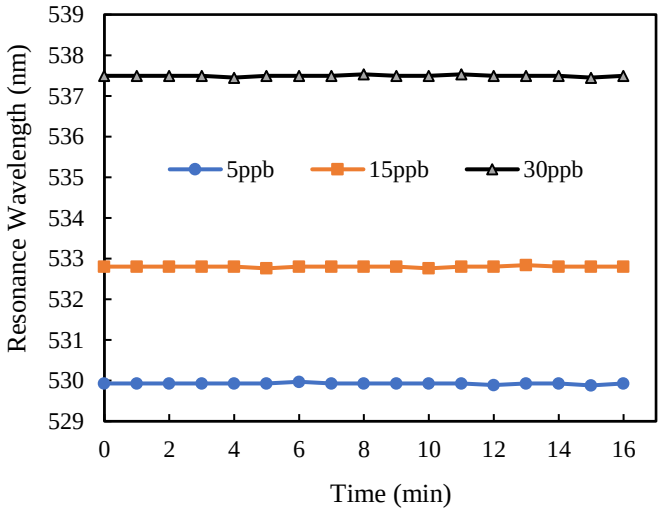

Figure 5.8: Short term stability test: Continuous resonance wavelength for 16 minutes at 5ppb, 15ppb and 30ppb As^{3+} concentration.

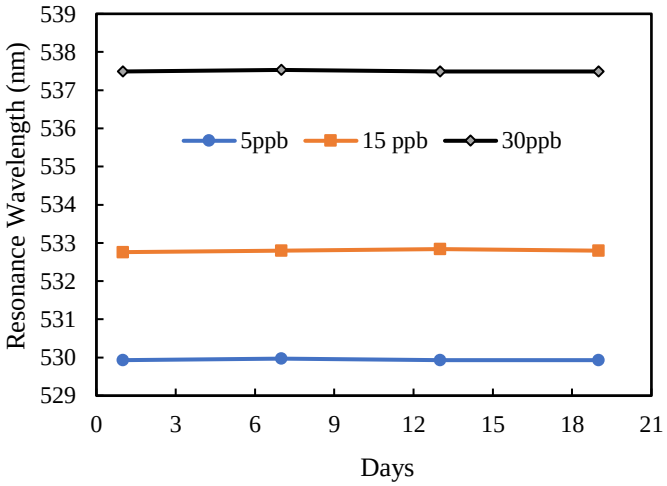

Figure 5.9: Repeatability and reliability test: Resonance wavelength on four different days at 5ppb, 15ppb and 30ppb As^{3+} concentration.

For long-term stability or reliability test, the developed optical fiber As^{3+} ion sensor underwent testing on four different days with an interval of 5 days at three different As^{3+} concentrations

(5 ppb, 15 ppb, and 30 ppb) in a span of 18 days. The observed results are shown in Fig. 5.9. Notably, it can be observed from the figure that the maximum variation in the resonance wavelength of the developed As^{3+} optical fiber sensor is less than 0.006% of the resonance wavelength recorded on the first day. This result highlights the excellent repeatability and reliability of the developed optical fiber As^{3+} sensor.

5.3.6 Detection of Arsenic ion in real sample and validation of the sensor

Table 6: As^{3+} ion concentration from different real water samples using ICPMS analysis and proposed optical fiber sensor.

Real water Sample	Arsenic (As^{3+}) concentration ICPMS	Arsenic (As^{3+}) concentration optical fiber sensor	RPD	RPD%
Drinking water	0.98 ppb	0.97 ppb	0.003	0.34
Tap water	1.24 ppb	1.18 ppb	0.047	4.77
Near mill water	20.1 ppb	20.15 ppb	0.002	0.26
Brahmaputra river city side	6.96 ppb	6.91 ppb	0.006	0.60
Brahmaputra river IIT side	4.2 ppb	4.20 ppb	0.005	0.05

To evaluate the commercial applicability of the proposed sensor, experiments were conducted using real drinking water samples. Water samples were collected from various drinking water sources in Guwahati, Assam, India. These included water samples from drinking water within Indian Institute of Technology (IIT) Guwahati, tap water from the neighboring locality, water from a location near a mill in Guwahati city, samples from the Brahmaputra River taken both from the IIT Guwahati side and the city side. In order to verify the accuracy of As^{3+} ion detection by the proposed optical fiber sensor, results obtained from analyzing various real drinking water samples using the proposed optical fiber sensor were compared with the data obtained using the established inductively coupled plasma mass spectrometry (ICPMS) method. Prior to analysing the real water samples, they were diluted with 5% HNO_3, a necessary preparation step for ICPMS analysis. This dilution ensures the stability of the samples during the measurement process. After this step no further water treatment was done. The experimental results, presented in Table 6, show a strong correlation between the $As3^{+}$ concentrations measured by the standard ICPMS (Agilent, 7850) method and those detected by the proposed optical fiber sensor. Additionally, the relative percentage difference (RPD) was also calculated, which is an accuracy measure of the proposed sensor. The smaller the RPD

value, the greater is the accuracy of the proposed method in comparison to the established method [93]. As can be observed from Table 6, calculated RPD values are under 5%, demonstrating close agreement between the outcomes of the two methods. These findings strongly validate the proposed optical fiber LSPR sensor as a reliable, straightforward, and cost-effective alternative to conventional methods like ICPMS for detecting As^{3+} ions in real field.

5.4 Conclusion

A highly sensitive and selective U-shaped optical fiber arsenic ion sensor based on LSPR is developed employing lauryl sulfate-functionalized gold nanoparticles as the sensing material. The sensor demonstrates a linear relationship between arsenic ion concentration and LSPR wavelength shift in the 0-30 ppb range, with a high sensitivity of 0.3073 nm/ppb for As^{3+} ions. It shows excellent selectivity for arsenic over other heavy metals and achieves a remarkably low detection limit of 0.06 ppb, which is significantly below the WHO's recommended limit for arsenic ion in drinking water. Additionally, the sensor responds rapidly, with a fast response time of 0.5 sec. Moreover, the sensor exhibits high degree of repeatability, stability, reusability, and reliability. Further, when the sensor is tested with real water samples, the results closely align with those from the standard ICPMS method, confirming its accuracy. Moreover, it is evident that, the reported sensor achieves an enhanced sensitivity, an even lower LOD (1.5 times) while maintaining the same response time, high selectivity, stability, repeatability and reliability in comparison to the sensor reported in chapter 4. Thus, this sensor offers a reliable, cost-effective, and straightforward approach to arsenic ion monitoring in real field applications.

Chapter 6 : Novel Optical Fiber Sensor for Explosive (Trinitrophenol) Detection

6.1 Introduction

Detecting explosives accurately has emerged as a critical concern given the escalating instances of explosive deployment in terrorist activities. The constituents of many industrial explosives predominantly include nitroexplosives like 1,3,5-Trinitro1,3,5-triazinane (RDX), 2,4,6-Trinitrotoluene (TNT), and compounds such as Trinitrophenol (TNP), also recognized as picric acid (PA), 2,4-Dinitroanisole, 2,4- Dinitrotoluene (DNT), and 4-Nitrotoluene (NT). Among these, TNP stands out as one of the most powerful explosives and is extensively used in landmines over several decades. TNP is a very powerful explosive, even stronger than TNT [46]. Furthermore, TNP is highly soluble in water, and extremely toxic, even at trace concentrations. Its high solubility poses a serious threat to soil and groundwater, increasing the risk of human exposure through indirect means. Such exposure can result in health issues like cyanosis, anemia, cancer, and eye and skin irritation [47]. Despite these adverse effects, TNP continues to be used in various industries, such as pharmaceuticals, leather, and dye industries. Regulatory standards like the "surface water environmental quality standards" (GB3838-2002) have set a strict maximum allowable TNP concentration in water at 0.5 mg/L (ppm) [113], highlighting the importance of precise detection methods for TNP in aqueous environments. Effective strategies for detecting trace amounts of TNP are vital for environmental safety and security, particularly in identifying unexploded landmines. The development of highly selective sensors capable of detecting TNP at low concentrations is crucial for safeguarding both environmental and public health. However, selectively detecting TNP remains a significant challenge due to its electron-deficient nature, which it shares with other nitro explosives and phenolic contaminants. Therefore, there is an alarming need for developing efficient, selective sensors for TNP detection in water.

Various analytical techniques exist for analyzing nitro explosives such as TNP, including high-performance liquid chromatography [49], surface enhance Raman spectroscopy [50], mass spectrometry [51], Raman scattering [52], colorimetry [53], [54] and electrochemical analysis [55]–[57] etc. These techniques are highly accurate. However, they have drawbacks such as they are complex, expensive, less sensitive, time-consuming, and require skilled personnel, which limits their widespread use. In contrast, fluorescent probes have emerged as a promising alternative for nitro explosive detection due to their simplicity, rapid response,

portability, easy sample preparation and high sensitivity. Therefore, this field has caught the attention of researchers and hence several fluorescent sensors for TNP have been reported. For example, as discussed in Chapter 1 from references [48 – 63]. Nevertheless, these fluorescent probes do have limitations, including fluorescence quenching in response to TNP which inturn makes them non-reusable, selectivity issues, and challenges in on-site detection applications. The primary unresolved challenge in this field is the remote detection of trace amounts of explosives, such as landmines, which remains exceptionally difficult. To address this challenge, optical fiber sensors have emerged as a promising alternative for explosive detection. These sensors offer advantages such as high sensitivity, remote sensing capability, immunity to electromagnetic interference, multiplexing, real-time detection, ease of use, cost-effectiveness, and suitability for field applications. Only two optical fiber based fluorescence TNP sensors are reported so far. For instance, as discussed in Chapter 1 from references [77, 78]. Nevertheless, these sensors did not show reusability and also there is a very high scope of improving the detection limit further. So, there is a significant need for developing an optical fiber sensor that is simple, exhibits a very low detection limit, high selectivity, optimal sensitivity, reusability, and fast response and recovery time for real-field applications.

The main objective of the research reported in this chapter, is to develop an optical fiber TNP sensor with high sensitivity, very low limit of detection, highly selective and fast response and recovery times by employing simplest optical fiber sensing configuration. To achieve this, the sensor employs a novel polymer, PFTPA film, as a sensing cladding over the centrally decladded region of a straight and uniform plastic-clad silica (PCS) multimode optical fiber. Proposed sensor exploits intensity modulation through evanescent wave absorption – one of the simplest techniques for developing optical fiber TNP sensor. For the first time in the best of author's knowledge an optical fiber TNP sensor employing evanescent wave-based intensity modulation scheme is reported. Rigorous experimental investigations are carried out to establish the response characteristics of the proposed sensor. The sensor exhibits a linear response in the range of 0-50 parts per billion (ppb) with a remarkable limit of detection (LOD) of 1.06 ppb. Even after testing the sensor for over 18 days, the sensing characteristics remained unchanged. This demonstrates the stability and reliability of the proposed optical fiber sensor, which has the potential to be utilized in various applications that require accurate and precise TNP detection. The sensor also shows high selectivity towards TNP. These significant findings underscore the sensor's potential as an efficient, user-friendly, and cost-effective solution for

real-world TNP detection, particularly in aqueous environments. In summary, the proposed optical fiber sensor provides a direct and simple approach to TNP detection, contributing to the critical need for reliable counterterrorism measures and addressing environmental health concerns.

6.2 Experiment

6.2.1 Synthesis of the polymer (PFTPA)

A novel polymer, named PFTPA, was successfully derived from the monomer FTPA (F indicates Fluorene and TPA indicates Triphenyl amine) through Stille coupling reaction with a yield of 70%. For that three monomers: FTPA (50 mg, 0.076 mmole), 2,5-bis (trimethylstannyl) thiophene (62 mg, 0.152 mmole), and FMI (F indicates Fluorene and MI indicates Methyl imidazole) (62 mg, 0.076 mmole) were combined in a Schlenk tube equipped with a condenser and an argon inlet. Then the mixture was made inert by degassing and purging with Argon. Subsequently, 5 mg of the catalyst Tetrakis (triphenylphosphine) palladium ($Pd(PPh_3)_4$) was added in inert condition. A solution containing a mixture of Dimethylformamide (DMF) and Toluene in a 1:3 ratio was introduced into the reaction mixture. The resulting solution was stirred at a temperature of 110°C for a duration of 30h while maintaining the inert condition. Thereafter, the mixture was cooled down to room temperature and the final product was extracted with Chloroform ($CHCl_3$) and water. The organic layer was subsequently dried and underwent further purification through repeated precipitation in ether and methanol. Upon completion of the purification process, 100 mg of the polymer PFTPA was obtained with a yield of 70%. The resulting polymer exhibited a reddish-brown color as shown in Fig. 6.1(a), and the inset of Fig. 6.1(a) shows the structure of the polymer. Also, the FETEM picture of prepared Polymer PFTPA is taken using Zeiss (Sigma) as shown in Fig. 6.1(b). The FETEM image depicts the formation of large polymer PFTPA sheets resulting from the crosslinking of monomers, forming elongated chains, with dimensions typically ranging in the magnitude of a few microns.

6.2.2 Sensing probe preparation and characterization

To develop the TNP sensor, a plastic cladding silica (PCS) fiber measuring 40 cm in length and 200µm in core diameter was utilized. To ensure optimal performance, the fiber ends were carefully prepared to be optically flat and perpendicular to the fiber axis. Next, a 3 cm section

in the middle of the fiber was decladded, and this exposed section was precisely cleaned using soap solution, followed by rinsing with de-ionized water, and finally, cleaning with acetone to ensure a pristine surface. In order to explore the impact of the sensing film composition on the sensor performance, the concentration of polymer PFTPA is varied in the order of 0.5mg/ml, 1mg/ml and 1.3mg/ml in Tetrahydrofuran (THF), a commonly used solvent. Subsequently, a smooth solution was prepared for each concentration. This solution was carefully coated onto the decladded portion of the fiber using the dip coating method, where the fiber was dipped into the solution and then slowly withdrawn at a predetermined speed to achieve an even and uniform coating thickness. In order to investigate the effect of sensing film thickness on the sensor performance, multiple dip coating (1-dip, 2-dip, 3-dip and 4-dip) was employed to vary the thicknesses of the sensing film for each film composition.

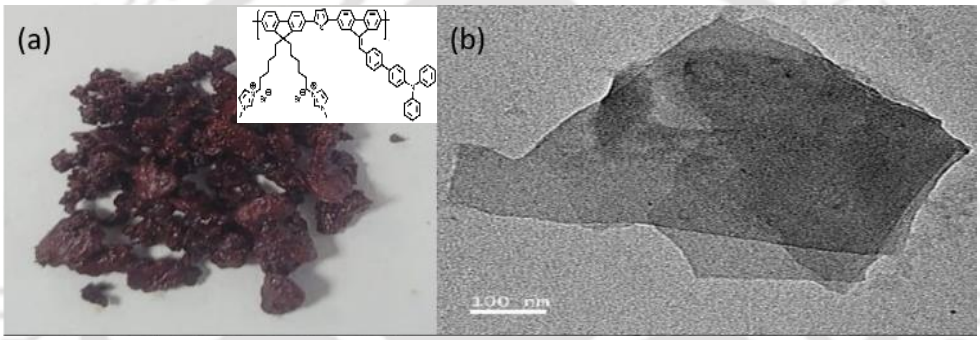

Figure 6.1: (a) Polymer PFTPA, (b) FETEM picture of polymer PFTPA.

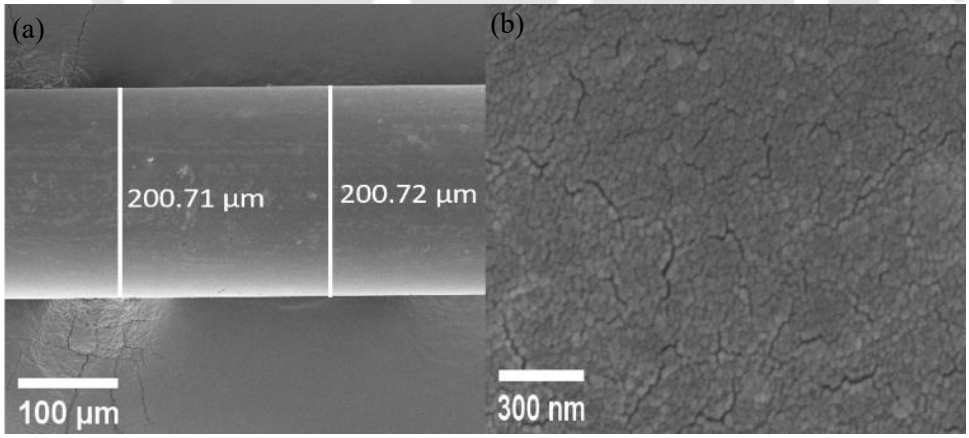

Figure 6.2: (a) FESEM picture of 3-dip coated fiber and (b) Surface of the coated fiber.

Following the coating process, all of the coated fiber probes were left to dry naturally at room temperature for a duration of two days. This drying period allowed the solvent to evaporate gradually, leaving behind a solid and stable sensing layer adhered to the fiber surface. Surface morphology and the thickness of deposited film were examined by Field Emission Scanning

Electron Microscope (FESEM) (Zeiss, Sigma 300). Fig. 6.2(a) depicts, as an example, image of the 3-dip coated sensing region corresponding to film composition 1mg/ml of polymer PFTPA in THF of the optical fiber. Average diameter in this region is observed to be ~ 200.715 µm, which establishes an average thickness of the sensing film as ~ 357.2 nm. Surface morphology of the deposited sensing film for this probe is depicted in Fig. 6.2(b), which shows a good degree of uniformity of the polymer PFTPA coated over the fiber. Similarly, the measured film thicknesses for other dip coatings are ~ 119.17 nm for 1-dip, ~ 239 nm for 2-dip, and ~ 477 nm for 4-dip coating.

In order to investigate the sensor's response characteristics, extensive experiments were carried out. For this, the developed optical fiber sensor was fixed within an in-house developed flow cell in such a way that the sensing region remained at the center of the flow cell, as shown in Fig. 6.3. Optical output from a UV laser source operating at wavelength 390.26 nm was coupled to the optical fiber sensor from one end. Whereas the distal end of the fiber was connected to a photodetector using subminiature version A (SMA) connector. The photodetector is then interfaced with a computer through data acquisition (DAQ) card and MATLAB program for real-time monitoring of the fiber sensor's output. Aqueous TNP solutions of varying concentrations, ranging from 0 ppb to 50 ppb, were prepared. To characterize the optical fiber sensor, the output intensity of the sensor was monitored while exposing it to a TNP solution of fixed concentration. Output intensity data were recorded during sufficient time in order to let the sensor's output getting stabilized. Afterwards, TNP solution was removed, sensor was properly cleaned ensuring no trace deposition of the TNP solution onto the sensor. Sensor was then exposed to the TNP solution of higher concentration. Throughout the experiment, temperature was kept constant at 25ºC.

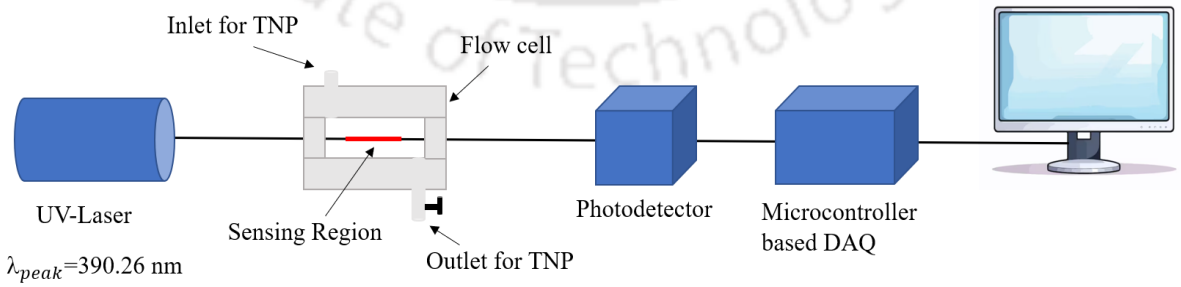

Figure 6.3: Schematic diagram of the experimental set-up for the characterization of optical fiber TNP sensor.

6.3 Result and discussion

6.3.1 Response of the proposed optical fiber sensor towards TNP detection

The proposed sensor exploits intensity variation modulation through evanescent wave interaction with the thin sensing film of polymer PFTPA in the cladding of the fiber. The sensor employs the simplest and easiest sensing configuration where the sensing film is synthesized onto the centrally decladded region of the straight and uniform PCS optical fiber. To precisely assess the effect of film configuration on the sensor performance optimization, a thorough examination of sensor characteristics by varying the film composition as well as the thickness of the film were conducted. To do so, composition of the sensing film was varied specifically at concentrations 0.5 mg/ml, 1mg/ml and 1.3 mg/ml of polymer PFTPA in THF, and the thickness of the film was varied by applying 1-dip, 2-dip, 3-dip, and 4-dip coatings successively for each composition. It is important to note that the concentration of polymer PFTPA in THF could not be increased beyond 1.3 mg/ml due to solubility constraints. The complex structure of polymer PFTPA, featuring long chains and a high degree of crosslinking, hindered solvent (THF) molecules from effectively integrating individual polymer units into the solution beyond this threshold. It is well-established that the dissolution of polymers relies not only on their physical properties but also on their chemical structure, encompassing factors such as polarity, molecular weight, branching, and crystallinity. In order to investigate the response characteristics of the proposed sensor, various aqueous solutions of TNP with different concentrations ranging from 0-50ppb were prepared. The corresponding optical fiber output intensity was recorded while exposing the sensor to varying TNP concentration solutions. The response characteristics for all the sensors with varying film thicknesses for each varying film composition were studied. For example, in case of film composition 1mg/ml the thickness is varied by multiple dip coatings. It's worth noting that since the films in each case were prepared from the same solution composition, any disparities in sensitivity should be attributed solely to differences in film thickness. To explicitly observe this effect, the response characteristics of the sensing probe was determined by plotting the fiber sensor output intensity against varying concentrations of TNP for each probe. Fig. 6.4 depicts the effect of varying film thickness for the film composition of 1mg/ml polymer PFTPA in THF concentration, while increasing the TNP concentration from 0-50 ppb. Similar responses were observed while decreasing the TNP concentration. The results indicate that the fiber sensors output intensity decreases as concentration of TNP increases in each case. The phenomenon can be explained as follows:

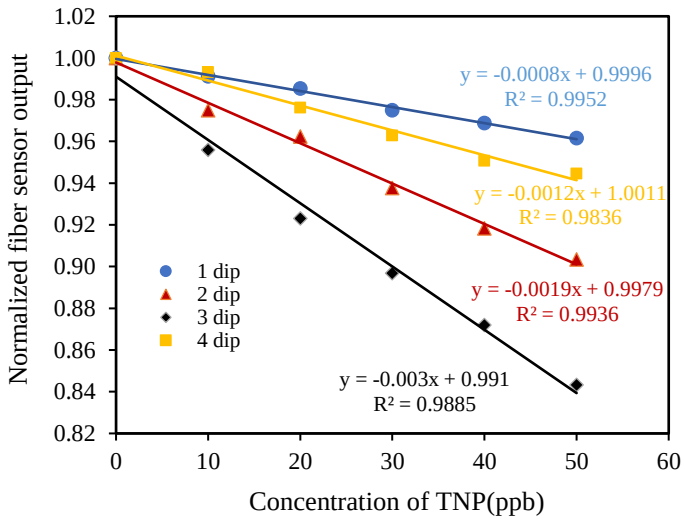

Figure 6.4: Experimentally observed sensor response corresponding to film composition 1mg/ml with different film thicknesses (1-dip, 2-dip, 3-dip and 4-dip).

The sensing film (PFTPA) contains a positively charged receptor that interacts with negatively charged TNP molecules. Consequently, an increase in the concentration of TNP leads to enhanced adsorption of TNP molecules onto the receptor film. This, in turn, causes the refractive index of the cladding in the sensing region to increase. As a result, the guided power leaks to the cladding modes, leading to a corresponding intensity modulation. All sensors with different film thicknesses exhibited a linear response within the 0-50 ppb TNP concentration range. The 1-dip coated sensor shows a sensitivity of 0.0008/ppb TNP concentration. Increasing the film thickness from 1-dip to 2-dip enhances the sensitivity to 0.0019/ppb TNP concentration, representing ~2.37 times increase compared to the one-dip coated sensor. Moreover, increasing the thickness from 2-dip to 3 dip enhances the sensitivity to 0.0032/ppb TNP concentration, about 1.57 times higher than the sensitivity of the two-dip coated sensor. However, extending the thickness from 3-dip to 4-dip does not follow this trend. As the film thickness goes from 3 to 4-dip, the sensor's sensitivity no longer improves and instead decreases to ~0.0012/ppb TNP concentration. Thus, the 3-dip coated sensor exhibits the highest sensitivity. This confirms the existence of an optimum film thickness for the 3-dip coated sensor. The following reasons can be attributed to the observation of optimum film thickness. In the case of 1-dip and 2-dip coatings, the film thicknesses were notably smaller than the penetration depth of the evanescent wave, which is typically of the order of the wavelength of the light source, approximately ~390.26 nm in this scenario. Consequently, there were fewer positively charged receptors available on the sensing cladding comprising polymer PFTPA, to interact with TNP molecules. As the TNP concentration increased, negatively charged TNP

molecules could only interact with a limited number of receptors. Thus, the adsorption of TNP molecules onto the receptor film was limited. This resulted in restricted absorption of the optical power carried by the evanescent field in the sensing region, leading to a lower sensitivity. The thickness of the sensing film in the 3-dip coated probe increased significantly but remained slightly lower than the penetration depth. The increased thickness accommodated more receptors and hence, more TNP molecules that are adsorbed onto the receptors within the sensing film, filling up to the entire width of the evanescent wave. This facilitates optimum exploitation of the optical power available in the evanescent field, and hence, optimum optical absorption in this case, leading to a higher sensitivity compared to 1-dip as well as 2-dip coated probes. The thickness of the sensing film corresponding to 4-dip coated probe was greater than the penetration depth of the evanescent wave. Increased thickness resulted in the hindrance for the TNP molecules to penetrate deeper into the sensing PFTPA film, that is close to the core-sensing-clad interface. Thus, TNP molecules that are adsorbed onto the receptors were limited within the range of (or, volume of the sensing film spanned by) the evanescent wave. This resulted in the reduced absorption of the optical power carried by the evanescent field in the sensing region, and hence, substantially lesser sensitivity. Therefore, an optimum film thickness of 3-dip is observed for the film composition of 1mg/ml polymer PFTPA in THF. Likewise, the impact of film thickness on the sensor's performance was investigated for the other two film compositions (0.5 mg/ml and 1.3 mg/ml polymer PFTPA in THF) as well. In all the cases, the 3-dip coated sensor exhibited the best response characteristics, regardless of the film composition

Furthermore, to observe the sensor response with varying film composition, the sensor responses corresponding to 3-dip coating of all three film compositions were plotted in Fig.6.5. From the figure it can be observed that all the sensors corresponding to different film composition shows a linear response in the range of 0-50 ppb TNP concentration. The sensor with film composition of 0.5 mg/ml of polymer PFTPA in THF show a sensitivity of 0.0014/ppb TNP concentration. Increasing the polymer PFTPA concentration in THF from 0.5mg/ml to 1mg/ml enhances the sensitivity to 0.0030/ppb TNP concentration, which is ~2.14 times higher than the sensitivity of the sensor with film composition of 0.5mg/ml. Further increasing the polymer PFTPA concentration in THF from 1 mg/ml to 1.3 mg/ml increases the sensitivity to 0.0032/ppb TNP concentration, which is ~1.06 times higher than the sensitivity of the sensor with film composition of 1 mg/ml. The increase in sensitivity with the rise in polymer PFTPA

concentration in THF can be attributed to the greater amount of polymer PFTPA in the sensing film, resulting in more receptors available to interact with TNP molecules. This induces a more significant change in the refractive index of the cladding in the sensing region, leading to increased leakage of the guided power to the cladding modes. Consequently, there is a higher modulation in the output intensity of the optical fiber. Therefore, the film thickness corresponding to the three-dip coated probe for 1.3 mg/ml concentration of polymer PFTPA in THF (concentration cannot be increased further due to solubility issue of the polymer PFTPA), which is approximately equal to the penetration depth, represents the optimum film composition. This condition results in maximum evanescent wave interaction, leading to maximum sensitivity.

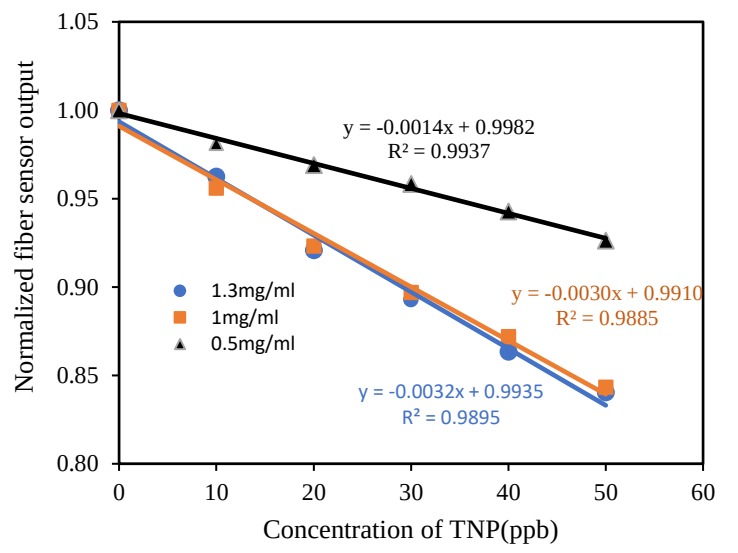

Figure 6.5: Experimentally observed sensor response corresponding to 3-dip coating with different film compositions (0.5mg/ml, 1mg/ml, and 1.3mg/ml).

6.3.2 Limit of detection of the sensor

Apart from sensitivity, the performance of the sensor is also evaluated based on its ability to detect the minimum analyte concentration, known as the limit of detection (LOD). It was calculated the way discussed in chapter 2. The LOD for the optical fiber sensor with optimized configuration is determined to be 1.06 ppb.

6.3.3 Repeatability, reversibility and response time of the sensor

In addition to sensitivity and LOD, the speed of detection is a very critical parameter to evaluate the performance of a sensor. A TNP sensor with rapid response and recovery times, along with

reversible response characteristics holds significant importance. Thus, the dynamic performance, repeatability and reversibility characteristics of the proposed sensor were investigated by exposing the sensor successively to air, 10 ppb TNP concentration, air, 50 ppb TNP concentration and again air. This cyclic exposure between air, low concentration of TNP (10 ppb) and high concentration of TNP (50 ppb) was repeated multiple times, and the corresponding fiber output intensity variations in real time were recorded, as illustrated in Fig. 6.6. As depicted in the figure, the fiber sensor output changes instantly and smoothly during both forward and reverse TNP concentration changes, without any hysteresis, indicating a completely reversible response of the proposed sensor. Zoomed views of a single cycle during exposure to air to 50 ppb and then 50 ppb to air are presented in Fig. 6.7(a) and Fig. 6.7(b). It can be observed from the figures that the sensor exhibits a fast response time and recovery time of 2 seconds. Identical response and recovery times are observed for other cycles as well.

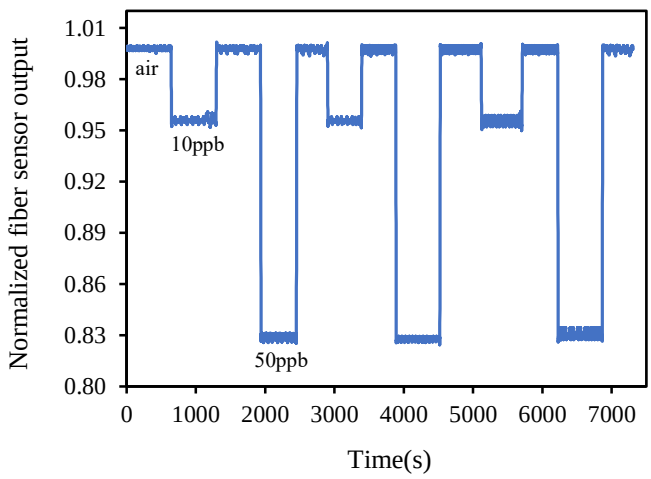

Figure 6.7: Time response of the developed sensor for cyclic variation of TNP concentration.

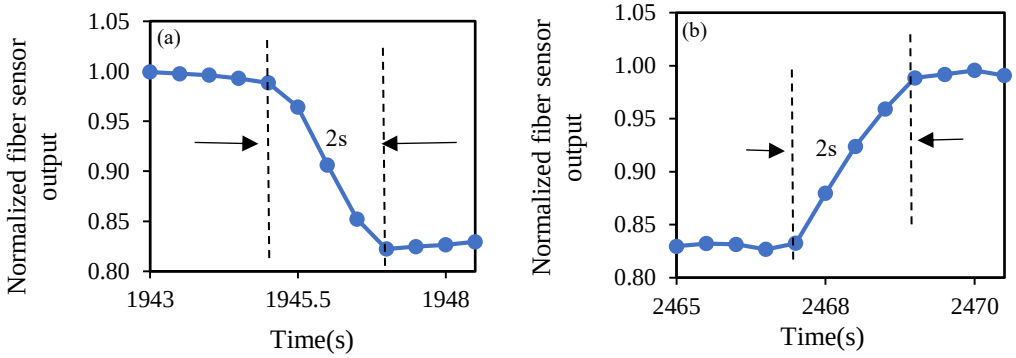

Figure 6.6: (a) Response time (during the variation from air to 50 ppb), (b) Recovery time (during the variation from 50 ppb to air).

Further, in order to test the reversibility and repeatability of the proposed TNP sensor in real-world conditions, where the sensor may encounter higher TNP concentrations, the sensor's dynamic performance, reversibility, and repeatability were re-evaluated. This involved exposing the sensor to a significantly higher concentration of TNP, specifically 100 parts per million (ppm). For that, the time response of the sensor is investigated by exposing the sensor successively to air, 10 ppb TNP concentration, air and then finally 100 ppm TNP concentration. This cyclic variation from air, low TNP concentration (10 ppb) to much higher TNP concentration (100 ppm) is repeated several times and the fiber output intensity in real-time were recorded as depicted in Fig. 6.8. Notably, the sensor exhibited a completely reversible and repeatable response even at the much higher concentration of TNP (100 ppm), without any hysteresis. Furthermore, the sensor's response time and recovery time during the transitions from air to 100 ppm TNP concentration and from 100 ppm TNP concentration to air were evaluated. For that, the sensor demonstrated an average response and recovery time of 3 s. This marginal increase in the response and recovery times from 2 seconds (for the transition from air to 50 ppb TNP concentration) to 3 seconds (for air to 100 ppm concentration) is negligible when compared to the change in TNP concentration, which is of the order of 10^4.

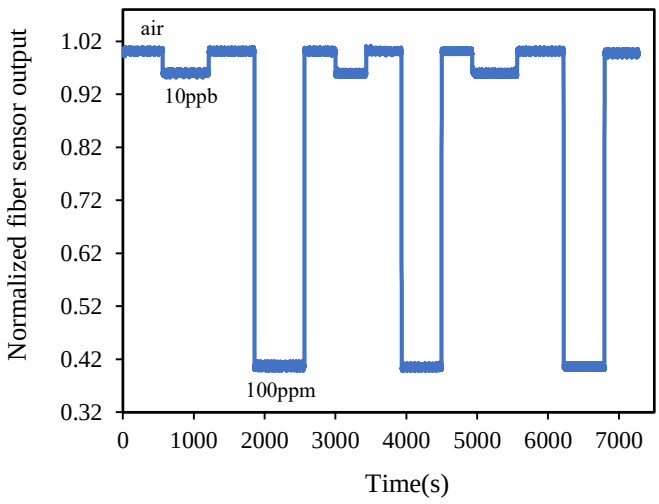

Figure 6.8: Time response of the developed sensor for cyclic variation of TNP concentration (from air, 10 ppb to 100 ppm).

6.3.4 Comparison of the response characteristics of the fiber

Next, the response characteristics of the proposed sensor are compared with other TNP sensors reported in the literature using various sensing schemes. Table 7 provides details of the limit of detection (LOD) for comparative analysis along with response and recovery times. Notably,

most of the reported sensors employ non-optical fiber based fluorescence sensing (NOF) like [48]-[63]. Only two sensors, [77] and [78], utilize optical fiber based fluorescence sensing, while other sensing methods include electrochemical sensing ([55]-[57]) and colorimetric sensing [54]. As can be observed from the table, among all the reported works, [58] showcases the lowest LOD. Nevertheless, the proposed optical fiber TNP sensor significantly outperforms all the reported sensors by demonstrating the lowest LOD of 1.06 ppb. This achieved LOD is ~11.01 times lower than the LOD reported in [58]. Additionally, it's noteworthy that among these reported sensors, only [58] provides information regarding response time (i.e., 10 s), while none of the other sensors offers details on response and recovery time, which are crucial parameters for a sensor. Furthermore, the proposed sensor notably stands out by demonstrating a fast response and recovery time of 2 seconds, which is ~5 times lower than the response time reported in [58].

Table 7: Response comparison of the sensor with other TNP sensors utilizing different sensing techniques.

Ref.	Sensing Technique	Limit of Detection (ppb)	Response time (s)	Recovery time (s)
[54]	Colorimetric and Fluorescence (NOF)	2291 and 3207.4	-	-
[55]	Electrochemical	123.71	-	-
[56]	Electrochemical	8934.9	-	-
[57]	Electroanalytical	922.56	-	-
[48]	Fluorescence (NOF)	20	-	-
[58]	Fluorescence (NOF)	11.68	10	-
[59]	Fluorescence (NOF)	12.83	-	-
[60]	Fluorescence (NOF)	228	-	-
[61]	Fluorescence (NOF)	2291	-	-
[62]	Fluorescence (NOF)	155.78	-	-
[63]	Fluorescence (NOF)	75.6	-	-
[77]	Fluorescence (OF)	5700	-	-
[78]	Fluorescence (OF)	25	-	-
This work	Evanescent wave based Intensity modulation	1.06	2	2

6.3.5 Selectivity of the sensor

Selectivity of the sensor is another very important parameter of a sensor. To test the selectivity of the proposed optical fiber TNP sensor, experiments were performed by testing the optimized

sensor with various other nitro-explosives, including RDX, 4-NT, 2,4-DNT, 1,3-DNB, 2,4-DNP, and 2,6-DNT. The concentration of each nitro-explosive was kept constant at 10 ppm. The sensor probe was immersed in each solution, and the corresponding fiber sensor output was observed using the identical experimental setup employed for TNP detection. The shift in the fiber sensor output intensity were determined for the change in the concentration of each nitro-explosive from 0 to 10 ppm, with the exception of TNP, which was tested at 50 ppb. Fig. 6.9 depicts the shift in fiber sensor output intensity for all the nitro-explosives. As evident from the figure, the sensor exhibits a significantly higher shift in fiber output intensity for TNP compared to all the other nitro-explosives tested, even at a concentration as low as 50 ppb.

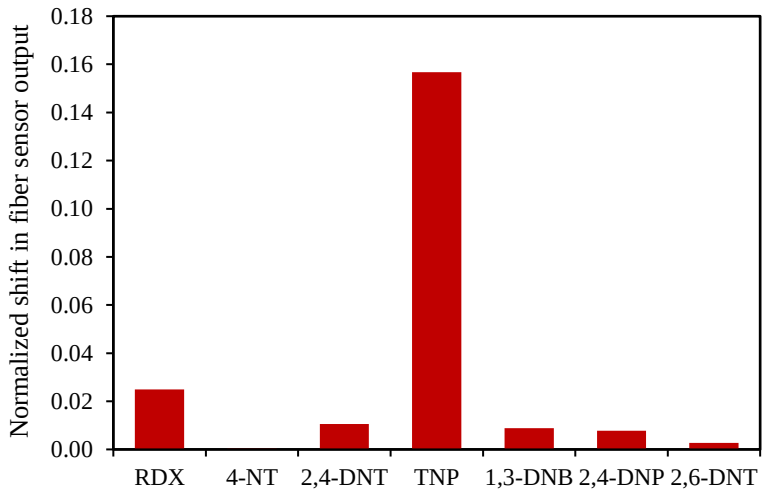

Figure 6.9: Comparison of the shift in fiber sensor output with different nitro-explosives.

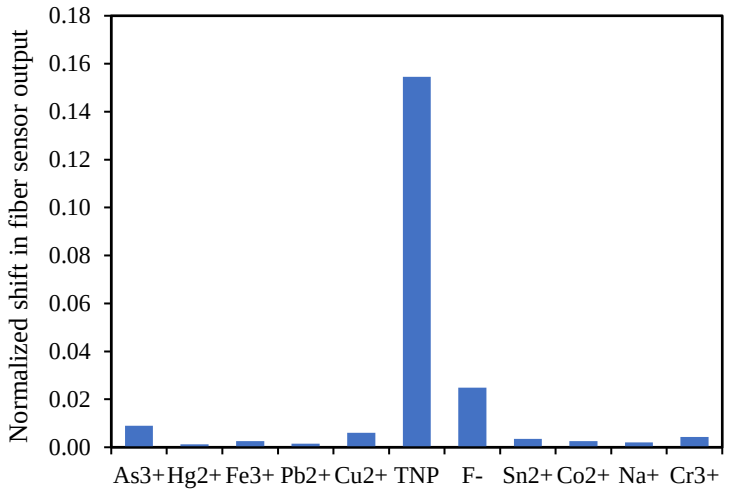

Figure 6.10: Comparison of the shift in fiber sensor output with different heavy metal ions.

Furthermore, to address potential interference from common chemicals e.g., metal ions in aqueous environments, the sensor's selectivity was tested against various metal ions, including As3+, Hg2+, Fe3+, Pb2+, Cu2+, F-, Sn2+, Co2+, Na+, and Cr3+. The fiber sensor output was observed for each metal ion solution at a constant concentration of 10 ppm using the same experimental setup. Fig. 6.10 shows the shifts in fiber sensor output intensity, demonstrating that the sensor depicts a significantly higher response for TNP compared to all the tested metal ions, even at 50 ppb. These results underscore the sensor's remarkable selectivity for TNP, highlighting its potential application in detecting TNP in real field.

6.3.6 Short term and long-term stability or reliability of the sensor

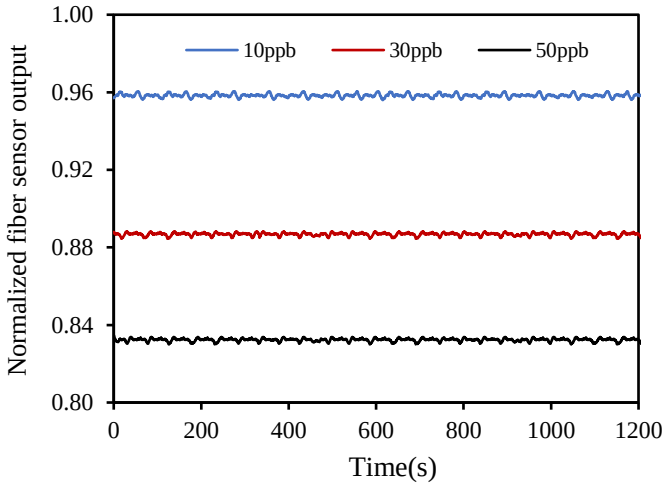

Figure 6.11: Short term stability test: Continuous fiber sensor output for 20 minutes at 50ppb, 30ppb and 20ppb TNP concentration.

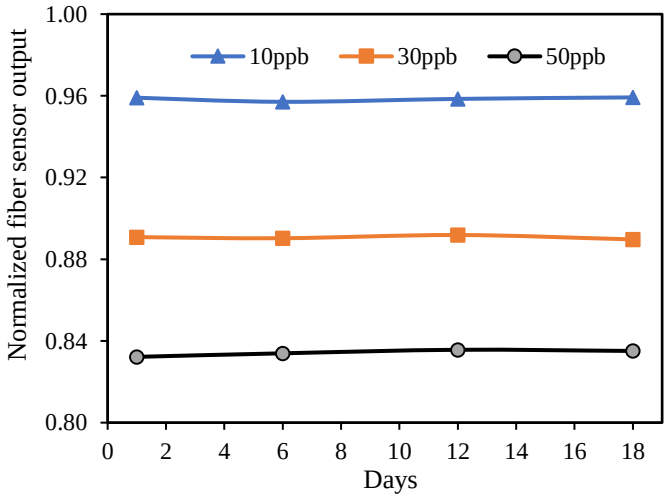

Figure 6.12: Long term stability and repeatability test: Fiber sensor output on four different days at 50ppb, 30ppb and 20ppb TNP concentration.

Stability, repeatability and reliability are other very important parameters for TNP detection. Therefore, comprehensive short-term stability and long-term stability or reliability tests were conducted for the proposed sensor. In order to determine the sensor's short-term stability, the variation in fiber sensor output was continuously recorded over a period of approximately 20 minutes while subjecting the sensor to three distinct TNP ion concentrations (10 ppb, 30 ppb, 50 ppb). The results depicted in Fig. 6.11 conclusively indicate that the sensor exhibits a high level of stability. The standard deviations in the fiber output intensity are observed to be ± 0.00094, ± 0.00079, ± 0.0008 respectively, at 10 ppb, 30 ppb and 50 ppb TNP concentrations. Hence, maximum resolution of the sensor for TNP detection is observed to be ± 0.294 ppb TNP concentration, which indicates the excellent stability and accuracy of TNP detection. For the long-term stability or reliability test, the developed optical fiber explosive sensor underwent testing on four different days with an interval of 4, 5 and 5 days, spanning a total of 18 days. Fig. 6.12 displays the proposed optical fiber sensor output corresponding to three different TNP ion concentrations (10 ppb, 30 ppb, and 50 ppb) observed over the course of these 18 days. Notably, it can be observed from the figure that the maximum variation in output of the developed TNP fiber sensor is less than 0.19%, compared to the first day at all three TNP concentrations. This result underscores the excellent repeatability and reliability of the developed optical fiber TNP sensor.

6.3.7 Temperature Cross-sensitivity of the Sensor

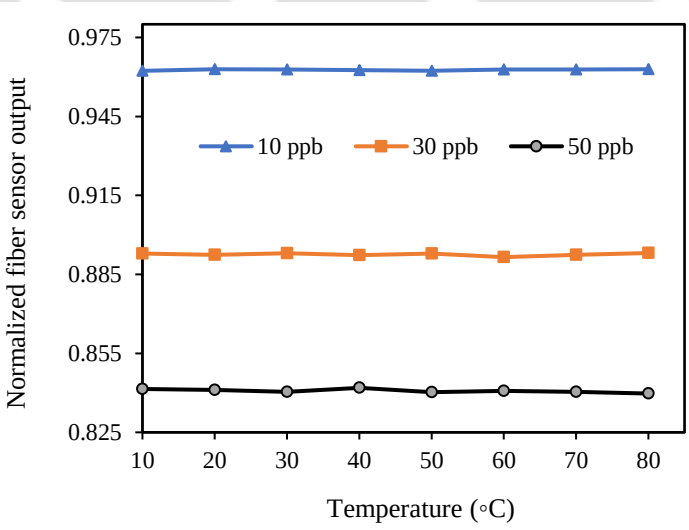

Figure 6.13: Fiber sensor output corresponding to varying temperatures at 10ppb, 30ppb and 50 ppb TNP concentration.

Further, it is crucial to examine the impact of ambient temperature fluctuations on the sensor's performance for real-field applications. As the sensor is developed to detect the explosive (TNP), it becomes specially crucial in this case to understand the impact of the ambient temperature variations. To study this, the sensor was placed in solutions with three different TNP concentrations (10 ppb, 30 ppb, and 50 ppb) maintained at ~80°C. The fiber output was measured at 10°C intervals as the water naturally cooled to room temperature. Additionally, the sensor was tested at 20°C and 10°C for the same concentrations. The thermal response is shown in Fig. 6.13. The standard deviations in fiber output intensity were ±0.00022, ±0.00048, and ±0.00066 for 10 ppb, 30 ppb, and 50 ppb TNP concentrations, respectively. These very low temperature cross-sensitivities indicate that the sensor is highly temperature-independent, making it suitable for real-field applications where continuous ambient temperature changes are inevitable.

6.3.8 Real sample testing

Table 8: Determination of TNP in real water samples.

Samples	TNP added (ppb)	TNP found (ppb)	Recovery (%)	RSD (n=3) (%)
Brahmaputra River Water	5	5.07	101.56	0.022
	25	25.33	101.33	0.04
	50	49.23	98.46	0.016
Drinking Water IIT	5	4.96	99.35	0.015
	25	25.29	101.19	0.052
	50	49.43	98.87	0.023
Near Mill Water	5	5.08	101.72	0.028
	25	25.37	101.49	0.016
	50	49.21	98.42	0.022
Tap Water	5	5.14	102.94	0.001
	25	25.21	100.87	0.026
	50	49.22	98.45	0.008
Well Water	5	5.08	101.79	0.029
	25	24.97	99.89	0.01
	50	49.58	99.16	0.033

Lastly, to verify the applicability of the proposed sensor for commercial use, the proposed optical fiber TNP sensor was tested for detecting TNP in real water samples. For this purpose, water

samples were collected from diverse real water sources in Guwahati, Assam India. The water samples included sources like the drinking water within IIT Guwahati, tap water and well water from the neighboring locality, water from a location near a mill in Guwahati city and sample from the Brahmaputra River. Upon conducting experiments with the optimized optical fiber sensor probe, no traces of TNP were detected in any of the collected samples. Consequently, a recovery test was conducted on real samples spiked with TNP at different concentrations (5 ppb, 25 ppb, and 50 ppb). The results, shown in Table 8, indicated TNP recoveries in the range of 98.42% to 102.94%. Furthermore, the relative standard deviation (RSD) for three replicate tests of each sample was below 0.06%. These outcomes affirm the potential of the proposed optical fiber sensor for effectively detecting TNP in real water sample as well.

6.4 Conclusion

A novel optical fiber explosive (TNP) sensor utilizing evanescent wave based intensity modulation technique is reported for the first time to the best of author's knowledge. The sensor is developed by coating a novel polymer (PFTPA) thin film onto the decladded section of the optical fiber for selective detection of TNP. The sensor displays a linear correlation between TNP concentration and the intensity variation within the range of 0-50 ppb and exhibits a sensitivity of 0.0032/ppb (73.31×10^4 M^{-1}). Also, the developed sensor shows a fast response and recovery time of 2 sec. Moreover, the sensor displays excellent selectivity towards TNP over other nitro-explosives and exhibits significantly low detection limit of 1.06 ppb. Additionally, the maximum fiber output variation during the repeatability and reliability test was observed to be of the order of less than 0.19% only. Thus, this sensor presents a reliable and straightforward solution for real-world monitoring of TNP. Furthermore, the practicality of the proposed optical fiber TNP sensor is confirmed by the determination of TNP in real water samples with recovery range of 98.42% to 102.94%. Although this sensor demonstrated high sensitivity with very low LOD, there is still further scope of improving the sensitivity and further lowering the LOD for TNP detection.

The PFTPA-coated evanescent wave fiber sensor demonstrated strong performance with a limit of detection of 1.06 ppb and excellent stability, making it highly effective for trace-level detection of TNP. However, compared to LSPR-based designs, only one inherent limitation is observed. In evanescent wave sensors, light–matter interaction occurs only through the exponentially decaying evanescent field outside the fiber core, which limits the magnitude of

intensity variation and consequently the overall sensitivity. By contrast, LSPR-based sensors exploit localized plasmonic field enhancement at the nanoparticle interface, greatly amplifying even subtle refractive index variations and enabling much higher sensitivity. This laid the foundation for the research work discussed in the next chapter.

Chapter 7 : Highly Selective and Sensitive LSPR based Optical Fiber Explosive (TNP) Sensor Employing ZnO QDs

7.1 Introduction

The sensor described in Chapter 6 utilizes intensity modulation through the evanescent wave absorption technique to detect trace amounts of TNP. Very good sensitivity and excellent LOD (over 11 times better as compared to the best LOD reported in the literature) was achieved. The quest of achieving further improved response characteristics, especially optimum LOD without compromising on the nature of the response (selectivity, repeatability, reliability etc.) resulted in the development of another optical fiber sensor for the detection of trace amount of TNP which is reported in this chapter.

Proposed sensor reported here, utilizes localized surface plasmon resonance (LSPR) technique, employing ZnO QDs as the sensing material. Gold nanoparticles (AuNPs) are employed to induce LSPR, while ZnO QDs are synthesized onto the AuNPs coated fiber core as the sensing material. Gold nanoparticles (AuNPs) are employed to induce LSPR, while ZnO QDs are synthesized onto the AuNPs coated fiber core as the sensing film. LSPR is a well-known sensing technique due to its high sensitivity, simplicity, rapid response, and cost-effectiveness. This technique exhibits a strong response to changes in localized refractive index, resulting in a shift in the resonance wavelength [114]. It is important to mention that, for the first time to the best of author's knowledge, an optical fiber TNP sensor based on LSPR technique is reported. Recently, ZnO QDs has been extensively used for biosensing, primarily due to its high surface to volume ratio. Additionally, they are less expensive, eco-friendly, biocompatible and less toxic [115]. It is worth mentioning that, ZnO QDs are used for the first time, to the best of authors knowledge, to realize an optical fiber TNP sensor. Rigorous experimental investigations are carried out to establish the response characteristics of the proposed sensor. The sensor exhibits a linear response in the range of 0-50 parts per billion (ppb) with a remarkable limit of detection (LOD) of 0.19 ppb. The sensor also shows high selectivity towards TNP. Even after testing the sensor for over 18 days, the sensing characteristics remained unchanged. This demonstrates the stability and reliability of the proposed optical fiber sensor. These significant findings establish the sensor's potential as an efficient, user-friendly, and cost-effective solution for real-field TNP detection, particularly in aqueous environments. In summary, the proposed optical fiber sensor provides a direct and

simple approach to TNP detection, contributing to the critical need for reliable counterterrorism measures and addressing environmental health concerns.

7.2 Experiment

7.2.1 Synthesis and characterization of ZnO quantum dots

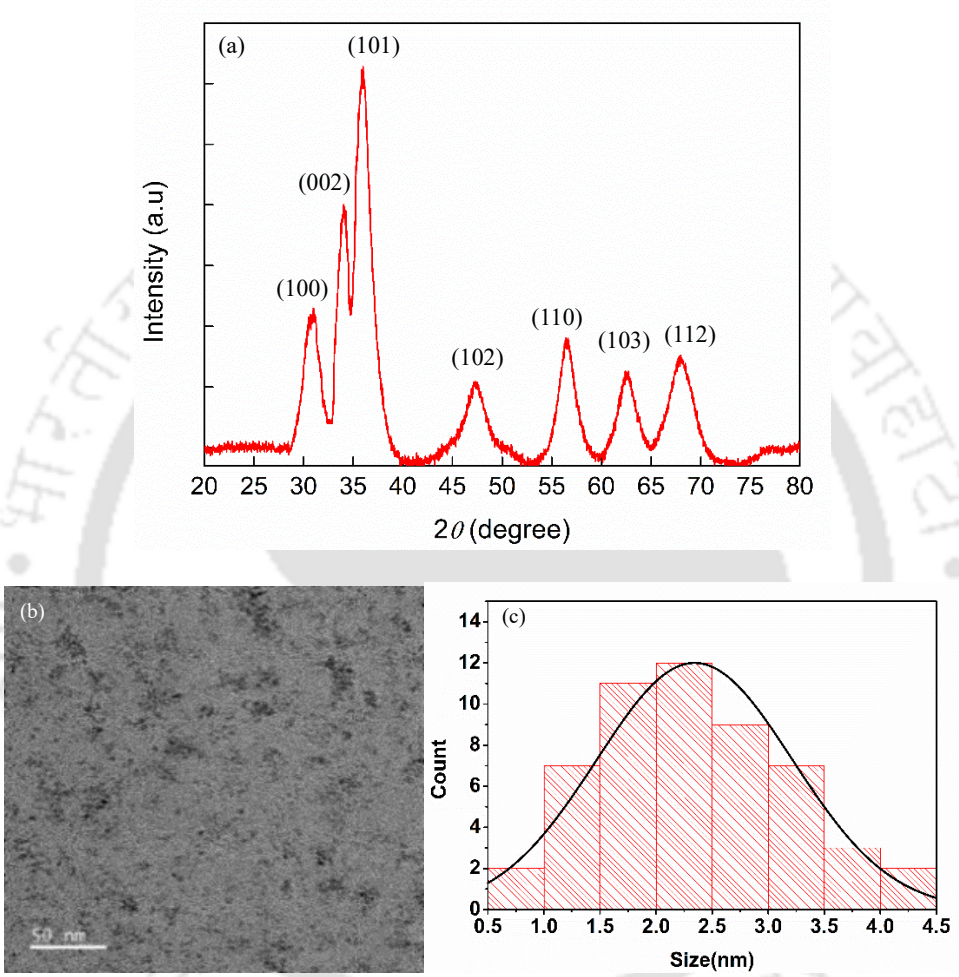

Figure 7.1: (a) XRD image of ZnO QDs, (b) FETEM image of ZnO QDs, (c) Size of the ZnO QDs.

To synthesize ZnO QDs, 140 mmol of Potassium hydroxide (KOH) was dissolved in 80 mL ethanol at 60 °C, followed by reducing the temperature to 4 °C [116]. Subsequently, 100 mmol of zinc acetate dihydrate ($Zn(Ac)_2 \cdot 2H_2O$) was added to a flask containing a 600 mL ethanol solution and stirred at 78 °C until dissolved. Then, the KOH solution was added dropwise to the $Zn(Ac)_2 \cdot 2H_2O$ solution, and the mixture was allowed to react for 30 minutes under continuous stirring. To provide aqueous stability to ZnO QDs, 1.6 mL of (3-aminopropyl) triethoxysilane (APTES) and 6 mL of deionized water was added dropwise to the solution. The solution was then allowed to stir at room temperature for 1 hr. Following this, ZnO QDs precipitated

gradually. Finally, the precipitate was centrifuged at 6000 rpm for 2 minutes, and washed with ethanol to remove unreacted precursors. This process was repeated multiple times to remove unreacted material in the solution.

The structural characterization of synthesized ZnO QDs was conducted using an X-ray diffractometer (XRD, Rigaku TTRAX III) in Bragg–Brentano geometry, operating at 5 kW with Cu-Kα radiation (λ = 1.5406 Å). The XRD spectra is shown in Fig. 7.1(a). In the spectra, ZnO QD diffraction peaks were observed at 31.6°, 34.46°, 36°, 47.28°, 56.44°, 62.7°, and 68°, corresponding to the (100), (002), (101), (102), (110), (103), and (112) crystalline planes of ZnO QDs, respectively [116]. Further, the size and structural morphology of the synthesized ZnO QDs were examined by using FETEM. Fig. 7.1(b) displays a typical FETEM image. While Fig. 7.1(c) showcases the size distribution of the ZnO QD, predominantly ranging from 1.5 to 3 nm, with an average particle size of 2.2 ± 0.06 nm. This result confirms the successful synthesis of ZnO QDs.

7.2.2 Sensor preparation and characterization

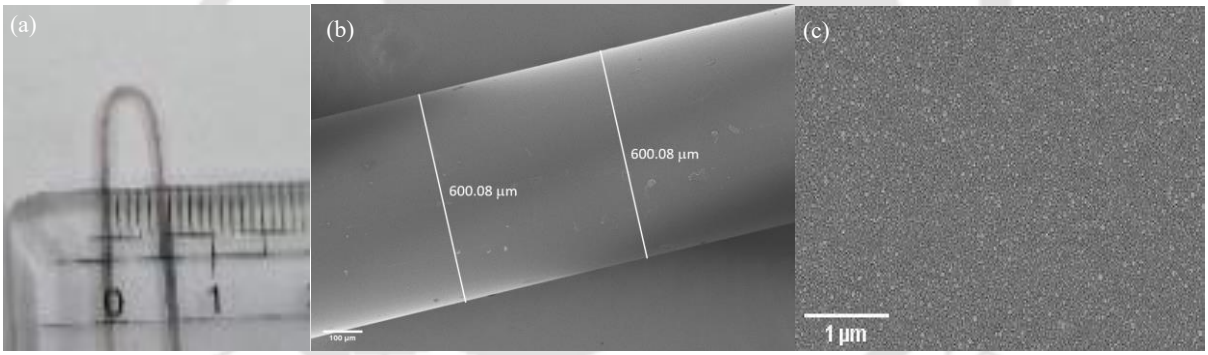

Figure 7.2: (a) AuNPs coated U-shaped probe, (b) FESEM image of the centrally decladded region of the fiber carrying AuNPs coating, (c) FESEM picture of surface morphology of the AuNPs coated region.

A plastic clad silica (PCS) multimode fiber, measuring 40 cm in length and 600 µm in core diameter, was employed to develop the sensing probe. The fiber-ends were prepared to ensure that they were optically flat and perpendicular to the fiber axis. This is critically important in order to achieve maximum power coupling efficiency from source to the fiber and fiber to the detector. Subsequently, a 2.5 cm central section of the fiber was decladded. Then the decladded section was cleaned with soap solution, de-ionized water, and acetone. Thereafter, the decladded section of the fiber was carefully bent into a U-shape. Experiments were conducted only on probes exhibiting uniform core diameter within a perfectly formed U-shaped region.

The U-bend radius of the resulting sensor probe measuring 2.5 mm, are utilized in this research. Following this, the sensing probe was coated with AuNPs using the same procedures as discussed in chapter 2. The AuNPs coated U-shaped optical fiber probe is depicted in Fig. 7.2(a). The thickness of the gold nanoparticle coated probe and the surface morphology of the coated region were analyzed using a Field Emission Scanning Electron Microscope (FESEM) (Zeiss, Sigma 300). Fig. 7.2(b) depicts the image of a section of AuNPs coated U-shaped optical fiber. An average diameter in this is observed to be ~600.08 µm, which establishes an average thickness of the AuNPs filam as ~40 nm. Fig. 7.2(c) shows the surface morphology of the deposited AuNPs film. The image illustrates not only a high density but also uniform coating of the AuNPs on the decladded fiber surface.

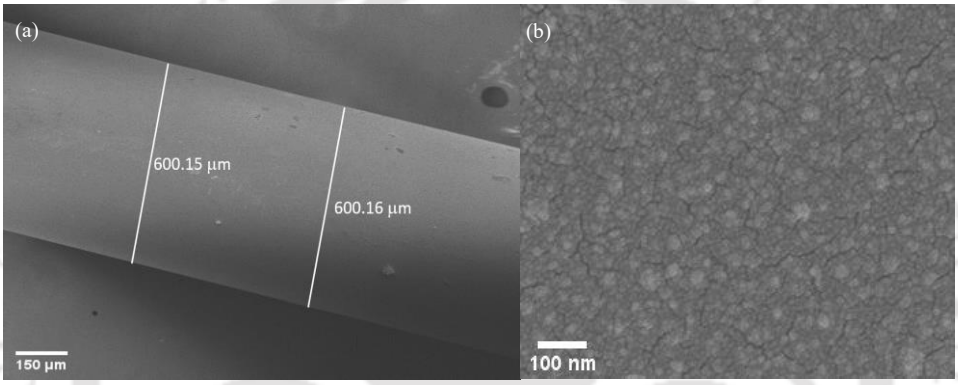

Figure 7.3: (a) FESEM image of the centrally decladded region of the fiber coated with ZnO QDs over the AuNPs coating film. (b) FESEM pattern of surface morphology of the ZnO QDs coating region.

Afterwards, ZnO QDs film was coated over the probe already coated with AuNPs. For that, prepared ZnO QDs was first dispersed in distilled water. Then, the U-shaped region of the fiber was carefully immersed in the ZnO QDs solution and kept at 100°C in an oven. Drying the probe at 100°C results in the evaporation of distilled water and hence, a uniform ZnO QDs film was coated on to the U-shaped region of the fiber. In order to investigate the effect of sensing film composition on the sensor performance, amount of ZnO QDs dispersed in 10ml of distilled water was varied in the order of 170mg, 200mg, 220mg. Next, all the prepared sensing probes were kept in a desiccator under partial vacuum for two days to remove the trace of water from the ZnO QDs film. The surface morphology, nanostructure, and deposited film thickness were examined using FESEM. For example, Fig. 7.3(a) displays an image of the 200 mg of ZnO QDs coating over the AuNPs coated sensing region of the optical fiber. In this region, an average diameter of ~600.155µm was observed, establishing the average thickness of the ZnO

QDs sensing film as ~37.5 nm as the gold coating thickness is already determined to be ~40 nm. Similarly, the thickness for the other two film compositions is determined to be ~27.5 nm for 170 mg and ~72.5 nm for 220 mg of ZnO QDs. Fig. 7.3(b) shows the surface morphology of the deposited sensing film, illustrating an interconnected, high-quality coated surface with moderate roughness.

To investigate the response characteristics of the sensor, similar procedures were followed as described in Chapter 2. Throughout the experiment, TNP concentrations were varied in the range of 0 ppb to 50 ppb.

7.3 Result and discussion

7.3.1 Response of the proposed optical fiber LSPR sensor towards TNP detection

The proposed sensor utilizes the LSPR technique with ZnO QDs as the sensing material, synthesized onto the AuNPs coated U-shaped optical fiber probe. To optimize the sensor's response, the impact of sensing film configuration on its performance was investigated. This entailed varying the concentration of ZnO QDs in distilled water to create different sensing film compositions. Specifically, the amount of ZnO QDs was varied in the distilled water solution, starting from 170 mg, then 200 mg, and finally, 220 mg. Each concentration change resulted in a proportional increase in the film's thickness deposited on the fiber. FESEM measurements determines a film thickness of ~27.5 nm for 170 mg, ~37.5 nm for 200 mg, and ~72.5 nm for 220 mg of ZnO QDs film composition. To examine the performance characteristics of the proposed sensor, outputs from the sensor were monitored in real-time while exposing it to solutions with varying concentrations of TNP (0-50 ppb). Fig. 7.4 depicts the resulting LSPR spectra, as an example, for the sensing probe having a film composition of 200 mg of ZnO QDs. Notably, the figure reveals a significant blue shift in the dip resonance wavelength, accompanied by a decrease in transmittance as the concentration of TNP rises. This can be explained as follows: amine groups are present on the surface of ZnO QDs due to the capping of APTES. When a TNP solution is introduced to the APTES-capped ZnO QDs, the acidic environment causes the amine group to change to ammonium, and exhibits a high affinity for the phenolate group of TNP. This results in the adsorption of TNP onto the surface of ZnO QDs, causing a change in the effective refractive index of the surrounding medium of the AuNPs. As a result, a blue shift is observed in the resonance wavelength of the LSPR spectrum. The response of all the developed sensors with varying film compositions is

thoroughly examined. To gain deeper insight into the effect of film composition, the dip resonance wavelength is plotted against the applied TNP concentration. Fig. 7.5 illustrates the impact of varying ZnO QD concentrations on the response of the sensor. As depicted in the figure, all sensors with different film compositions exhibit a linear response within the range

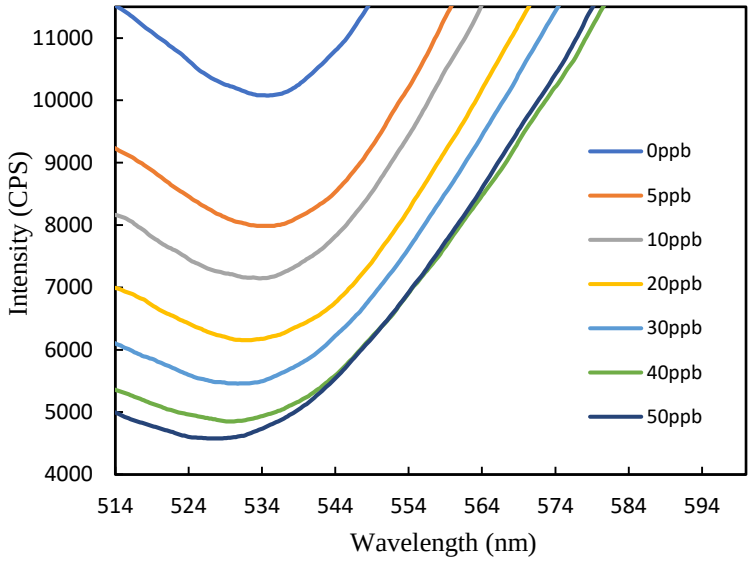

Figure 7.4: LSPR spectrum with varying mercury ion concentrations.

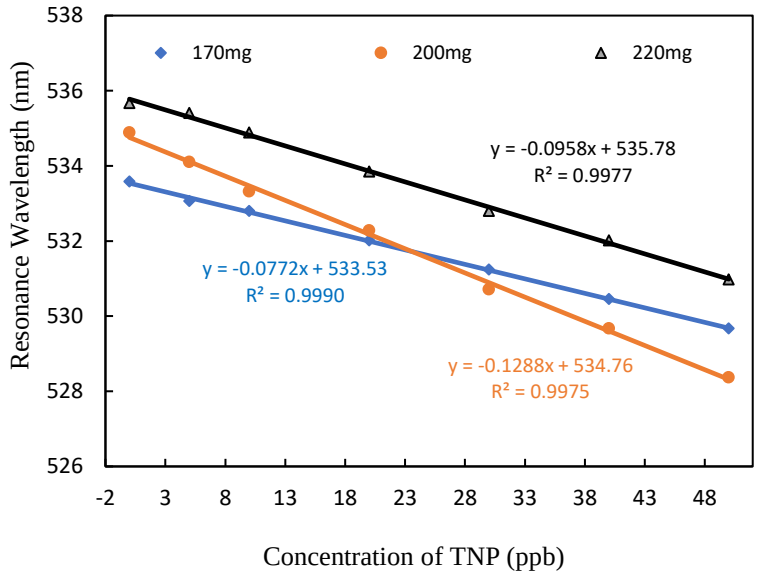

Figure 7.5: Sensor response with different film compositions (170 mg, 200 mg and 220 mg of GO in 10 ml of distilled water).

of 0-50 ppb TNP concentration. For instance, the sensor with a film composition of 170 mg demonstrates a sensitivity of 0.0772 nm/ppb. Upon increasing the concentration of ZnO QDs from 170 mg to 200 mg, the sensitivity rises to 0.1288 nm/ppb, marking an approximately 1.66

times increase compared to the sensitivity observed for the 170 mg film composition. This increase in sensitivity can be attributed to the greater number of adsorption sites available for TNP adsorption, resulting from the higher ZnO QDs concentration. Consequently, this leads to more pronounced changes in the refractive index near the gold nanoparticles, causing a larger shift in the resonance wavelength of the LSPR. Conversely, as the ZnO QDs concentration is further increased from 200 mg to 220 mg, the sensitivity decreases to 0.0958 nm/ppb, approximately 1.34 times lower than the sensitivity observed for the 200 mg film composition. This decline is primarily due to the increased thickness of the sensing film deposited on the U-shaped LSPR probe with the higher ZnO QDs concentration. For ZnO QDs concentration of 220 mg, the film thickness surpasses the decay length (20-40 nm) of the LSPR [91]. As a result, even though more adsorption sites are available for TNP adsorption, they become ineffective in the sensing process. The interaction between TNP and ZnO QDs beyond the LSPR decay length does not influence the resonance wavelength shift, leading to a decrease in sensitivity. These findings establish an optimal film configuration for the sensor, which corresponds to 200 mg of ZnO QDs.

7.3.2 Limit of Detection of the Sensor

In addition to sensitivity, the limit of detection (LOD) is another figure of merit, which is significantly important while evaluating the performance characteristics of a given sensor. For the optimized probe, the LOD was determined to be 0.19 ppb. The achieved LOD of the proposed sensor is significantly lower (~ 2631 times) than the maximum permissible limit for TNP in water set by the surface water environmental quality standards (0.5 ppm). This implies that the proposed sensor is capable of accurately detecting TNP at concentrations lower than the regulatory threshold, making it a promising tool for ensuring the environmental monitoring and safety.

7.3.3 Reusability, reversibility and response time of the sensor

Repeatability/reusability and reversibility are crucial parameters for evaluating a sensor's performance. Thus, these characteristics of the sensor was thoroughly examined by exposing it to the minimum (5 ppb) and maximum (50 ppb) TNP concentrations. Initially, the sensor was exposed to a 5ppb concentration of TNP solution within the flow cell, and the corresponding LSPR spectrum was recorded. The sample was left in the flow cell for 1 min and the LSPR spectrum was recorded again. Subsequently, after removing the 5ppb solution from the flow

cell, the sensor was cleaned with deionized water in order to ensure no trace deposition of TNP solution onto the sensor. Sensor was then exposed to a 50ppb concentration of TNP solution. Corresponding LSPR spectrum is recorded again at an interval of 1 min, completing one cycle of evaluation. To examine the sensor's repeatability, the 5ppb solution was reintroduced into the flow cell, and the results were compared with the initial 5 ppb measurements. This cyclic process was repeated multiple times, typical response for three cycles is shown in Fig. 7.6. As can be observed, the resonance wavelength remains the same for each measurement at lower TNP concentrations, indicating that no TNP residue was left on the sensor after removing the higher concentration solution. The sensor exhibited consistent results during both the forward (5 ppb to 50 ppb) and backward (50 ppb to 5 ppb) change in TNP concentration. This demonstrates the highly repeatable and completely reversible nature of the proposed sensor.

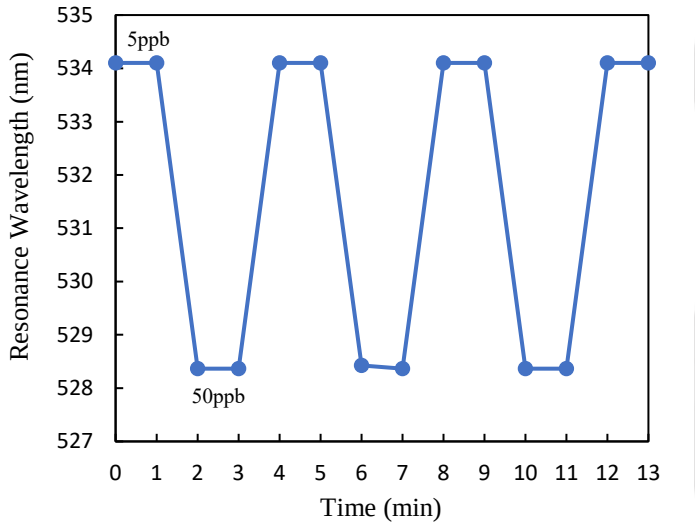

Figure 7.6: Repeatability and reversibility characteristics of the proposed sensor.

Detection speed stands as another critical aspect in evaluating sensor performance, holding notable significance. Rapid response time is essential for effective sensor operation. To examine the response time of the proposed sensor, we measured the LSPR resonance wavelength before and after introducing a 50ppb TNP solution into the flow cell. This involved recording LSPR spectra at every 0.125 sec, and analyzing the corresponding resonance wavelength values. The outcomes are depicted in Fig. 7.7, showcasing the resonance wavelength values plotted against time. Initially, when the sensor is exposed to air, the resonance wavelength remains constant. However, upon introducing the TNP solution into the flow cell, the resonance wavelength experiences blue shifts, gradually stabilizing after

approximately 2 seconds. This stabilization establishes that the proposed sensor achieves its response time of 2 seconds.

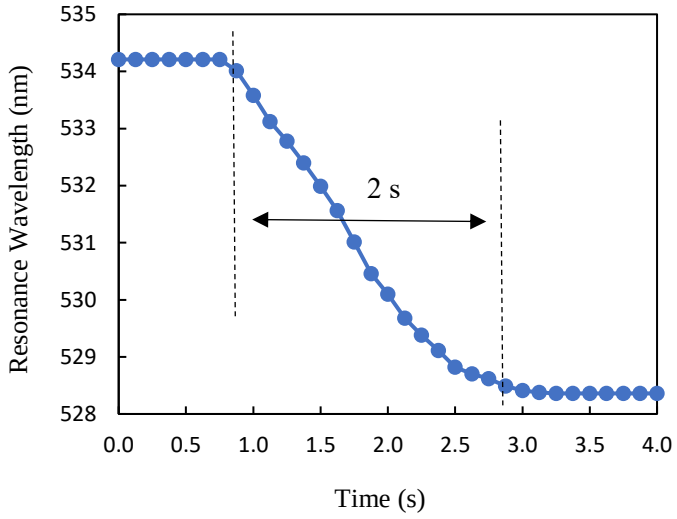

Figure 7.7: Response time (during the variation from air to 50 ppb TNP concentration).

7.3.4 Selectivity of the sensor

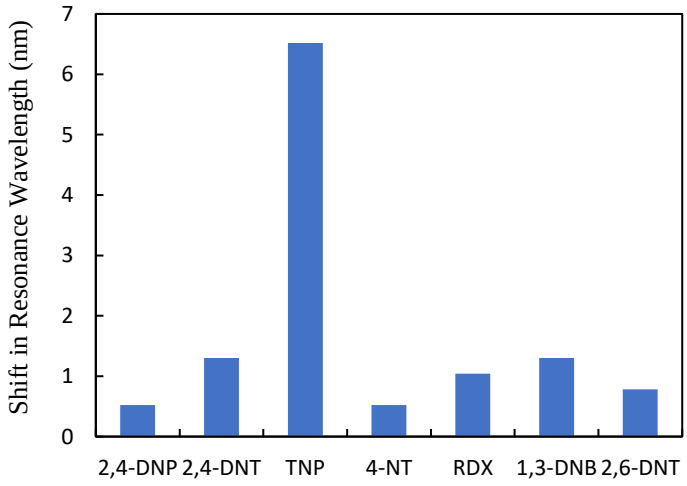

Figure 7.8: Comparison of the resonance wavelength shift of the sensor with different nitro explosives.

Furthermore, the proposed sensor's selectivity was evaluated, which is another crucial aspect of sensor performance. To evaluate the selectivity of the proposed optical fiber TNP sensor, experiments were conducted by testing the optimized sensor with various other nitro-explosives, including 2,4-DNP, 2,4-DNT, 4-NT, RDX, 1,3-DNB and 2,6-DNT. Each nitro-explosive was maintained at a constant concentration of 10 ppm, except for TNP, which was tested at a significantly lower (~200 times) concentration of 50 ppb. The sensor probe was

immersed in each solution, and the corresponding LSPR spectrum was observed using the same experimental setup utilized for TNP detection. The shift in the resonance wavelength was determined for the change in the concentration of each nitro-explosive from 0 to 10 ppm, except for TNP, which was tested at 50 ppb. As illustrated in Fig. 7.8, the sensor exhibited a significantly higher shift in the resonance wavelength for TNP compared to all the other nitro-explosives tested, even at a concentration as low as 50 ppb.

To evaluate potential interference from common chemicals, particularly heavy metal ions in aqueous environments, the sensor's selectivity was tested against various heavy metal ions, including As^{3+}, Hg^{2+}, Pb^{2+}, Sn^{2+}, Cu^{2+}, F^{-}, Fe^{3+}, and Cr^{3+}. The LSPR spectrum was measured for each metal ion solution at a constant concentration of 10 ppm using the same experimental setup. Fig. 7.9 illustrates the shifts in resonance wavelength, showing a significantly higher response for TNP compared to all tested heavy metal ions, even at 50 ppb. This outcome emphasizes the sensor's exceptional selectivity for TNP, highlighting its potential for detecting TNP in real-field applications.

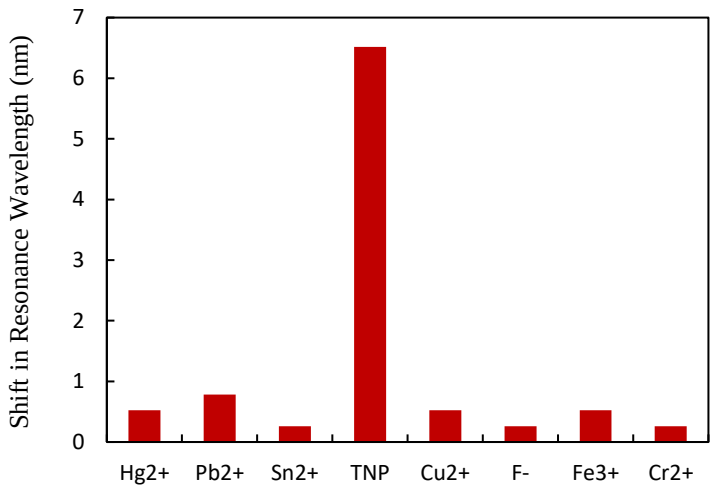

Figure 7.9: Comparison of the resonance wavelength shift of the sensor with different heavy metal ions.

7.3.5 Stability and reliability of the sensor

Stability, repeatability, and reliability are other critical parameters crucial for TNP detection. Therefore, comprehensive analysis was conducted to thoroughly examine the short-term and long-term performance of the proposed sensor. To evaluate the sensor's short-term stability, the LSPR spectrum was continuously recorded at 1-minute interval for 16 minutes while exposing the sensor separately to three distinct TNP concentrations (5 ppb, 30 ppb, 50 ppb). The results

are illustrated in Fig. 7.10. The standard deviations of the resonance wavelength were observed to be ± 0.0249 nm, ± 0.0143 nm, and ± 0.0218 nm at 5 ppb, 30 ppb, and 50 ppb TNP concentrations, respectively. Thus, the sensor exhibits a maximum resolution of ± 0.193 ppb for TNP detection, highlighting its exceptional stability and accuracy. For the long-term stability or reliability test, the developed optical fiber TNP sensor underwent testing on four different days with an interval of 5 days at three different TNP concentrations (5 ppb, 30 ppb,

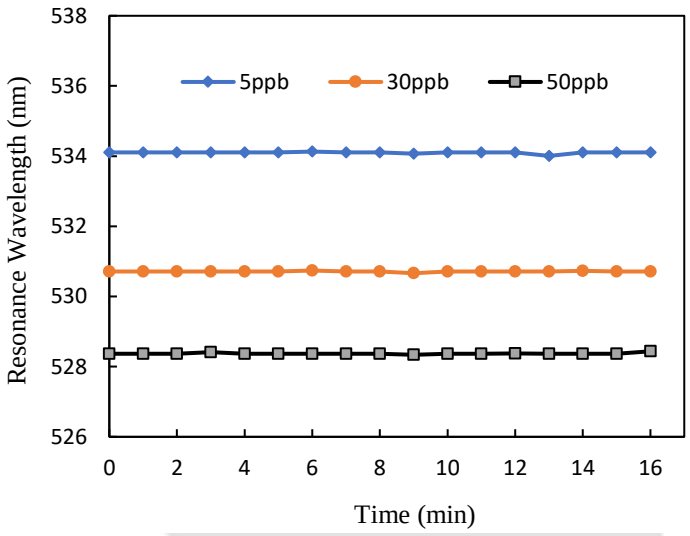

Figure 7.10: Short term stability test: Continuous resonance wavelength for 16 minutes at 5ppb, 30ppb and 50ppb TNP concentration.

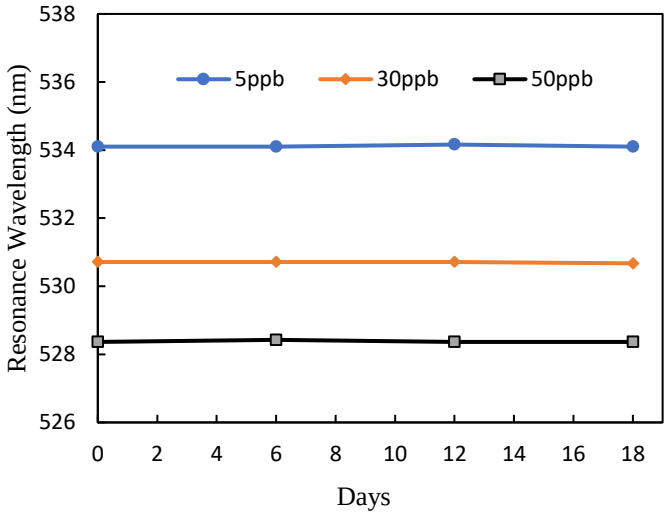

Figure 7.11: Repeatability and reliability test: Resonance wavelength on four different days at 5ppb, 30ppb and 50ppb TNP concentration.

and 50 ppb) over a span of 18 days. The observed results, depicted in Fig. 7.11, reveal that the maximum variation in the resonance wavelength of the developed TNP optical fiber sensor is

less than 0.005% of the resonance wavelength recorded on the first day. This outcome highlights the excellent repeatability and reliability of the developed optical fiber TNP sensor.

7.3.6 Temperature Cross-sensitivity of the Sensor

Further, as described in the previous chapter it is very important to examine the impact of ambient temperature fluctuations on the sensor's performance while detecting explosives in real-field applications. For that, the sensor was immersed in solutions with three different TNP concentrations (5 ppb, 30 ppb, and 50 ppb) maintained at ~80°C. As the water naturally cooled, LSPR spectrum was recorded at 10°C intervals until it reached room temperature. The sensor was also tested at 20°C and 10°C for the same concentrations. The thermal response of the proposed sensor is shown in Fig. 7.12. The standard deviations of the resonance wavelength were observed to be ±0.01309 nm, ±0.01594 nm, and ±0.01665 nm for 5 ppb, 30 ppb, and 50 ppb TNP concentrations, respectively. These low temperature cross-sensitivities confirm that the sensor is highly temperature-independent, making it suitable for real-field applications where ambient temperature fluctuations are inevitable.

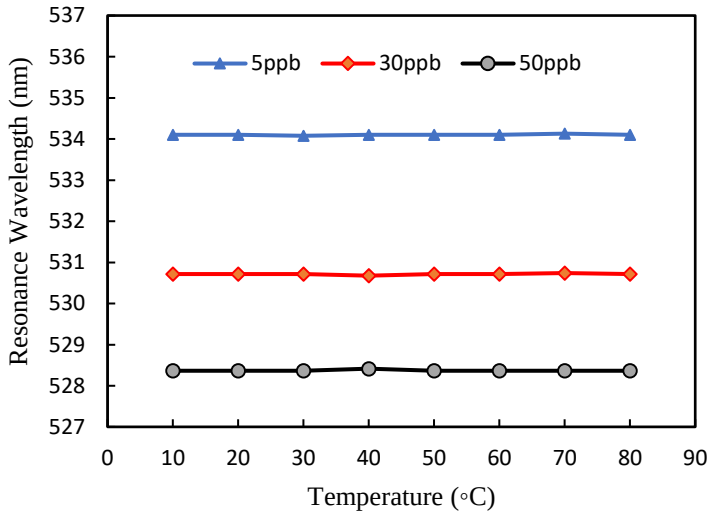

Figure 7.12: Fiber sensor output corresponding to varying temperatures at 5ppb, 30ppb and 50ppb TNP concentration.

7.3.7 TNP detection in real water samples

In order to find out the practical applicability of the proposed sensor, real water samples were tested for TNP detection using the optical fiber TNP sensor. These samples were collected from various sources across Guwahati, Assam, India. These water samples included Indian Institute

of Technology Guwahati's drinking water, tap water and well water from neighbouring areas, water from a mill in Guwahati city, and samples from the Brahmaputra River. Despite testing with the optimized optical fiber sensor probe, no traces of TNP were detected in any of the collected samples. Consequently, a recovery tests were conducted on real samples spiked with TNP at different concentrations (5 ppb, 30 ppb, and 50 ppb). The results, presented in Table 9, revealed TNP recoveries ranging from 97.14% to 104.74%. Additionally, the relative standard deviation (RSD) for five replicate tests of each sample was found to be below 0.032%. These findings validate the potential of the proposed optical fiber sensor for effectively detecting TNP in real water samples. These findings strongly suggest that the proposed optical fiber LSPR sensor is a reliable, simple, and cost-effective alternative to conventional techniques for accurately detecting TNP.

Table 9: Determination of TNP in real water samples

Samples	TNP added (ppb)	TNP found (ppb)	Recovery (%)	RSD (n=5) (%)
Brahmaputra River Water	5	5.20	104.01	0.004
	30	31.42	104.74	0.031
	50	50.05	100.10	0.019
Drinking Water IIT	5	4.85	97.14	0.012
	30	31.01	103.39	0.019
	50	49.64	99.29	0.031
Near Mill Water	5	5.15	103.08	0.002
	30	31.42	104.74	0.031
	50	48.83	97.67	0.024
Tap Water	5	4.99	99.93	0.005
	30	31.01	103.39	0.019
	50	49.24	98.48	0.019
Well Water	5	5.08	101.70	0.001
	30	31.01	103.39	0.019
	50	50.05	100.10	0.019

7.4 Conclusion

A novel optical fiber sensor for detecting the explosive compound TNP utilizing LSPR technique is reported for the first time in the best of author's knowledge. The sensor demonstrates a linear relationship between TNP concentration and the resonance wavelength

variation within the range of 0-50 ppb, exhibiting a sensitivity of 0.1288 nm/ppb. Additionally, the sensor achieves a remarkably low detection limit of 0.19 ppb and shows outstanding selectivity towards TNP. Moreover, the sensor exhibits a rapid response time of 2 seconds. During repeatability and reliability testing, the maximum variation in resonance wavelength was found to be less than 0.005%, indicating high degree of repeatability and reliability. Furthermore, its practicality is confirmed through successful determination of TNP in real water samples, with recovery rates ranging from 97.14% to 104.74%. The reported sensor achieved an enhanced sensitivity, a significantly lower LOD (~5.5 times) while maintaining the same response time, high selectivity, stability, repeatability and reliability in comparison to the sensor reported in chapter 6. Overall, this sensor offers a reliable, cost effective and straightforward solution for real-world TNP monitoring applications.

s

Chapter 8 : Conclusion and future scope

8.1 Conclusion

This thesis presents a comprehensive experimental study aimed at achieving optimal sensitivity, exceptionally low LOD, ultrafast response time, and high repeatability and reliability by employing a simple optical fiber sensor configuration. Intensity modulation via evanescent wave (EW) and wavelength modulation by localized surface plasmon resonance are utilized to develop optical fiber Hg^{2+}, As^{3+} and TNP sensors, employing novel sensing configurations within a very short sensing region. The responses of the developed sensors were optimized by varying chemical composition of the sensing material. Further, the response characteristics such as LOD and response time were compared with the other Hg^{2+}, As^{3+} and TNP sensors using different sensing techniques reported in the literature. The first part of the research, AuNPs were coated onto the centrally decladded U-shaped core of the PCS optical fiber followed by the coating of GO-CS composite for the development of the sensor. The sensor exhibits a linear response across the 0–200 ppb range, with a sensitivity of 0.0728 nm/ppb for Hg^{2+} concentration and an impressively low LOD of 0.29 ppb. The achieved LOD is substantially lower than the regulatory threshold set by the WHO for Hg^{2+} in drinking water. It exhibits high reversibility and stability, with average response time of 0.6 s. Another optical fiber Hg^{2+} sensor is developed to further enhance sensitivity and reduce the LOD by incorporating CNT/PVA nanocomposite film, utilizing the same fiber configuration. Optimizing the sensing film configuration results in an enhanced sensitivity of 0.2458 nm/ppb over the range of 0-30 ppb Hg^{2+} concentration. The average response time of the sensors is 0.4 s and the LOD is determined to be 0.08 ppb. Next, a novel optical fiber sensor for detecting another highly toxic water contaminant As^{3+} is developed. The sensor utilizes the LSPR technique, employing an aluminum oxide/graphene oxide (Al_2O_3/GO) nanocomposite as the sensing material. The optimized sensor exhibits a linear response within the 0–20 ppb range with a high sensitivity of 0.1833 nm/ppb along with high selectivity towards As^{3+}. The proposed sensor also exhibits an impressively low LOD of 0.09 ppb, which is significantly lower than the threshold of As^{3+} set by WHO in drinking water. Furthermore, the proposed sensor demonstrates an average fast response time of 0.5 s. In order to enhance response characteristics, another optical fiber As^{3+} sensor is developed, incorporating a sensing film of lauryl sulphate functionalized gold nanoparticles. This sensor demonstrates an enhanced

sensitivity of 0.3073 nm/ppb. The sensing probe shows linear dynamic range of 0-30 ppb with a very low LOD of 0.06 ppb. The sensor also exhibits a high selectivity towards As^{3+} ions. Additionally, the proposed sensor exhibits an average response time of 0.5 s. In the next part of the research, a simple yet innovative optical fiber sensor for detecting the explosive compound TNP is developed. To accomplish this, a polymer PFTPA film is synthesized onto the centrally decladded straight PCS fiber. For this sensor, intensity modulation through evanescent wave absorption technique is employed. The optimized sensor demonstrates a linear response within the 0-50 ppb range, with a high sensitivity of 0.0032/ppb (73.31×10^4 M^{-1}) and a remarkably low LOD of 1.06 ppb. The sensor also shows excellent selectivity for TNP and offers a rapid response time of just 2 s. To further improve the sensing performance for detecting TNP, in the next work an LSPR based optical fiber sensor is developed that employs ZnO QDs as the sensing material. The optimized sensor displays a linear response in the range of 0–50 ppb, with an enhanced sensitivity of 0.1288 nm/ppb and a remarkably low LOD of 0.19 ppb for TNP. Additionally, the sensor demonstrated high selectivity towards TNP and exhibits an average response time of 2 s. It is worth mentioning that all the novel sensors developed in the research presented here exhibit high degree of stability, reversibility, repeatability and reliability. Furthermore, in order to find out the real-field applicability of the all proposed optical fiber sensors, the proposed sensors were employed to detect Hg^{2+}, As^{3+}, and TNP in real water samples as well.

8.2 Future scope

The research presented in this thesis has successfully laid a strong foundation for the development of highly sensitive and selective optical fiber sensors for detecting Hg^{2+}, As^{3+}, and TNP. While the proposed sensors demonstrate excellent performance in terms of sensitivity, selectivity, and response time, there is significant potential for further advancements. The following key areas are suggested for future research:

Development of Multi-Parameter Sensors for Heavy Metal Ions

The current research focuses on the detection of mercury (Hg^{2+}) and arsenic (As^{3+}). However, several other toxic heavy metals, such as lead (Pb^{2+}), fluoride (F^-), iron (Fe^{3+}), and nickel (Ni^{2+}), also pose severe environmental and health risks. Future research should aim at extending the sensing capabilities of the proposed optical fiber platform by designing multi-parameter sensors capable of detecting multiple toxic heavy metals simultaneously. This can be achieved

by employing a combination of nanomaterials with distinct affinities for different metal ions, allowing for selective detection in complex real-world samples.

Expansion of Nitroexplosive Detection Beyond TNP

The present study primarily focuses on the detection of trinitrophenol (TNP). However, other nitroexplosives, such as trinitrotoluene (TNT), dinitrotoluene (DNT), and pentaerythritol tetranitrate (PETN), are also critical targets for security and defense applications. Future efforts should be directed toward the development of optical fiber sensors that can selectively and sensitively detect a broader range of nitroexplosives using novel functional materials, such as metal-organic frameworks (MOFs), quantum dots, and molecularly imprinted polymers (MIPs).

Detection of TNP in Vapour Form

Currently, the developed sensors demonstrate efficient detection of TNP in aqueous solutions. However, for practical security applications, it is crucial to extend the detection capability to the vapor phase. Detecting TNP vapours is vital for counterterrorism and environmental monitoring. Future research can explore modifications in the sensing layer, such as employing advanced nanomaterials that can enhance adsorption and interaction with TNP vapours.

Packaging and Integration for Real-Field Deployment

The developed sensors have undergone extensive experimental evaluations, including both laboratory tests and real-site sample analyses. Moving forward, these sensors need to be integrated into portable, user-friendly devices, ensuring protection from environmental contaminants while maintaining efficient interaction with target analyte. By packaging the developed sensors, the developed optical fiber sensors can be transformed into practical, real-world tools for environmental monitoring, water safety, and security applications.

Further Enhancement in Sensitivity, Limit of detection, Selectivity and Response time

Despite achieving impressive sensitivity, LOD, response time and selectivity, there is always room for further enhancement. This can be pursued by:

- **Exploring novel nanomaterials** such as quantum dots, 2D materials, and hybrid nanocomposites.

- **Improving optical configurations** to maximize evanescent wave interactions or enhance localized surface plasmon resonance effects.
- **Developing artificial intelligence-based data processing algorithms** to analyze spectral shifts and improve detection accuracy in complex real-world samples.

By advancing in these directions, the optical fiber sensors developed in this research can significantly contribute to environmental monitoring, security applications, and real-time field detection of hazardous substances.

Use of sustainable sensing materials

To further improve sustainability, future work can focus on incorporating eco-friendly nanomaterials, biodegradable polymers, or encapsulation strategies that both enhance stability and ensure minimal release risk. By combining controlled fabrication, proper waste management, and the use of greener materials, the deployment of such sensors can be aligned with both environmental safety and sustainable monitoring practices.

8.3 Publications

(A) JOURNAL PUBLICATIONS

1. F. Banoo, M. A. Chanu, P. K. Iyer, S. K. Khijwania, "Novel Optical Fiber Sensor for Explosive (Trinitrophenol) Detection," *J. LightWave. Technol.*, pp. 2–5, 2024, doi: 10.1109/JLT.2024.3453191.
2. F. Banoo, S. K. Khijwania, "Localized surface plasmon resonance based optical fiber arsenic ion sensor employing Al_2O_3/GO nanocomposite," *Appl. Opt.*, doi: 10.1364/AO.544358.
3. F. Banoo, S. Mohan, S. K. Khijwania, "Novel LSPR based U-shaped optical fiber mercury ion sensor employing Graphene oxide functionalized with Chitosan," (Communicated)
4. F. Banoo, S. K. Khijwania, "Highly Selective and Sensitive LSPR based Optical Fiber Explosive (TNP) Sensor Utilizing ZnO QDs," (Communicated)
5. F. Banoo, S. K. Khijwania, "Highly selective and sensitive LSPR based optical fiber Arsenic ion sensor employing functionalized gold nanoparticles," (Communicated)
6. F. Banoo, S. K. Khijwania, "LSPR based novel optical fiber mercury ion sensor employing CNT/PVA nanocomposite," (Communicated)

(B) CONFERENCE PROCEEDINGS

1. F. Banoo, S. K. Khijwania, "Optical Fiber Lspr Sensor Employing Graphene Oxide Nanocomposite for Arsenic Detection," *ofs2023*, Th6.36, pp. 3-6, 2023, doi:

10.1364/OFS.2023.Th6.36.

2. F. Banoo, M. A. Chanu, P. K. Iyer, S. K. Khijwania, "Novel Optical Fiber Sensor for Explosive (Trinitrophenol) Detection," *ofs2023*, Tu3.39, pp. 2-5, 2023, doi: 10.1364/OFS.2023.Tu3.39.
3. F. Banoo, S. Mohan, S. K. Khijwania, "Development of LSPR-Based Optical Fiber Sensor Employing Graphene Oxide (GO) for the detection of Mercury in Water", *PHOTONICS 2023. Lecture Notes in Electrical Engineering*, vol 1225. Springer, Singapore. doi.org/10.1007/978-981-97-4884-6_1.

(C) PAPERS PRESENTED IN CONFERENCES (NATIONAL & INTERNATIONAL)

1. F. Banoo, S. Mohan, S. K. Khijwania, "Development of LSPR based optical fiber sensor employing Graphene oxide for the detection of mercury in water," International Conference on Photonics "Photonics 2023", 5 – 8 July, 2023, IISc Bengaluru. (Oral presentation)
2. F. Banoo, S. K. Khijwania, "Optical Fiber Lspr Sensor Employing Graphene Oxide Nanocomposite for Arsenic Detection," 28th international conference on optical fiber senor "OFS28", 20 – 24 November, 2023, Hamamatsu (Japan). (Poster presentation)
3. F. Banoo, M. A. Chanu, P. K. Iyer, S. K. Khijwania, "Novel Optical Fiber Sensor for Explosive (Trinitrophenol) Detection," 28th international conference on optical fiber senor "OFS28", 20 – 24 November, 2023, Hamamatsu (Japan). (Poster preasentation)
4. F. Banoo, S. Mohan, S. K. Khijwania, "LSPR based optical fiber mercury ion sensor utilising Graphene oxide functionalized with Chitosan," Research and Industrial Conclave 2024 "RIC 2024", 9 – 11 August, 2024, IIT Guwahati. (Oral presentation)
5. F. Banoo, S. Khijwania, " Highly Selective and Sensitive LSPR based Optical Fiber Explosive (TNP) Sensor Utilizing ZnO QDs," International Conference on Fiber Optics and Photonics "Photonics – 2024" 12 – 15 December, 2024, IIT Kharagpur. (Poster presentation)
6. F. Banoo and S. K. Khijwania, "Localized Surface Plasmon Resonance based Optical Fiber Mercury Ion Sensor Employing CNT/PVA nanocomposite", 29th international conference on optical fiber senor "OFS29", 25 – 30 May, 2025, Porto (Portugal). (Accepted)

References

1. B. P. Pal, “Fundamentals of fiber optics in telecommunication and sensor systems”, (New Age Inc., 2003).
2. S. K. Khijwania, K. L. Srinivasan, and J. P. Shingh, “Performance optimized optical fiber sensor for humidity measurement,” Optical Engineering, vol. 44, no. 3, p. 034401, 2005, doi: 10.1117/1.1870753.
3. B. D. Gupta, H. Dodeja, and A. K. Tomar, “Fiber optic evanescent field absorption sensor based on U-shaped probe,” Opt. Quantum Electron . 28, 1629-1639 (1996).
4. S. K. Khijwania and B. D. Gupta “Fiber optic evanescent field absorption sensor based on tapered probe: effect of fiber parameters on the response curve,” Proc. SPIE 3666, 578-584 (1999).
5. V. Rudy, “ An effective attenuation coefficient for evanescent wave spectroscopy using multimode fiber,” Fiber Integr. Opt. 9, 142_150 (1990).
6. N. K. Sharma and B. D. Gupta, “Fabrication and characterization of pH sensor based on side polished single mode optical fiber,” Optics Communications, vol. 216, no. 4–6, pp. 299–303, 2003.
7. H. S. Haddock, P. M. Shankar, and R. Mutharasan, “Fabrication of biconical tapered optical fibers using hydrofluoric acid,” Materials Science and Engineering: B, vol. 97, no. 1, pp. 87–93, 2003.
8. B. H. Lee, Y. H. Kim, K. S. Park, J. B. Eom, M. J. Kim, B. S. Rho, and H. Y. Choi Interferometric fiber optic sensors,” Sensors, vol. 12, no. 3, pp. 2467–2486, 2012.
9. A. Miliou, “In-fiber interferometric-based sensors: Overview and recent advances,” Photonics, vol. 8, no. 7, 2021.
10. P. S. J. Russell, “Photonic Crystal Fibers,” Optics InfoBase Conference Papers, vol. 299, no. JANUARY, pp. 358–363, 2003.
11. D. H. Kim and J. U. Kang, “Sagnac loop interferometer based on polarization maintaining photonic crystal fiber with reduced temperature sensitivity,” Optics Express, vol. 12, no. 19, p. 4490, 2004.
12. H. Y. Fu, H. Y. Tam, L. Y. Shao, X. Dong, P. K. A. Wai, C. Lu, and S. K. Khijwania, “Pressure sensor realized with polarization-maintaining photonic crystal fiber-based Sagnac interferometer,” Applied Optics, vol. 47, no. 15, pp. 2835–2839, 2008.
13. B. Culshaw and A. Kersey, “Fiber-Optic Sensing : A Historical Perspective,” vol. 26, no. 9, pp. 1064–1078, 2008.
14. K. O. Hill and G. Meltz, “Fiber Bragg grating technology fundamentals and overview,” Journal of Lightwave Technology, vol. 15, no. 8, pp. 1263–1276, 1997.
15. A. D. Kersey, M. A. Davis, H. J. Patrick, M. LeBlanc, K. P. Koo, C. G. Askins, M. A. Putnam, and E. J. Friebele , “Fiber grating sensors,” Journal of Lightwave Technology, vol. 15, no. 8, pp. 1442–1462, 1997.
16. S. Unser, I. Bruzas, J. He, and L. Sagle, “Localized Surface Plasmon Resonance Biosensing: Current Challenges and Approaches,” pp. 15684–15716, 2015.
17. S. Schlücker, “Surface-enhanced raman spectroscopy: Concepts and chemical applications,” *Angew. Chemie - Int. Ed.*, vol. 53, no. 19, pp. 4756–4795, 2014.
18. J. R. Adleman, D. A. Boyd, D. G. Goodwin, and D. Psaltis, “Heterogenous catalysis mediated by plasmon heating,” *Nano Lett.*, vol. 9, no. 12, pp. 4417–4423, 2009.
19. M. P. Nielsen, A. Ashfar, K. Cadien, and A. Y. Elezzabi, “Plasmonic materials for metal-insulator-semiconductor-insulator-metal nanoplasmonic waveguides on silicon-on-insulator platform,” *Opt. Mater. (Amst).*, vol. 36, no. 2, pp. 294–298, 2013.
20. M. Sun and H. Xu, “A novel application of plasmonics: Plasmon-driven surface-catalyzed reactions,” *Small*, vol. 8, no. 18, pp. 2777–2786, 2012.

21. B. Kang, M. M. Afifi, L. A. Austin, and M. A. El-Sayed, "Exploiting the nanoparticle plasmon effect: Observing drug delivery dynamics in single cells via Raman/fluorescence imaging spectroscopy," *ACS Nano*, vol. 7, no. 8, pp. 7420–7427, 2013.
22. L. B. Sagle, L. K. Ruvuna, J. A. Ruemmele, R.P. van Duyne, "Advances in localized surface plasmon resonance spectroscopy biosensing," *Nanomedicine*, vol. 6, pp. 1447–1462, 2011.
23. Katherine A. Willets and Richard P. Van Duyne, Localized Surface Plasmon Resonance Spectroscopy and Sensing, Annual Review of Physical Chemistry 2007 58:1, 267-297
24. Mie G. 1908. Contributions to the optics of turbid media, especially colloidal metal solutions. Ann. Phys. 25:377-445.
25. Link S, El-Sayed MA. 1999. Spectral properties and relaxation dynamicsof surface plasmon electronic oscillations in gold and silver nano-dots and nano-rods. Phys. Chem. B 103:8410-26.
26. S. E. E. Profile, *Nanoplasmonics - Fundamentals and Applications*, no. June. 2017.
27. M. S. Sankhla, M. Kumari, M. N. Agrawal, R. Kumar, and A. Prashant, "Heavy Metals Contamination in Water and their Hazardous Effect on Human Health-A Review," Int. J. Curr. Microbiol. Appl. Sci., vol. 5, no. 10, pp. 759–766, 2016.
28. N. Ratner and D. Mandler, "Electrochemical detection of low concentrations of mercury in water using gold nanoparticles," *Anal. Chem.*, vol. 87, no. 10, pp. 5148–5155, 2015.
29. R. L. Calderon, "The epidemiology of chemical contaminants of drinking water," *Food Chem. Toxicol.*, vol. 38, no. SUPPL.1, pp. 13–20, 2000.
30. Y. Li, Y. Jiang, and X. P. Yan, "Probing mercury species-DNA interactions by capillary electrophoresis with on-line electrothermal atomic absorption spectrometric detection," *Anal. Chem.*, vol. 78, no. 17, pp. 6115–6120, 2006.
31. A. G. Howard and M. H. Arbab-Zavar, "Determination of 'inorganic' arsenic(III) and arsenic(V), 'methylarsenic' and 'dimethylarsenic'species by selective hydride evolution atomic-absorption spectroscopy," Analyst, vol. 106, no. 1259, pp. 213–220, 1981.
32. A. Ono and H. Togashi, "Highly selective oligonucleotide-based sensor for mercury(II) in aqueous solutions," *Angew. Chemie - Int. Ed.*, vol. 43, no. 33, pp. 4300–4302, 2004.
33. Z. Fiket, N. Mikac, and G. Kniewald, "Determination of trace elements in wines by high resolution inductively coupled plasma mass spectrometry," Atomic Spectroscopy, vol. 31, no. 2. pp. 44–55, 2010.
34. K. Farhadi, M. Forough, R. Molaei, S. Hajizadeh, and A. Rafipour, "Highly selective Hg^{2+} colorimetric sensor using green synthesized and unmodified silver nanoparticles," *Sensors Actuators, B Chem.*, vol. 161, no. 1, pp. 880–885, 2012.
35. G. Gilmartin and D. Gingrich, "A comparison of the determination and speciation of inorganic arsenic using general HPLC methodology with UV, MS and MS/MS detection," *J. Chromatogr. B Anal. Technol. Biomed. Life Sci.*, vol. 1083, no. October 2017, pp. 20–27, 2018.
36. V. R. Samuel and K. J. Rao, "A rapid colorimetric dual sensor for the detection of mercury and lead ions in water using cysteine capped silver nanoparticles," *Chem. Phys. Impact*, vol. 6, no. January, p. 100161, 2023.
37. B. S. Boruah, R. Biswas, and P. Deb, "A green colorimetric approach towards detection of arsenic (III): A pervasive environmental pollutant," *Opt. Laser Technol.*, vol. 111, no. September 2018, pp. 825–829, 2019.
38. Y. Zhang, H. Zhao, Z. Wu, Y. Xue, X. Zhang, Y. He, X. Li and Z. Yuan, "A novel graphene-DNA biosensor for selective detection of mercury ions," *Biosens. Bioelectron.*, vol. 48, pp. 180–187, 2013.

39. M. Taniguchi, M. S. R. Siddiki, S. Ueda, and I. Maeda, “Mercury (II) sensor based on monitoring dissociation rate of the trans-acting factor MerR from cis-element by surface plasmon resonance,” *Biosens. Bioelectron.*, vol. 67, pp. 309–314, 2015.
40. N. I. M. Fauzi, Y. W. Fen, N. A. S. Omar, S. Saleviter, W. M. E. M. M. Daniyal, H. S. Hashim and M. Nasrullah, “Nanostructured chitosan/maghemite composites thin film for potential optical detection of mercury ion by surface plasmon resonance investigation,” *Polymers (Basel).*, vol. 12, no. 7, pp. 1–13, 2020.
41. J. Castillo, J. Chirinos, H. Gutiérrez, and M. La Cruz, “Surface plasmon resonance sensor based on golden nanoparticles and cold vapour generation technique for the detection of mercury in aqueous samples,” *Opt. Laser Technol.*, vol. 94, pp. 34–39, 2017.
42. G. Jiang, Y. Miao, J. Wang, H. Shao, H. Chen, P. Tao, W. Wang, Q. Yu, W. Peng and X. Zhou, “Specific detection of mercury ions based on surface plasmon resonance sensor modified with 1, 6-hexanedithiol,” *Sensors Actuators A Phys.*, vol. 356, no. April, p. 114343, 2023.
43. D. Huang, T. Hu, N. Chen, W. Zhang, and J. Di, “Development of silver/gold nanocages onto indium tin oxide glass as a reagentless plasmonic mercury sensor,” *Anal. Chim. Acta*, vol. 825, pp. 51–56, 2014.
44. P. R. Solanki, N. Prabhakar, M. K. Pandey, and B. D. Malhotra, “Surface plasmon resonance-based DNA biosensor for arsenic trioxide detection,” *Int. J. Environ. Anal. Chem.*, vol. 89, no. 1, pp. 49–57, 2009.
45. A. Das, S. Mohanty, and B. K. Kuanr, “Label-free gold nanorod-based plasmonic sensing of arsenic(iii) in contaminated water,” *Analyst*, vol. 144, no. 15, pp. 4708–4718, 2019.
46. S. S. Nagarkar, A. V. Desai, and S. K. Ghosh, “Engineering metalorganic frameworks for aqueous phase 2,4,6 trinitrophenol (TNP) sensing,” CrystEngComm, vol. 18, no. 17, pp. 2994–3007, 2016.
47. A. Preiss, A. Bauer, H. M. Berstermann, S. Gerling, R. Haas, A. Joos, A. Lehmann, L. Schmelz and K. Steinbach, “Advanced high-performance liquid chromatography method for highly polar nitroaromatic compounds in ground water samples from ammunition waste sites,” J. Chromatogr. A, vol. 1216, no. 25, pp. 4968–4975, 2009.
48. S. Kumari, S. Joshi, T. C. Cordova-Sintjago, D. D. Pant, and R. Sakhuja, “Highly sensitive fluorescent imidazolium-based sensors for nanomolar detection of explosive picric acid in aqueous medium,” Sensors Actuators, B Chem., vol. 229, pp. 599–608, 2016.
49. M. Nipper, R. S. Carr, J. M. Biedenbach, R. L. Hooten, and K. Miller, “Fate and effects of picric acid and 2,6-DNT in marine environments: Toxicity of degradation products,” Mar. Pollut. Bull., vol. 50, no. 11, pp. 1205–1217, 2005.
50. H. Ko, S. Chang, and V. V. Tsukruk, “Porous substrates for label-free molecular level detection of nonresonant organic molecules,” ACS Nano, vol. 3, no. 1, pp. 181–188, 2009.
51. S. Babaee and A. Beiraghi, “Micellar extraction and high performance liquid chromatography-ultra violet determination of some explosives in water samples,” Anal. Chim. Acta, vol. 662, no. 1, pp. 9–13, 2010.
52. P. Srinivasan, M. Gunasekaran, T. Kanagasekaran, R. Gopalakrishnan, and P. Ramasamy, “2,4,6-Trinitrophenol (TNP): An organic material for nonlinear optical (NLO) applications,” J. Cryst. Growth, vol. 289, no. 2, pp. 639–646, 2006.
53. Y. Peng, A. J. Zhang, M. Dong, and Y. W. Wang, “A colorimetric and fluorescent chemosensor for the detection of an explosive-2,4,6-trinitrophenol (TNP),” Chem. Commun., vol. 47, no. 15, pp. 4505–4507, 2011.
54. Gao Yuqian, Qi Yuancheng, Zhao Kui, Wen Qing, Shen Jinwen, Qiu Liyou and Mou Wanzhi, “An optical sensing platform for the dual channel detection of picric: The combination of rhodamine and metal-organic frameworks,”.

Sensors Actuators, B Chem., vol. 257, pp. 553–560, 2018.

55. Jiarui Huang, Liyou Wang, Chengcheng Shi, Yijuan Dai, Cuiping Gu and Jinhuai Liu, “Selective detection of picric acid using functionalized reduced graphene oxide sensor device,” . Sensors Actuators, B Chem., vol. 196, pp. 567–573, 2014.
56. S. James, B. Chishti, S. A. Ansari, O. Y. Alothman, H. Fouad, Z. A. Ansari and S. G. Ansari, “Nanostructured Cuprous-Oxide-Based Screen-Printed Electrode for Electrochemical Sensing of Picric Acid,” J. Electron. Mater., vol. 47, no. 12, pp. 7505–7513, 2018.
57. J. M. Mohan, K. Amreen, M. B. Kulkarni, A. Javed, S. K. Dubey, and S. Goel, “Optimized ink jetted paper device for electroanalytical detection of picric acid,” Colloids Surfaces B Biointerfaces, vol. 208, no. August, p. 112056, 2021.
58. Y. Z. Fan, Y. Zhang, N. Li, S. G. Liu, T. Liu, N. B. Li and H. Q. Luo, “A facile synthesis of water-soluble carbon dots as a label-free fluorescent probe for rapid, selective and sensitive detection of picric acid,” Sensors Actuators, B Chem., vol. 240, pp. 949–955, 2017.
59. Tingting Luo, Yiqi Li, Yanxue Xu, Shiting Zhang, Yujue Wang, Xingming Kou and Dan Xiao, “Rapid synthesis of a hyperfluorescence 2-pyridone derivative as a fluorescent molecular sensor for picric acid,” Sensors Actuators, B Chem., vol. 253, pp. 231–238, 2017.
60. K. Li, R. H. Yu, C. M. Shi, F. R. Tao, T. D. Li, and Y. Z. Cui, “Electrospun nanofibrous membrane based on AIE-active compound for detecting picric acid in aqueous solution,” Sensors Actuators, B Chem., vol. 262, pp. 637–645, 2018.
61. W. Dong, Q. Ma, Z. Ma, Q. Duan, X. Lu, N. Qiu, T. Fei and Z. Su, “Phosphorescent iridium(III) complex based photoluminescence sensor for sensitive and selective detection of picric acid,” Dye. Pigment., vol. 172, no. August 2019.
62. Shengmei Guo, Yuyang Zhang, Jianyan Huang, Lin Kong and Jiaxiang Yang, “High dual-state blue emission of a functionalized pyrazoline derivative for picric acid detection,” CrystEngComm., vol. 23, pp. 221-226, 2021.
63. K. C. Remani and N. N. Binitha, “Fluorescence sensing of picric acid by ceria nanostructures prepared using fenugreek extract,” Iranian Chemical Society., vol. 19, pp. 619-633, 2022.
64. H. Yuan, W. Ji, S. Chu, Q. Liu, S. Qian, J. Guang, J. Wang, X. Han, J. Masson, and W. Peng, “Mercaptopyridine-Functionalized Gold Nanoparticles for Fiber-Optic Surface Plasmon Resonance Hg 2+ Sensing,” *ACS Sensors*, vol. 4, no. 3, pp. 704–710, 2019.
65. V. P. Prakashan, G. Georgea, M.S. Sanua, M.S. Sajnaa, A.C. Sarithaa, C. Sudarsanakumara, P.R. Bijua, C. Josepha and N.V. Unnikrishnan, “Investigations on SPR induced Cu@Ag core shell doped SiO2-TiO2-ZrO2 fiber optic sensor for mercury detection,” *Appl. Surf. Sci.*, vol. 507, no. December 2019, 2020.
66. H. Yuan, G. Sun, W. Peng, W. Ji, S. Chu, Q. Liu and Y. Liang, “Thymine-Functionalized Gold Nanoparticles (Au NPs) for a Highly Sensitive Fiber-Optic Surface Plasmon Resonance Mercury Ion Nanosensor,” *Nanomater. 2021, Vol. 11, Page 397*, vol. 11, no. 2, p. 397, Feb. 2021.
67. D. Rithesh Raj, S. Prasanth, T. V. Vineeshkumar, and C. Sudarsanakumar, “Surface Plasmon Resonance based fiber optic sensor for mercury detection using gold nanoparticles PVA hybrid,” *Opt. Commun.*, vol. 367, pp. 102–107, 2016.
68. X. Zhong, L. Ma, G. Yin, M. Gan, and Y. Wei, “Hg2+ optical fiber sensor based on LSPR with PDDA-templated AuNPs and CS/PAA Bilayers,” *Appl. Sci.*, vol. 10, no. 14, 2020.

69. B. S. Boruah, N. Ojah, and R. Biswas, “Bio-Inspired Localized Surface Plasmon Resonance Enhanced Sensing of Mercury through Green Synthesized Silver Nanoparticle,” *J. Light. Technol.*, vol. 38, no. 7, pp. 2086–2091, 2020.
70. G. M. Shukla, N. Punjabi, T. Kundu, and S. Mukherji, “Optimization of Plasmonic U-Shaped Optical Fiber Sensor for Mercury Ions Detection Using Glucose Capped Silver Nanoparticles,” *IEEE Sens. J.*, vol. 19, no. 9, pp. 3224–3231, 2019.
71. A. A. Khan, P. M. Thirunavakkarasu, A. S. M. Noor, N. bte Saidin, and N. Waqas, “Development and sensitivity analysis of MWCNTs coated D-shaped plastic optical fiber sensor for the detection of mercury,” *Opt. Fiber Technol.*, vol. 85, no. April, p. 103813, 2024.
72. B. Wu *et al.*, “Gold nanoparticle-enhanced D-shaped optical fiber sensor for mercury ion detection,” *Anal. Methods*, vol. 16, no. 34, pp. 5872–5882, 2024.
73. T. H. Nguyen, T. Sun, and K. T. V. Grattan, “A Turn-On Fluorescence-Based Fibre Optic Sensor for the Detection of Mercury,” *Sensors (Basel).*, vol. 19, no. 9, 2019.
74. S. Sharma and B. D. Gupta, “ Fiber optic surface-plasmon-resonance-based highly sensitive arsenic sensor prepared using α-Fe 2O3/SnO2 core-shell nanostructure with optimized probe parameters ,” *Appl. Opt.*, vol. 57, no. 36, p. 10466, 2018.
75. A. Shukla, T. Pal, and S. Mukherjia, “Gold Nanoparticles Coated Aptamer-based Fiber Optic LSPR Biosensor for Arsenic Detection,” *APSCON 2023 - IEEE Appl. Sens. Conf. Symp. Proc.*, pp. 54–56, 2023.
76. A. Shukla, T. Pal, and S. Mukherji, “Polyaniline Coated U-Bent Optical Fiber Aptasensor for Detection of Arsenic in Environmental Matrices,” *IEEE Sens. J.*, vol. PP, no. Xx, p. 1, 2024.
77. L. Zhao, J. Gan, T. Xia, L. Jiang, J. Zhang, Y. Cui, G. Qian and Z. Yang, “A luminescent metal-organic framework integrated hydrogel optical fibre as a photoluminescence sensing platform for fluorescence detection,” J. Mater. Chem. C, vol. 7, no. 4, pp. 897– 904, 2019.
78. S. S. R. Dasary, A. K. Singh, K. S. Lee, H. Yu, and P. C. Ray, “A miniaturized fiber-optic fluorescence analyzer for detection of Picricacid explosive from commercial and environmental samples,” Sensors Actuators, B Chem., vol. 255, pp. 1646–1654, 2018.
79. L. Gong, B. Du, L. Pan, Q. Liu, K. Yang, W. Wang, H. Zhao, L. Wu and Y. He, “Colorimetric aggregation assay for arsenic(III) using gold nanoparticles,” *Microchim. Acta*, vol. 184, no. 4, pp. 1185–1190, 2017.
80. N. I. Zaaba, K. L. Foo, U. Hashim, S. J. Tan, W. W. Liu, and C. H. Voon, “Synthesis of Graphene Oxide using Modified Hummers Method: Solvent Influence,” *Procedia Eng.*, vol. 184, pp. 469–477, 2017.
81. C. V Mohod and J. Dhote, “Review of Heavy Metals in Drinking Water and Their Effect on Human Health,” *Int. J. Innov. Res. Sci. Eng. Technol.*, vol. 2, no. 7, pp. 2992–2996, 2013.
82. P. Kanchana, N. Sudhan, S. Anandhakumar, J. Mathiyarasu, P. Manisankar, and C. Sekar, “Electrochemical detection of mercury using biosynthesized hydroxyapatite nanoparticles modified glassy carbon electrodes without preconcentration,” *RSC Adv.*, vol. 5, no. 84, pp. 68587–68594, 2015.
83. N. Bloom and W. F. Fitzgerald, “Determination of volatile mercury species at the picogram level by low-temperature gas chromatoraphy with cold-vapor atomic fluorescence detection,” *Anal. Chim. Acta*, vol. 208, pp. 151–161, 1988.
84. R. A. Soomro, A. Nafady, Sirajuddin, N. Memon, T. H. Sherazi, and N. H. Kalwar, “L-cysteine protected copper nanoparticles as colorimetric sensor for mercuric ions,” *Talanta*, vol. 130, pp. 415–422, 2014.

85. A. Jeevika and D. R. Shankaran, “Functionalized silver nanoparticles probe for visual colorimetric sensing of mercury,” *Mater. Res. Bull.*, vol. 83, pp. 48–55, 2016.
86. X. Liu, R. Ma, X. Wang, Y. Ma, Y. Yang, L. Zhuang, S. Zhang, R. Jehan, J. Chen and X. Wang, “Graphene oxide-based materials for efficient removal of heavy metal ions from aqueous solution: A review,” Environ. Pollut., vol. 252, pp. 62–73, 2019.
87. T. A. Ahmed and B. M. Aljaeid, “Preparation, characterization, and potential application of chitosan, chitosan derivatives, and chitosan metal nanoparticles in pharmaceutical drug delivery,” *Drug Des. Devel. Ther.*, vol. 10, pp. 483–507, 2016.
88. L. Gong, B. Du, L. Pan, Q. Liu, K. Yang, W. Wang, H. Zhao, L. Wu and Y. He, “Colorimetric aggregation assay for arsenic(III) using gold nanoparticles,” *Microchim. Acta*, vol. 184, no. 4, pp. 1185–1190, 2017.
89. N. I. Zaaba, K. L. Foo, U. Hashim, S. J. Tan, W. W. Liu, and C. H. Voon, “Synthesis of Graphene Oxide using Modified Hummers Method: Solvent Influence,” *Procedia Eng.*, vol. 184, pp. 469–477, 2017.
90. W. M. A. El Rouby, A. A. Farghali, M. A. Sadek, and W. F. Khalil, “Fast Removal of Sr(II) From Water by Graphene Oxide and Chitosan Modified Graphene Oxide,” *J. Inorg. Organomet. Polym. Mater.*, vol. 28, no. 6, pp. 2336–2349, 2018.
91. L. G. Bousiakou, H. Gebavi, L. Mikac, S. Karapetis, and M. Ivanda, “Surface enhanced Raman spectroscopy for molecular identification- A review on surface plasmon resonance (SPR) and localised surface plasmon resonance (LSPR) in optical nanobiosensing,” *Croat. Chem. Acta*, vol. 92, no. 4, pp. 479–494, 2019.
92. Z. Geng, H. Zhang, Q. Xiong, Y. Zhang, H. Zhao, and G. Wang, “A fluorescent chitosan hydrogel detection platform for the sensitive and selective determination of trace mercury(II) in water,” *J. Mater. Chem. A*, vol. 3, no. 38, pp. 19455–19460, 2015.
93. S. S. R. Dasary, A. K. Singh, K. S. Lee, H. Yu, P. C. Ray, “Miniaturized fiber-optic fluorescence analyzer for detection of Picric-acid explosive from commercial and environmental samples” *Sensors Actuators, B Chem.*, vol. 255, pp. 1646–1654, 2018.
94. R. H. Krishna, M. N. Chandraprabha, K. Samrat, T. P. Krishna Murthy, C. Manjunatha, and S. G. Kumar, “Carbon nanotubes and graphene-based materials for adsorptive removal of metal ions – A review on surface functionalization and related adsorption mechanism,” Appl. Surf. Sci. Adv., vol. 16, no. June, p. 100431, 2023.
95. E. M. Sadek, D. E. El-Nashar, A. A. Ward, and S. M. Ahmed, “Study on the properties of multi-walled carbon nanotubes reinforced poly (vinyl alcohol) composites,” J. Polym. Res., vol. 25, no. 12, 2018.
96. E. M. Sadek, D. E. El-Nashar, A. A. Ward, and S. M. Ahmed, “Study on the properties of multi-walled carbon nanotubes reinforced poly (vinyl alcohol) composites,” *J. Polym. Res.*, vol. 25, no. 12, 2018.
97. S. S. R. Dasary, A. K. Singh, K. S. Lee, H. Yu, P. C. Ray, “Miniaturized fiber-optic fluorescence analyzer for detection of Picric-acid explosive from commercial and environmental samples” *Sensors Actuators, B Chem.*, vol. 255, pp. 1646–1654, 2018.
98. L. Feng, M. Cao, X. Ma, Y. Zhu, and C. Hu, “Superparamagnetic high-surface-area Fe 3O 4 nanoparticles as adsorbents for arsenic removal,” *J. Hazard. Mater.*, vol. 217–218, pp. 439–446, 2012.
99. X. C. Le, “Speciation of arsenic compounds using high-performance liquid chromatography at elevated temperature and selective hydride generation atomic fluorescence detection,” *Anal. Chem.*, vol. 68, no. 24, pp. 4501–4506, 1996.
100. L. Gong *et al.*, “Colorimetric aggregation assay for arsenic(III) using gold nanoparticles,” *Microchim. Acta*, vol.

184, no. 4, pp. 1185–1190, 2017.

101. K. Shrivas, R. Shankar, and K. Dewangan, "Gold nanoparticles as a localized surface plasmon resonance based chemical sensor for on-site colorimetric detection of arsenic in water samples," *Sensors Actuators, B Chem.*, vol. 220, pp. 1376–1383, 2015.

102. S. Sharma and B. D. Gupta, "Lossy Mode Resonance-Based Fiber Optic Sensor for the Detection of As (III) Using α-Fe2O3/SnO2 Core-Shell Nanostructures," *IEEE Sens. J.*, vol. 18, no. 17, pp. 7077–7084, 2018.

103. A. S. K. Kumar and S. J. Jiang, "Chitosan-functionalized graphene oxide: A novel adsorbent an efficient adsorption of arsenic from aqueous solution," *J. Environ. Chem. Eng.*, vol. 4, no. 2, pp. 1698–1713, 2016.

104. S. Mohan, S. K. Khijwania, "Graphene oxide based optical fiber humidity sensor having a linear response throughout a large dynamic range and optimum sensitivity," *Appl. Opt.*, vol. 63, no. 1, 2024.

105. L. Önnby, P. S. Kumar, K. G. V. Sigfridsson, O. F. Wendt, S. Carlson, and H. Kirsebom, "Improved arsenic(III) adsorption by Al2O3 nanoparticles and H2O2: Evidence of oxidation to arsenic(V) from X-ray absorption spectroscopy," *Chemosphere*, vol. 113, pp. 151–157, 2014.

106. H. Ahmad, A. R. A. Abdulwahab, B. H. Koo, and R. A. Khan, "Selective Extraction of Trace Arsenite Ions Using a Highly Porous Aluminum Oxide Membrane with Ordered Nanopores," *ACS Omega*, vol. 7, no. 3, pp. 3044–3051, 2022.

107. P. Devi, C. Sharma, P. Kumar, M. Kumar, B.K.S. Bansod, M. K. Nayak and M. L. Singla, "Selective electrochemical sensing for arsenite using rGO/Fe3O4 nanocomposites," *J. Hazard. Mater.*, vol. 322, pp. 85–94, 2017.

108. B. B. Rasulkhan, S. K. Ponnaiah, P. Periakaruppan, G. Venkatachalam, and J. Balasubramanian, "A new CQDs/f-MWCNTs/GO nanocomposite electrode for arsenic (10-12M) quantification in bore-well water and industrial effluents," *New J. Chem.*, vol. 44, no. 42, pp. 18149–18156, 2020.

109. A. Baranik, A. Gagor, I. Queralt, E. Marguí, R. Sitko, and B. Zawisza, "Determination and speciation of ultratrace arsenic and chromium species using aluminium oxide supported on graphene oxide," *Talanta*, vol. 185, no. March, pp. 264–274, 2018.

110. I. Iatsunskyi, M. Kempiński, M. Jancelewicz, K. Załęski, S. Jurga, and V. Smyntyna, "Structural and XPS characterization of ALD Al2O3 coated porous silicon," *Vacuum*, vol. 113, pp. 52–58, 2015.

111. R. D. González, L. G. Varela, and P. B. Barrera,"Functionalized gold nanoparticles for the detection of arsenic in water," *Talanta*, vol. 118, pp. 262–269, 2014.

112. Ghodake, Gajanan, Vassilios, S. Choi, J. Hak, Jang, J. Lee, D. Sung, "Facile Synthesis of Gold Nanoparticles by Amino Acid Asparagine: Selective Sensing of Arsenic," J. Nanosci. Nanotechnol., vol. 15, no. 9, pp. 7235-7239, 2015.

113. J. Li, L. Zhang, P. Li, Y. Zhang, and C. Dong, "One step hydrothermal synthesis of carbon nanodots to realize the fluorescence detection of picric acid in real samples," *Sensors Actuators, B Chem.*, vol. 258, pp. 580–588, 2018.

114. K. A. Willets and R. P. Van Duyne, "Localized surface plasmon resonance spectroscopy and sensing," Annu. Rev. Phys. Chem., vol. 58, pp. 267–297, 2007.

115. S. K. Arya, S. Saha, J. E. Ramirez-Vick, V. Gupta, S. Bhansali, and S. P. Singh, "Recent advances in ZnO nanostructures and thin films for biosensor applications: Review," Anal. Chim. Acta, vol. 737, pp. 1–21, 2012.

116. X. Chen, Q. Wang, X. J. Wang, J. Li, and G. Bin Xu, "Synthesis and performance of ZnO quantum dots water-based fluorescent ink for anti-counterfeiting applications," Sci. Rep., vol. 11, no. 1, pp. 1–9, 2021.

117. U. Priyanka, A. Gowda K M, E. M G, S. Teja B, N. Nitish, and R. Mohan B, "Biologically synthesized PbS nanoparticles for the detection of arsenic in water," *Int. Biodeterior. Biodegrad.*, vol. 119, pp. 78–86, 2017.
118. S. K. Pal, N. Akhtar, and S. K. Ghosh, "Determination of arsenic in water using fluorescent ZnO quantum dots," *Anal. Methods*, vol. 8, no. 2, pp. 445–452, 2016.
119. M. Rauf, S. K. Shah, A. Algahtani, V. Tirth, A. H. Alghtani, T. Al-Mughanam, K. Hayat, N. H. Al-Shaalan, S. Alharthi, S. A. Alharthyij and M. A. Amin, "Application of ZnO-NRs@Ni-foam substrate for electrochemical fingerprint of arsenic detection in water," *RSC Adv.*, vol. 13, no. 21, pp. 14530–14538, 2023.
120. S. Ismail, N. A. Yusof, J. Abdullah, and S. F. Abd Rahman, "Development of Electrochemical Sensor Based on Silica/Gold Nanoparticles Modified Electrode for Detection of Arsenite," *IEEE Sens. J.*, vol. 20, no. 7, pp. 3406–3414, 2020.